Unsteady Surface Heat Flux and Temperature Measurements

by

Karen Irene Baker

Thesis submitted to the Faculty of the

Virginia Polytechnic Institute and State University

in partial fulfillment of the requirements for the degree

Master of Science

in

Mechanical Engineering

APPROVED

T. E. Diller, Chairman

B. Vick

H. L. Moses

May, 1993

Blacksburg, Virginia

Unsteady Surface Heat Flux and Temperature Measurements

by

Karen Irene Baker

T. E. Diller, Chairman

Mechanical Engineering

(ABSTRACT)

A fast response thin-film heat flux sensor was used to measure the time-resolved surface heat flux and temperature from a turbulent combustion flame impinging on a surface. Using the analytical semi-infinite conduction model, the unsteady surface heat flux was calculated from the transient temperature measurements and the surface temperature was calculated from the unsteady surface heat flux measurements.

Methods of comparing time-resolved heat flux and temperature data were presented and discussed. The standard analytical method for converting surface temperature to heat flux was used. Two new analytical methods were developed for converting heat flux to surface temperature.

The study is the first demonstration of time-resolved temperature signals generated from time-resolved heat flux measurements. The results graphically illustrate the effects of data processing on electrical noise present in the actual signal. The effect of flame unsteadiness is also shown, especially in the time-resolved heat flux measurements, which gives insight into the behavior of a propane torch. One application is for development of feed-forward control systems in industrial processes with fast transients.

Acknowledgments

First, I would like to thank Dr. Diller for his guidance over the last year. He has always had good advice for all the problems I encountered. I would also like to express my gratitude to Dr. H. Moses and Dr. B. Vick for serving on my committee.

I would like to thank Vatell Corporation who made the Heat Flux Microsensor and Jon Hager and Jim Terrell for their advice and help during this research.

Thanks to Janice E. Burr who made life more bearable for me and made me laugh. She was always willing to listen and provide an opinion on any topic.

Thanks to my friends from the University of North Carolina at Charlotte: Susan Oberhofer, Haj Baji, and Bonnie Hunter. They gave me motivation and support when I needed it most.

I'd also like to thank my brother, Dr. Gregory R. Baker, for his support and wise advice. He has always been there for me and I owe a lot of my success to him.

Most importantly, I'd like to thank my parents, Patrick and Faye Baker, for their continual inspiration, support, and encouragement. Without them, I would never have made it.

Finally, I would like to thank God for making all my dreams come true.

Table of Contents

List of Figures

List of Tables

Nomenclature

A	amplitude
C	specific heat, $J/kg \cdot K$
E_q	Heat flux sensor output, V
E_T	Temperature sensor output, V
f	pulsation frequency, Hz
G	Green's function
h	heat transfer coefficient
h_c	corrected heat transfer coefficient
h_i	indicated heat transfer coefficient
j	summation counter
k	thermal conductivity, $W/m \cdot K$
n	number of equal divisions of time interval
q	heat flux, W/cm^2
q_o	initial surface heat flux, W/cm^2
q_{rad}	radiation heat flux, W/cm^2
q_s	surface heat flux, W/cm^2
S	sensitivity

S_q	sensitivity of the Heat Flux Microsensor, $\mu V/(W/cm^2)$
t	time, s
Δt	time interval (t/n), s
T	temperature, °C
T_a	air temperature, °C
T_o	initial substrate temperature, °C
T_s	surface temperature, °C
T_{so}	initial surface temperature, °C
u,du,v,dv	integration by parts variables
U	velocity, m/s
U_∞	mean stream velocity, m/s
x	space coordinate into the substrate, m
z	integration substitution
α	thermal diffusivity, m^2/s
δ	thickness, m
ϵ_g	gage emissivity
θ_s	$(T_s - T_o)$, °C
ξ	nondimensionalized space variable
ρ	density, kg/m^3
σ	Stefan-Boltzmann constant
τ	time variable

Chapter 1.0

Introduction and Objective

1.1   Introduction

One method of measuring heat flux to a surface is to measure the rate of change of temperature of the material. With appropriate transient conduction modeling and material properties, the heat flux that caused the measured temperature history can be determined.

Due to the increased interest in the details of time-resolved heat flux measurements in transient facilities, techniques have been developed for fast-response instrumentation. Several groups have refined these techniques using thin-film resistance gages for measuring the surface temperatures. Although there are various types of heat transfer gages, the analysis required for these gages is approached from a single theoretical model of one-dimensional transient heat conduction [1].

The basic time-dependent problem of thin-film gages consists of conduction into a slab of material mounted onto a semi-infinite extent of another material [1]. The Heat Flux Microsensor is an example of such a thin-film gage. From the theoretical derivation of the temperature at any point within a layered medium comprising two

1

separate substances in thermal contact, the solution of such a problem enables the temperature to be determined as a function of time for prescribed heat transfer rates [1]. The analysis for each type of gage depends upon the application of the appropriate boundary conditions [1]. Analog electrical circuits composed of resistors and capacitors have been the most popular method for the conversion of the temperature signal to heat flux to avoid problems with the data processing. The equations for the circuit can be made to match exactly the model expressed by the heat transfer equations [1].

Because of the limitations of the one-dimensional, semi-infinite models used, the transient temperature techniques are usually limited to short duration tests. A group working at NASA Lewis injected a preheated cylinder into a steady low speed flow [2] to measure the time-resolved heat flux resulting from rotor wake passage [3] and grid turbulence [4]. A group at Calspan has measured heat flux to gas turbine blades (e.g., [5]). A shock tube was used to provide the flow conditions for 20 to 25 msec to entire gas turbine stages. A group at Oxford University has been instrumental in developing the thin-film techniques for many years [6]. Their application has been turbine blades, which were tested in an isentropic light piston tunnel (e.g., [7]). Their results include extensive testing of the effects of rotor wakes and shock waves passing on the time-resolved turbine blade heat transfer (e.g., [8]). The time-resolved heat flux measurements made by this group created important advances in the understanding of unsteady effects in heat transfer analysis.

Just as surface temperature measurements can be used to calculate the heat flux,

2

heat flux measurements can be used to calculate the temperature. However, examples of using experimental heat flux measurements to predict the surface temperature of a material are not common in the literature. The required analytical methods are certainly no more difficult, but the experimental capability of making the required time-resolved heat flux measurements has not been previously available.

1.2 Objective

The data processing problems that have arisen from converting measured surface temperatures to heat flux will be illustrated in this study. Comparisons of both data reduction processes (temperature to heat flux and heat flux to temperature) will be made using a new gage, the Heat Flux Microsensor. This gage has the unique capability of measuring surface temperature and heat flux simultaneously. Because the frequency response of both sensors is better than 50 kHz, the time-resolution of the signals is not compromised by the sensor response. The surface temperature and heat flux signals are compared using the same analytical conduction model in the substrate with three data-reduction schemes. The temperature signal from the sensor is used to generate time-resolved heat flux measurements. This is achieved using the analytical methods discussed in Chapter 2.0. The heat flux signal from the sensor is used to generate surface temperature measurements using the integration methods of Duhamel's method and

3

Green's Function detailed in Chapter 3.0. One application for obtaining surface temperature traces from time-resolved heat flux measurements is improved temperature control systems for gas turbines and other industrial processes with fast transients.

Chapter 2.0

Literature Review

There are three major topics of this review to address: the different types of heat flux measurement devices, the Heat Flux Microsensor, and the analytical methods used to process the data acquired in the experiment. In the first section, the various techniques for heat flux measurement in unsteady flow will be investigated. Second, the fabrication, operational techniques and the advantages of the Heat Flux Microsensor will be addressed. Lastly, the analytical methods previously used to process the experimental data will be discussed.

2.1   Heat Flux Measurement Devices

The majority of heat flux gages that measure heat transfer between a flowing fluid and a solid surface are categorized into three groups: (1) those that measure the electrical power dissipated in a heater at steady state, (2) those that measure the rate of change of thermal energy of the surface, and (3) those that measure the temperature difference across a known thermal resistance in the surface [9]. All three categories of

gages have been used in measuring time-resolved heat transfer at the solid surface [10].

Figure 1 illustrates an example of a category (1) gage. This gage monitors the electric power necessary to maintain a heated surface temperature. Although this type of gage provides accurate results for large surface areas, it does not perform well for smaller surface areas where fine spatial resolution is needed [11]. The largest errors for this gage arise from either heat losses at the edges of the measurement region or power measurements made before thermal equilibrium [10]. In addition, when these gages are made using thin-film resistance layers, a feedback control system must be used to control surface temperature [12]. This method is not passive and can only be used to measure heat flux from the surface. Because of the spatial constraints of this type of gage and the inability for it to measure heat flux to the surface, this category of gages was inappropriate for use in this experimental study.

Category (2) gages utilize the thermal capacitance of the gage and/or model material in conjunction with surface temperature measurements to infer the heat transfer from the time-temperature history [10]. This method has been used with slug calorimeters in the past, but more recent usage has been with thin-film resistance elements to measure time-dependent surface temperature [10]. Although these gages have a fast time response and are useful in short duration flows, they must be driven by a small current to measure resistance. Examples of experiments using this method can be found in [3,5,13,14,15]. Heat transfer is inferred from the temperature measurements by analytically determining the heat transfer coefficient history required to produce the
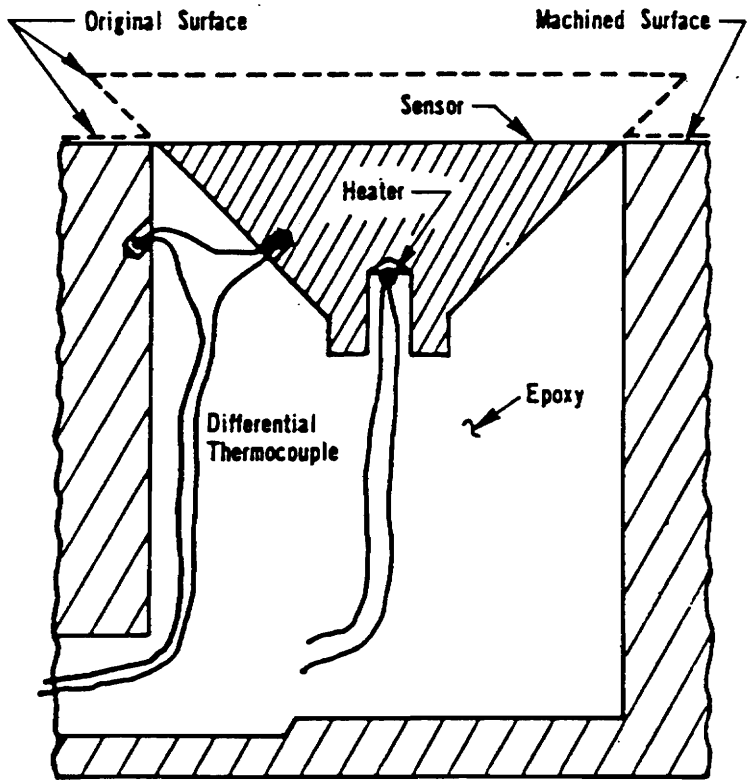
Figure 1. Example of a Category (1) Gage [10]

observed temperature history [10]. In effect, the solution is that of an inverse heat transfer problem for a semi-infinite model. Solutions differ according to the gage used and assumptions about the substrate material properties. Because the heat transfer is inferred from temperature measurements, the solution is similar to the differentiation method that will be discussed later. However, as in the present experiment, this type of data processing amplifies any distortions of the temperature signal when calculating the heat flux [16,17].

The final category of gages include gages that measure a temperature difference across a known thermal resistance. A thermopile is usually formed to multiply the output signals by placing thermocouples in series across the thermal resistance layer to measure the temperature difference [10]. Then, the gage output voltage is approximately proportional to the temperature difference across the gage. From heat transfer analysis, it is seen that the output voltage is also approximately proportional to the heat flux. This method is totally passive since the gage measures the self-generated voltage output. Another advantage is that these gages are capable of measuring heat flux in either direction. For small gages, there is a physical limitation on where to place the thermocouple junctions. This limitation creates a potential physical and thermal disruption of the flow field caused by the measuring device itself. Using a layered heat flux gage as the one shown in Fig. 2, the gage's surface disruption is minimized. The Heat Flux Microsensor, used in the present study, is one of the layered heat flux gages that exemplify this category of heat flux measurement devices.
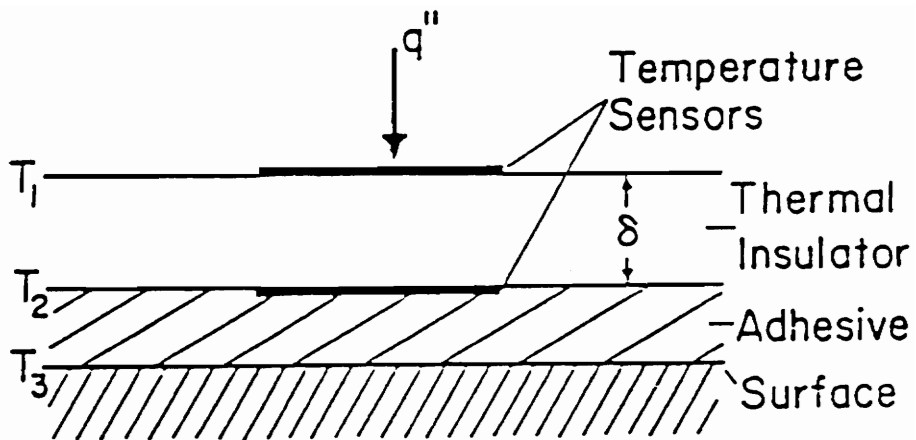
Figure 2. Schematic Cross Section of a Layered Heat Flux Gage [10]

2.2   The Heat Flux Microsensor

The direct comparison of experimental surface temperature and heat flux is possible using a Heat Flux Microsensor. Using microfabrication techniques, this new heat flux gage system possesses favorable attributes for measuring unsteady heat flux. The gages are small, have a high frequency response, are able to measure very high heat flux, and output voltages that are directly proportional to the heat flux and surface temperature [18,19].

As illustrated in Fig. 3, the heat flux sensor consists of a thin thermal resistance layer sandwiched between temperature sensors. To amplify the output signal on the gage, many thermocouple pairs are fabricated across the thermal resistance layer to form a differential thermopile [20]. The thermocouple is formed by narrow metal strips of platinum and platinum-rhodium overlapping above and below the silicon monoxide thermal resistance layer and forming several thermocouple junctions. This is illustrated in Fig. 4. The metal strips are connected outside of the layer to complete the thermopile circuit that wraps around the thermal resistance layer. This requires precise placement of these five layers to properly make all of the interconnections. The voltages from each pair then add in series in proportion to the temperature difference across the thermal resistance layer [20].

Since the sensors are fabricated directly onto the measurement surface and the total thickness of the sensors is less than 2 μm, the presence of the gage contributes
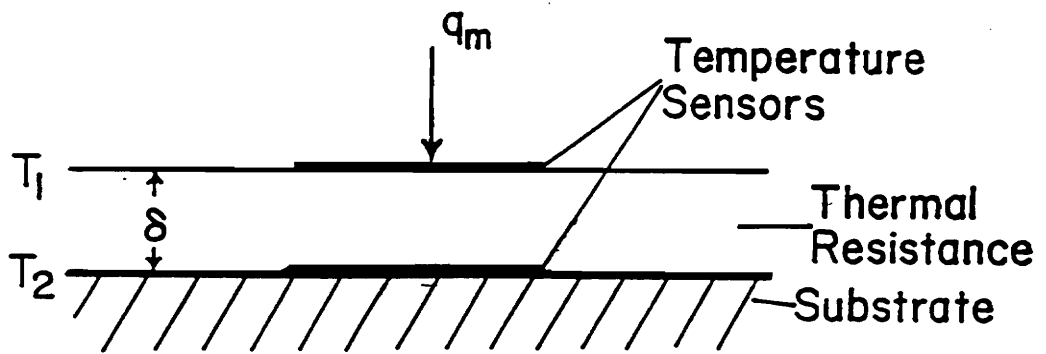
Figure 3. Schematic Cross Section of the Heat Flux Microsensor

11
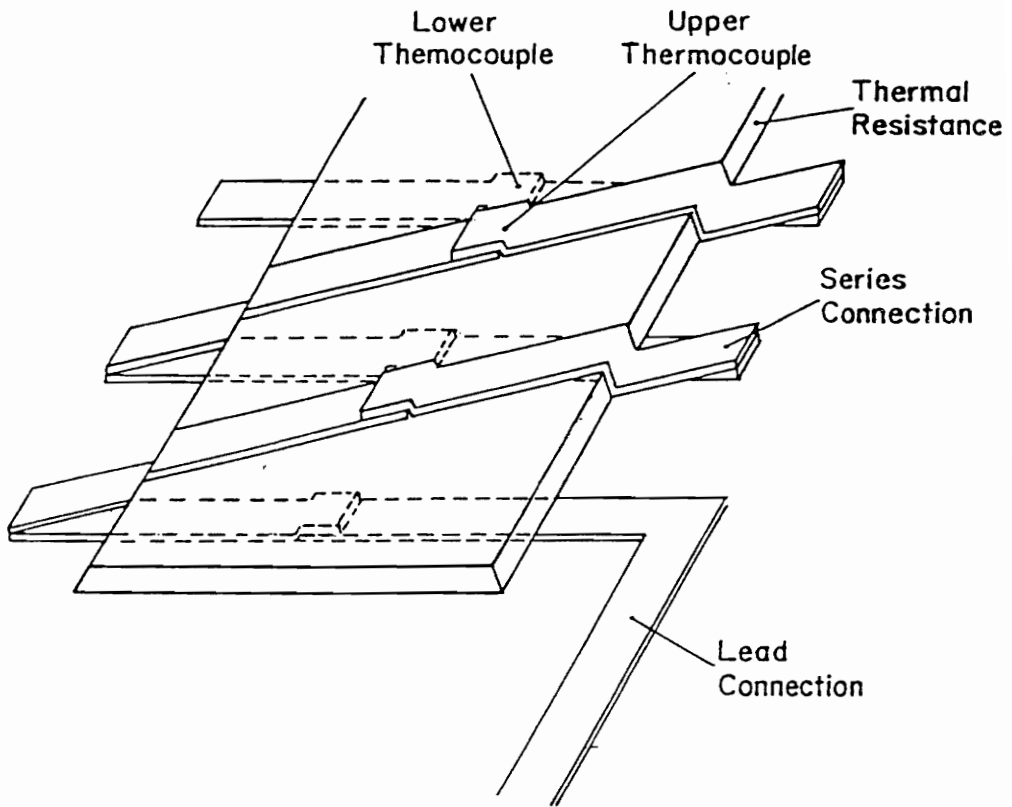
Figure 4. Detailed Section of Microsensor Thermopile

12

negligible flow and thermal disruption. Because the Heat Flux Microsensor requires no adhesive, it is thinner than other gages and has a more accurate heat flux reading. The thinness of the sensor also contributes to its high frequency response. Feed-through leads are used to bring the signals out through the back of the substrate. In addition, its fast time response, approximately 20 μsec [21], and continuous output allow the Heat Flux Microsensor to be used in both steady and transient facilities. The calibration method and results for the Heat Flux Microsensor are discussed in Appendix A.

The temperature sensor is a patterned metal layer used as a resistance temperature device. It is driven with a small current (0.2 mA). This is the same as category (2) heat flux gages. As the temperature of the sensor increases, the resistance increases, thereby increasing the output voltage. The calibration of the temperature sensor (RTS) is detailed in Appendix B.

An enlargement of a complete sensor is shown in Fig. 5. The heat flux sensor was sputtered on an aluminum nitride substrate. The thermal resistance layer consists of a sputtered silicon monoxide thermal resistance layer approximately 1 μm thick. As mentioned previously, the thermopile consists of sputtered layers of platinum and platinum/rhodium. An over-coat of aluminum oxide was used to physically protect the sensor. The temperature sensor (RTS) is a single layer of sputtered platinum.

The Heat Flux Microsensor has proven to be a useful tool in measuring time-resolved heat transfer and surface temperature. It has been successfully used in a variety of test facilities. For example, to observe the effects of unsteady flow time-resolved heat
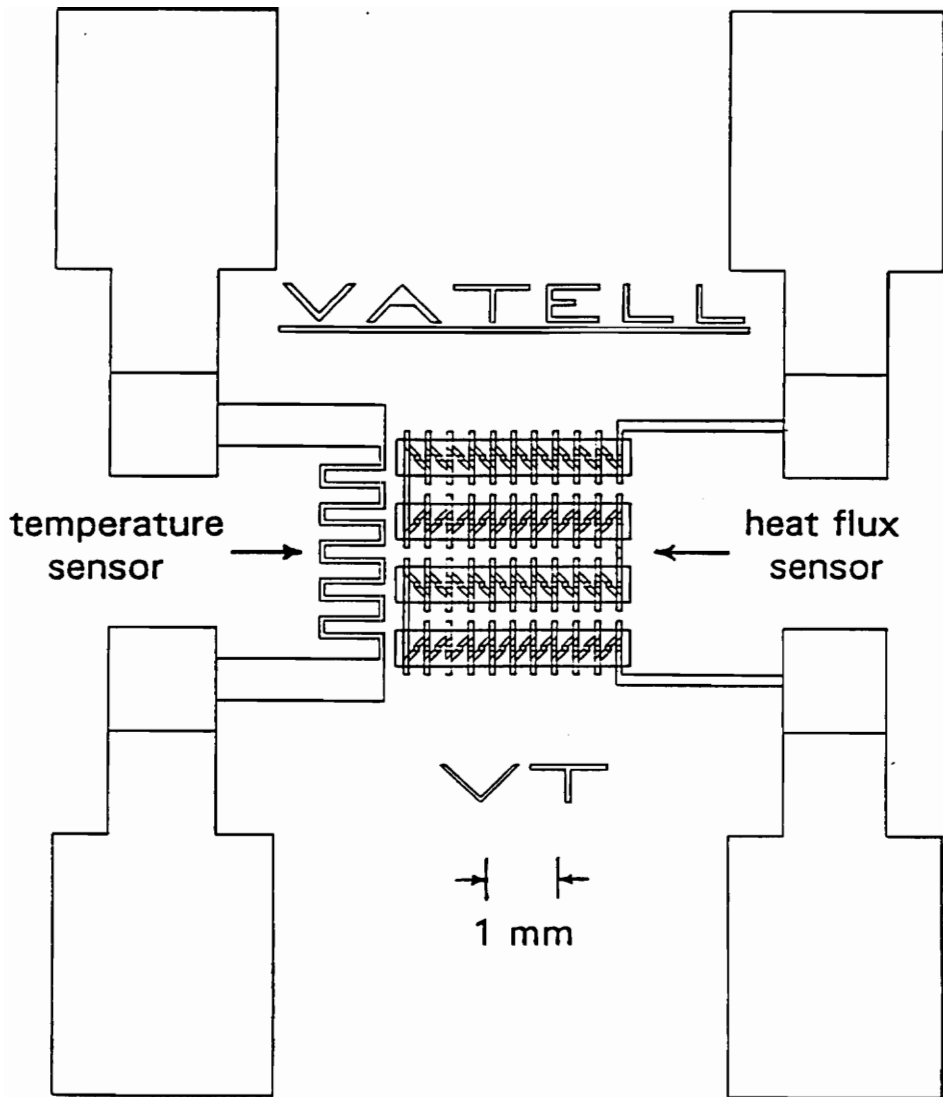
Figure 5. Heat Flux Microsensor Pattern Overlay

flux measurements to a surface in the wake region of a cylinder were made using the Heat Flux Microsensor [22]. Measurements of unsteady heat flux and local air velocity were recorded using the sensor and a hot-wire anemometer, respectively. Coherence functions were calculated for the two signals which established a causative relationship between the velocity and heat flux signals [22]. Another application is in the biomedical arena. The sensor has been used to non-invasively measure blood perfusion in animal limbs [23]. The current study uses the sensor to measure surface temperature and heat flux in a turbulent combustion flame. Analytical techniques are then used to investigate how well surface temperature correlates to heat flux and how accurately heat flux correlates to surface temperature.

2.3 Analytical Methods for Heat Flux Measurements

Before discussing the different numerical techniques used in this study, it is beneficial to look at the basis for these techniques. The governing equations used in processing transient heat transfer measurements made with the aforementioned heat flux measurement devises are primarily from one-dimensional heat conduction analysis [17]. From the first law of thermodynamics, the temperature change of a system is proportional to the rate of energy transfer across the system control volume. When only considering heat transfer, the general form for this equation is

$$\frac{\partial T}{\partial t} \propto \sum q \qquad (1)$$

For a one-dimensional semi-infinite model with constant properties Eq. 1 becomes

$$\frac{\partial T}{\partial t} = \alpha \frac{\partial^2 T}{\partial x^2} \qquad (2)$$

The geometry is illustrated in Fig. 6. Closed-form solutions to Eq. 2 have been obtained for two types of surface boundary conditions of particular interest for this study: constant surface temperature and constant surface heat flux [24]. These solutions assume constant thermal properties. The initial condition is $T = T_o$ at $t = 0$ and the two boundary conditions are temperature $T = T_o$ at $x \to \infty$ and a prescribed temperature or heat flux at the surface, $x = 0$.

The inverse of Eq. 1 is often desired; that is, the heat flux corresponding to a known (measured) surface temperature. This is commonly referred to as an inverse heat conduction problem. A detailed analysis of such problems is given in [25]. For a one-dimensional semi-infinite model with constant properties, Eq. 2 is solved subject to the conditions for a prescribed surface temperature. The initial condition is $T = T_o$ at $t = 0$ and the two boundary conditions are temperature $T = T_o$ at $x \to \infty$ and a prescribed surface temperature $T = T_s$ at $x = 0$. The solution for this problem is given by [24] for the special case, $T_s = $ constant
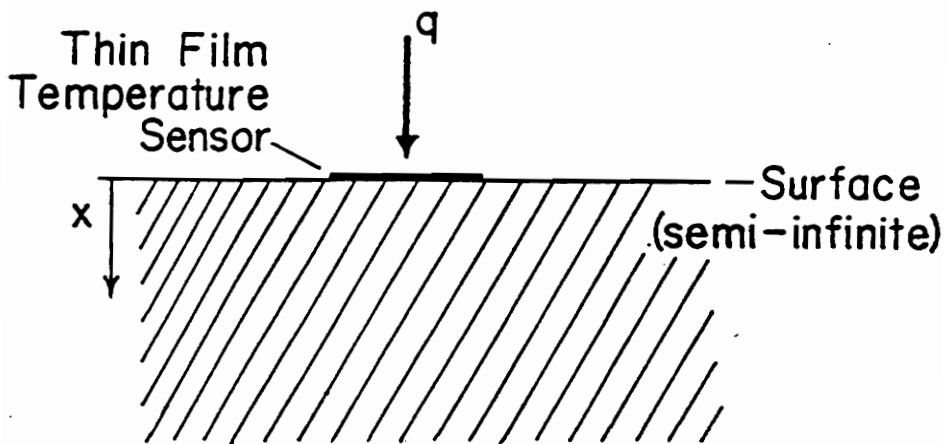
Figure 6. One-dimensional Semi-infinite Geometry

$$q_s(t) = \frac{\sqrt{k\rho C}}{\sqrt{\pi}} \frac{(T_s - T_o)}{\sqrt{t}} \tag{3}$$

From this special case, the foundation for forming the numerical techniques exists. By generalizing Eq. 3, q_s at time t_n can be determined by

$$q_s(t_n) = \frac{\sqrt{k\rho C}}{\sqrt{\pi}} \sum_{j=1}^{n} \frac{\Delta T_j}{\sqrt{t_n - t_j}} \tag{4}$$

where ΔT_j is the change in surface temperature for the jth of n time intervals and t_j is the time at the end of the jth of n time intervals. Taking limits as $\Delta t \to d\tau$,

$$q_s(t_n) = \frac{\sqrt{k\rho C}}{\sqrt{\pi}} \lim_{\Delta t_j \to d\tau} \left[\sum_{j=1}^{n} \frac{\left[\frac{\Delta T_j}{\Delta t_j}\right] \Delta t_j}{\sqrt{t_n - t_j}} \right] \tag{5}$$

the equation can be expressed in terms of an integral

$$q_s(t_n) = \frac{\sqrt{k\rho C}}{\sqrt{\pi}} \int_{\tau=0}^{t} \frac{\frac{dT_s}{d\tau}}{\sqrt{t - \tau}} d\tau \tag{6}$$

However, this solution assumes that the prescribed (or measured) surface temperature is a continuous function of time, τ [1]. The fundamental problem in using digitized data points as the input of surface temperature is that the prescribed surface temperature is not a continuous function of time. Rather, the data points are considered as stepwise

18

variations of surface temperature in time. In addition, any noise in the signal will make data reduction difficult because the differential of surface temperature is involved [1]. The expression in Eq. 6 can be integrated by parts to obtain a more convenient form [26].

First, let $z = T(t) - T(\tau)$ [1]. Then the derivative of z with respect to τ is

$$\frac{dz}{d\tau} = -\frac{dT(t)}{d\tau} \qquad (7)$$

Rewriting Eq. 6 in terms of z,

$$q_s = \frac{\sqrt{k\rho C}}{\sqrt{\pi}} \left[-\int_{\tau=0}^{t} \frac{\frac{dz}{d\tau}}{(t-\tau)^{1/2}} d\tau \right] \qquad (8)$$

Next, integrate Eq. 8 by parts. Let

$$u = (t-\tau)^{-1/2} \; , \; dv = \frac{dz}{d\tau} d\tau \qquad (9)$$

Then,

$$du = -\frac{1}{2}(t-\tau)^{-3/2} d\tau \; , \; v = z \qquad (10)$$

The equation after integration becomes

$$q_s(t_n) = \frac{\sqrt{k\rho C}}{\sqrt{\pi}} \left[-\frac{z}{(t-\tau)^{1/2}} \Big|_{0}^{t} - \frac{1}{2}\int_{\tau=0}^{t} \frac{z}{(t-\tau)^{3/2}} d\tau \right] \qquad (11)$$

Substituting for z and rewriting yields

$$q_s = \frac{\sqrt{k\rho C}}{\sqrt{\pi}} \cdot \left[\frac{T(\tau) - T(t)}{(t-\tau)^{1/2}} \Big|_0^t - \frac{1}{2} \int_{\tau=0}^t \frac{T(t) - T(\tau)}{(t-\tau)^{3/2}} d\tau \right] \qquad (12)$$

At $\tau = 0$, let $T(\tau) = 0$ [1]. Evaluating the integrand at the limits yields

$$q_s = \frac{\sqrt{k\rho C}}{\sqrt{\pi}} \left[\frac{T(t) - T(t)}{\sqrt{t-t}} + \frac{T(t)}{\sqrt{t}} + \frac{1}{2} \int_{\tau=0}^t \frac{T(\tau) - T(t)}{(t-\tau)^{3/2}} d\tau \right] \qquad (13)$$

The first term, where the integrand is evaluated at time t, is an indeterminate form of the type 0/0. Applying L'Hopital's Rule, the first term goes to 0. The result is written in final form as

$$q_s = \frac{\sqrt{k\rho C}}{\sqrt{\pi}} \left[\frac{T(t)}{\sqrt{t}} + \frac{1}{2} \int_{\tau=0}^t \frac{T(\tau) - T(t)}{(t-\tau)^{3/2}} d\tau \right] \qquad (14)$$

which has a singularity in the integral term at $t = \tau$ [1]. Because of this singularity, additional numerical techniques are required to solve Eq. 14 [26]. Several papers concur with the final form given in Eq. 14 [17,27]. However, an error was detected for the same solution in Eq. 20 of [1]. The factor of 1/2 was not carried in front of the integral.

Cook and Felderman [27] developed a numerical approximation for heat flux at time steps Δt using a piecewise linear signal on the temperature trace [17]. For their approximation, it was assumed that the surface temperature at each step Δt occurred at the midpoint of the time interval. Cook and Felderman's linear spline fits based on the temperature history can be taken into account by rewriting Eq. 14. For the nth value of

surface heat flux, this equation then becomes

$$q(t_n) = \frac{2\sqrt{k\rho C}}{\sqrt{\pi}} \sum_{j=1}^{n} \frac{T_j - T_{j-1}}{\sqrt{t_n - t_j} + \sqrt{t_n - t_{j-1}}} \tag{15}$$

where t_j is the time at the end of the jth of n time intervals. By comparison, Eq. 15 is similar to the solution obtained in Eq. 4. The only difference is that the time interval in Eq. 15 is averaged, which accounts for the factor of 2 in the numerator. This solution has an advantage over a finite-difference solution because it is easier to program [17]. It should be noted that a sign error was discovered in [28]. The denominator in Eq. 1 of [28] should be a sum of the time interval functions, as written in Eq. 15, and not a difference.

Because the solution is akin to differentiating the surface temperature with respect to time to yield heat flux, this method is termed the differentiation method. The FORTRAN program written to perform this algorithm is shown in Section D.1 of Appendix D. There has been no establishment of how accurately this algorithm reproduces fluctuations in the unsteady heat flux [17].

Chapter 3.0

Integration Methods to Obtain Surface Temperature

Since the Heat Flux Microsensor is capable of measuring surface temperature and heat flux simultaneously, the converse method of integrating the unsteady heat flux signal over time to yield the time-resolved surface temperature was developed. Two different numerical techniques were tested and evaluated. The first was Duhamel's method, or the method of superposition, and the second was Green's function. It was later shown that the expressions were identical and produced the same numerical results.

For each technique, the numerical expressions developed below were first tested to match the exact solution of the semi-infinite step change in surface temperature. First, the surface heat flux, q_s, was calculated for a constant step change in temperature of 10 °C at time intervals of 2 msec for a total time length of 10 msec using Eq. 3. Then, these calculated values of heat flux were used in an expanded form of Eq. 17 to calculate surface temperature. The techniques were determined to work if the calculated surface temperature approached the initial constant value of 10 °C.

Considering a one-dimensional semi-infinite model with constant properties, Eq. 2 is solved subject to the conditions for a prescribed surface heat flux. The initial condition is $T = T_o$ at $t = 0$ and the two boundary conditions are temperature $T = T_o$

at $x \to \infty$ and a prescribed surface heat flux at $x = 0$. The solution to this problem is given by [29]

$$\theta_s = \frac{1}{\sqrt{\pi}} \frac{1}{\sqrt{k\rho C}} \int_0^t \frac{q_s(\tau)}{\sqrt{(t-\tau)}} d\tau \qquad (16)$$

The function $q_s(\tau)$ gives the time variation of the heat flux at the boundary, with τ representing time at which the heat flux occurs for the integration. If the surface heat flux is given as a step change from zero to a constant value q_o at time $t = 0$, the solution reduces to [1]

$$\theta_s = \frac{2q_o\sqrt{t}}{\sqrt{\pi}\sqrt{k\rho C}} \qquad (17)$$

The surface temperature increases proportional to the square root of time and, thus, is parabolic in nature. The material properties of the substrate enter as the square root of the product of $k\rho C$.

3.1 Duhamel's Method

Duhamel's method, or the method of superposition, is commonly used in boundary layer theory to determine heat flux to a plate with an arbitrarily varying wall temperature along the length of the plate [30]. This method can be extended for transient

heat conduction problems with time-dependent boundary conditions by using the solution to the corresponding fundamental problem with steady boundary conditions [31]. The fundamental problem of calculating surface temperature for a one-dimensional semi-infinite model with arbitrarily varying heat flux is addressed here using the superposition method. Duhamel's method treats the time-dependent boundary condition as a sum of step changes.

As Myers states [31], the continuous portions of the function (for this study the function is heat flux) are represented as a series of very small steps occurring at Δt time intervals. Since the problem is homogeneous and linear, the response at any time t is the sum of the effects of each small step prior to time t. Thus, each step that occurs affects the system independent of other step changes.

For the first individual time step, the solution is identical to the one obtained in Eq. 17. This equation can be generalized to calculate the surface temperature at the nth time interval by

$$\theta_s(t_n) = \frac{2}{\sqrt{\pi}\sqrt{k\rho C}} \sum_{j=1}^{n} \Delta q_j \sqrt{t_n - t_j} \qquad (18)$$

where Δq_j is the change in heat flux for the jth time interval.

Figure 7a illustrates the method described above. The digitized unsteady heat flux values are treated as a series of step functions. The following numerical expression sums the effect of a series of heat flux values assuming constant Δt
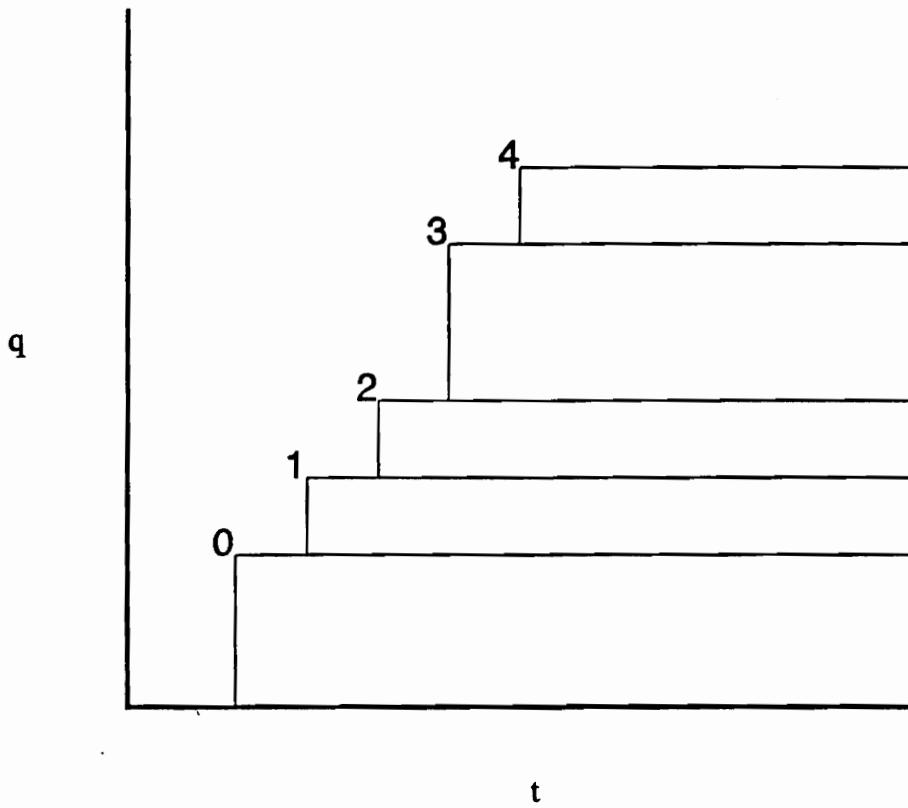
Figure 7. Integration Processes

a) Duhamel's Method - Step Function
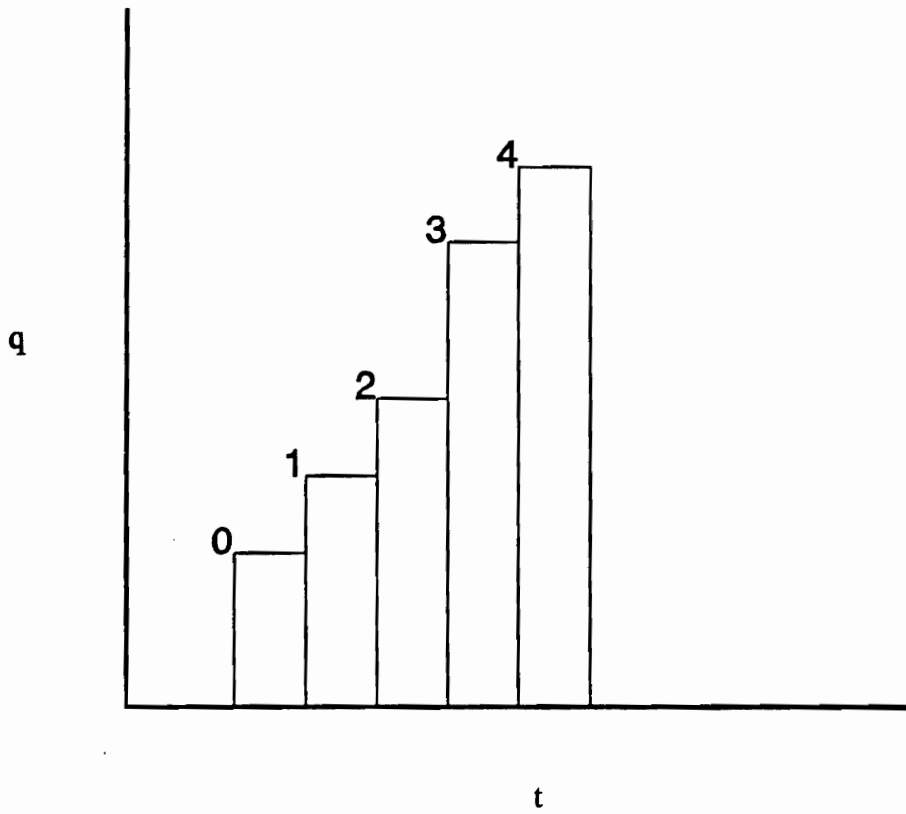
Figure 7. Integration Processes

b) Green's Function - Impulse Function

26

$$\theta_s(t_n) = \frac{2}{\sqrt{\pi}\sqrt{(k\rho C)}} \left[q_o\sqrt{t_n} + \sum_{j=1}^{n-1} (q_j - q_{j-1})\sqrt{t_n - t_j} \right] \qquad (19)$$

where n is the number of time intervals. The digitized values of unsteady heat flux were evaluated at half spacing; i.e., each digital data point was considered as occurring at the midpoint of the time interval. The FORTRAN program written to perform this numerical expression is detailed in Section D.2 of Appendix D.

3.2   Green's Function

The basic idea of Green's function is to build solutions by adding together (integrating) several instantaneous concentrated heat sources which are equivalent to the original continuous heat source. The heat sources are due to some combination of volumetric sources, surface sources, or an imposed initial condition. Figure 7b illustrates the integration process for a series of impulse functions. There are several papers that document the use of Green's function in solving transient heat conduction problems [32,33]. In addition, Ozisik's <u>Heat Conduction</u> devotes an entire chapter to the use of Green's function [34].

Green's function is a method that is capable of solving a time-dependent heat conduction equation with heat generation, subject to nonhomogeneous boundary

conditions and an initial condition [34]. This method provides a general solution for all nonhomogeneous problems in a compact manner [34].

The difficulty of using the Green's function method arises in the determination of the appropriate Green's function for a given problem. This is due to the dependency of the function on the coordinate system used, boundary conditions, and the type of region of the fundamental problem [34]. Ozisik illustrates how to construct a Green's function for a particular problem and how this is related to the solution of the homogeneous part of that problem [34].

The Green's function method was used to determine the general temperature distribution for a semi-infinite region with no volumetric heat generation, $g(\xi,\tau)$, and an initial condition of $T = T_0$ at $t = 0$. The two boundary conditions are that the surface at $x = 0$ is subjected to a specified heat flux, $q_s(t)$, and that $T = T_0$ at $x \to \infty$. The general solution for this problem is

$$\theta(x,t) = \frac{\alpha}{k} \int_{\tau=0}^{t} \int_{\xi=0}^{\infty} G \cdot g(\xi,\tau)\,d\xi\,d\tau + \frac{\alpha}{k} \int_{\tau=0}^{t} (G)_{\xi=0} \cdot q_s(\tau)\,d\tau \tag{20}$$

where

$$G = \frac{1}{\sqrt{4\pi\alpha(t-\tau)}} \left[\exp\left[-\frac{(x-\xi)^2}{4\alpha(t-\tau)} \right] + \exp\left[-\frac{(x+\xi)^2}{4\alpha(t-\tau)} \right] \right] \tag{21}$$

Taking into account that there is no volumetric heat source, $g(\xi,\tau) = 0$, and that only the surface temperature is desired, $\theta(0,t)$, the above equations become

28

$$\theta(0,t) = \frac{\alpha}{k} \int_{\tau=0}^{t} \frac{2}{\sqrt{4\pi\alpha(t-\tau)}} q_s(\tau) d\tau \qquad (22)$$

Rearranging,

$$\theta(0,t) = \frac{1}{\sqrt{\pi}\sqrt{k\rho C}} \int_{\tau=0}^{t} \frac{1}{\sqrt{t-\tau}} q_s(\tau) d\tau \qquad (23)$$

For a constant heat flux applied at $t = 0$, the above equation reduces to

$$\theta_s(t) = \frac{q}{\sqrt{\pi}\sqrt{k\rho C}} \int_{\tau=0}^{t} \frac{1}{\sqrt{t-\tau}} d\tau \qquad (24)$$

This can be integrated directly to yield the solution for the above condition by treating

the constant heat flux applied at $t = 0$ as an arbitrary impulse

$$\theta_s(t) = \frac{2q}{\sqrt{\pi}\sqrt{k\rho C}} \sqrt{\Delta t} \qquad (25)$$

which is the same solution as obtained in Eq. 17.

The individual heat flux impulse solution of Eq. 25 can be expanded to include

an arbitrarily varying heat flux over time by representing the integration in Eq. 24 as a

series summation by

$$\theta_s(t_n) = \frac{2}{\sqrt{\pi}\sqrt{(k\rho C)}} \sum_{j=1}^{n} q_j \left[\sqrt{t_n - t_{j-1}} - \sqrt{t_n - t_j} \right] \qquad (26)$$

For this method it was also assumed that each digitized data point occurred at the

29

midpoint of the time interval for consistency. The FORTRAN code for this method is illustrated in Section D.3 of Appendix D.

When the summations in Green's function (Eq. 26) and Duhamel's method (Eq. 19) are expanded and simplified, it can be shown that the two expressions are actually the same. Both expressions were used separately in the data processing for each test and compared. The numerical results from the two expressions were identical to within roundoff error.

Chapter 4.0

Experimental Apparatus and Procedure

This experimental apparatus provides a means to measure surface heat flux and temperature in a turbulent combustion flame using a Heat Flux Microsensor. In addition, the same apparatus is currently used in a senior design laboratory experiment. The design and set-up of the apparatus is discussed in the following two sections. The third section details the experimental procedure. The measurements taken during the experiments are then processed using the data reduction methods of Chapters 2.0 and 3.0.

4.1   Experimental Design

The design of the laboratory apparatus was broken into several parts. The main requirement was the need for a block to house the Heat Flux Microsensor and hold it firmly in place. The block material was selected to be aluminum to provide a close match to the sensor's material. This was done to reduce the conduction effects from the sensor to the housing block. A detailed design of the aluminum sensor support is shown

in Fig. 8. This block had to be suspended using wall and base supports. Because they were not in direct thermal contact with the Heat Flux Microsensor, stainless steel was used as the material for both the wall and base supports. In addition, this material was chosen due to its high temperature capability so it would not soften due to the propane flame. Figure 9 shows the detailed designs of the two wall supports and the base supports. One of the wall supports has been altered so a countersunk allen key bolt could be used to adjust the diameter of the hole holding the Heat Flux Microsensor, allowing it to be held securely in place. The wall supports were mounted to the base of the apparatus using the base supports.

Since the experiment is also utilized as a laboratory procedure, it was crucial to protect the leads coming off of the Heat Flux Microsensor and going to the amplifier. Thus, a sensor box constructed out of sheet metal was designed to cover the wire leads. Figure 10 shows a detailed drawing of the sensor box. A panel mount was placed on top of the sheet metal sensor box so a cable could be used to transmit the signal from the Heat Flux Microsensor to the amplifier box.

In addition, a shutter mechanism was developed to step on and off the impingement of the propane flame. The shutter mechanism was located 2.54 cm (1 in.) from the sensor surface. This mechanism with its slide supports is illustrated in Fig. 11. A total of four slide supports were used to hold the shutter in place, two on the top surface and two on the bottom surface. The slide supports were bolted onto the wall supports as shown in the detailed illustration of Fig. 11.

DRILL AND TAP FOR 1/4-28 UNF-2B
C MIN PERFECT THD DEPTH
TYP. 3 HOLES AS SHOWN

DRILL AND TAP FOR
NO. 10-32 UNF-2B
MIN. PERFECT THD DEPTH G
TYP. 4 HOLES

SENSOR SUPPORT
MATL ALUMINUM ALLOY
I EACH

DRILL AND TAP FOR 3/8-24 UNF-2B
DEPTH   K
C'BORE   L   DIA DEPTH   M
C'BORE   N   DIA DEPTH   O
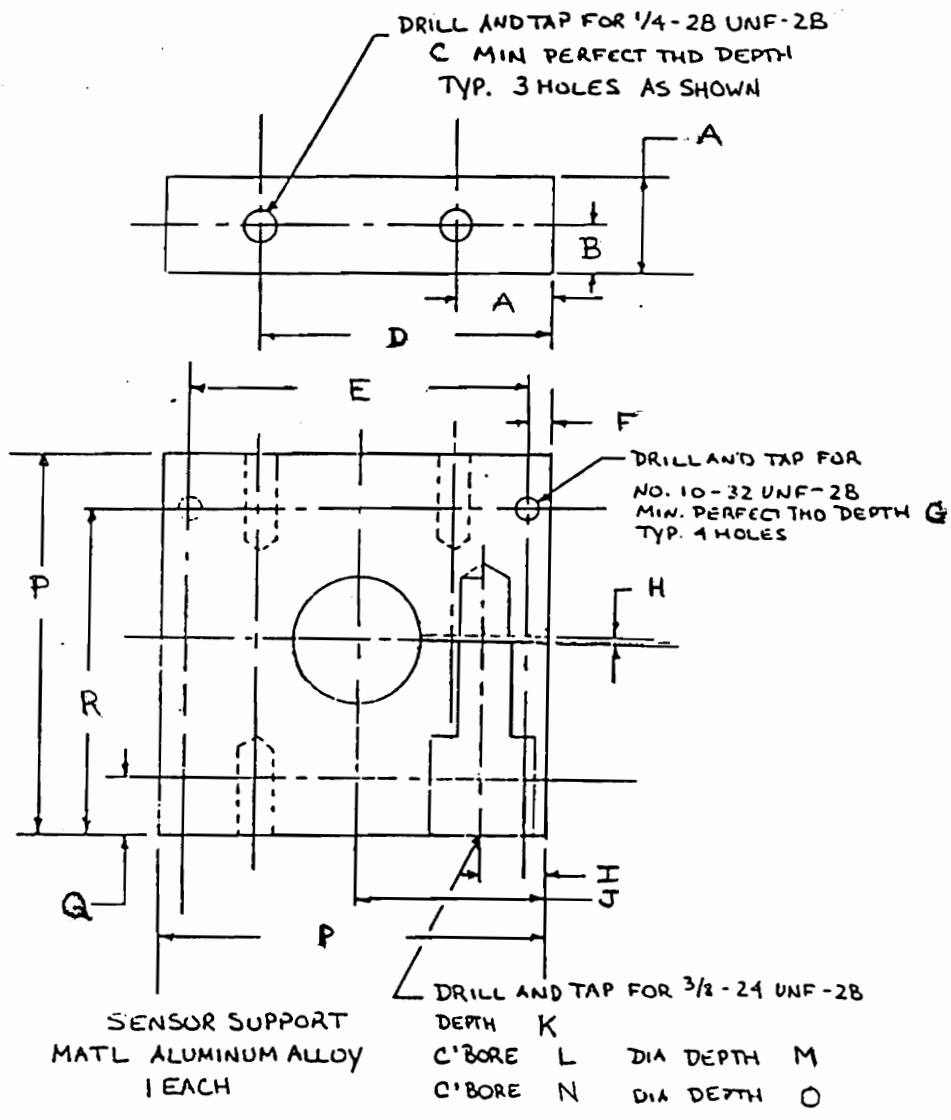
DIMENSIONS GIVEN IN TABLE 4 OF APPENDIX E

Figure 8. Detailed Drawing of Sensor Housing Block

33
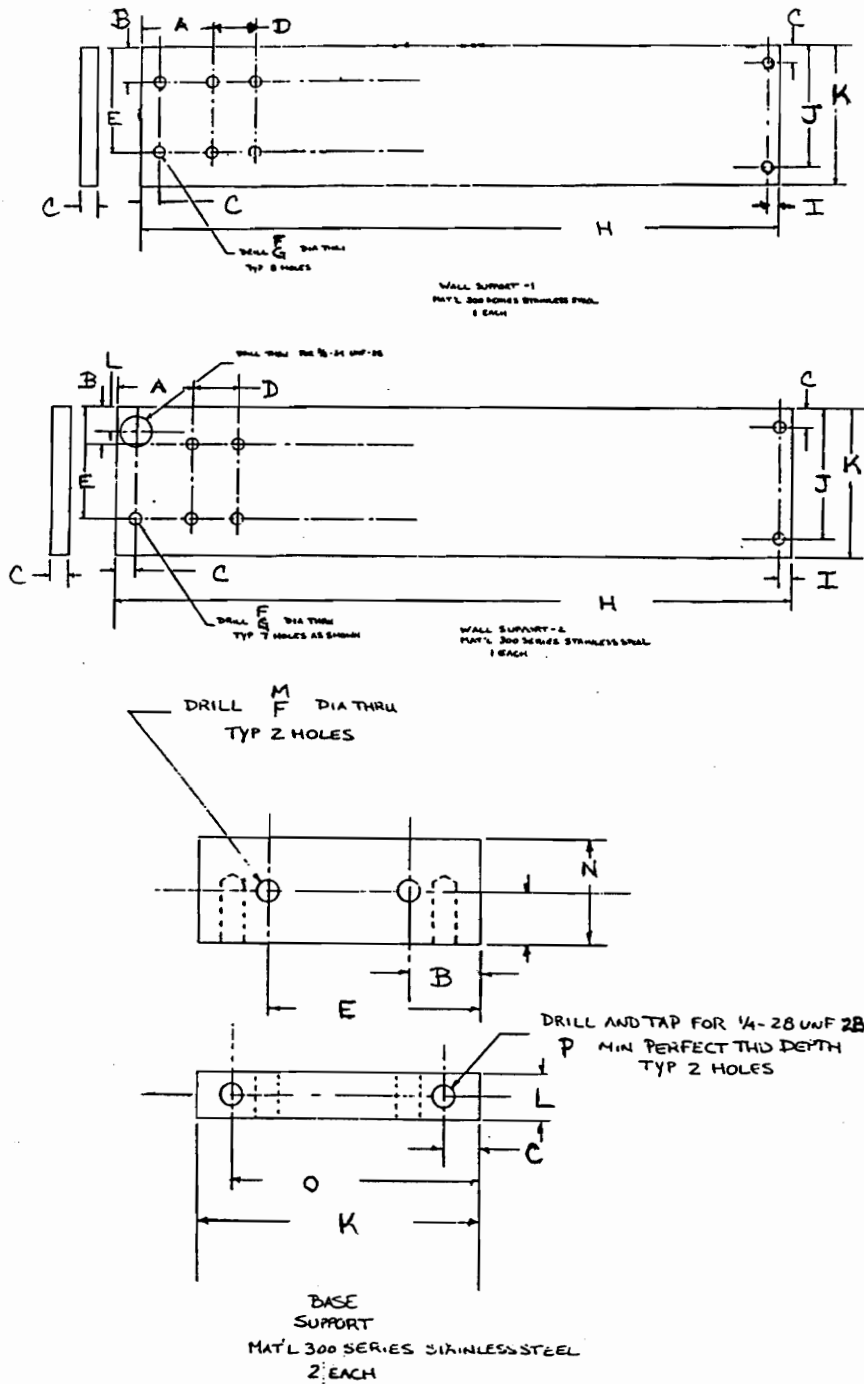
DIMENSIONS GIVEN IN TABLE 5 OF APPENDIX E

Figure 9. Detailed Drawings of Wall and Base Supports

34
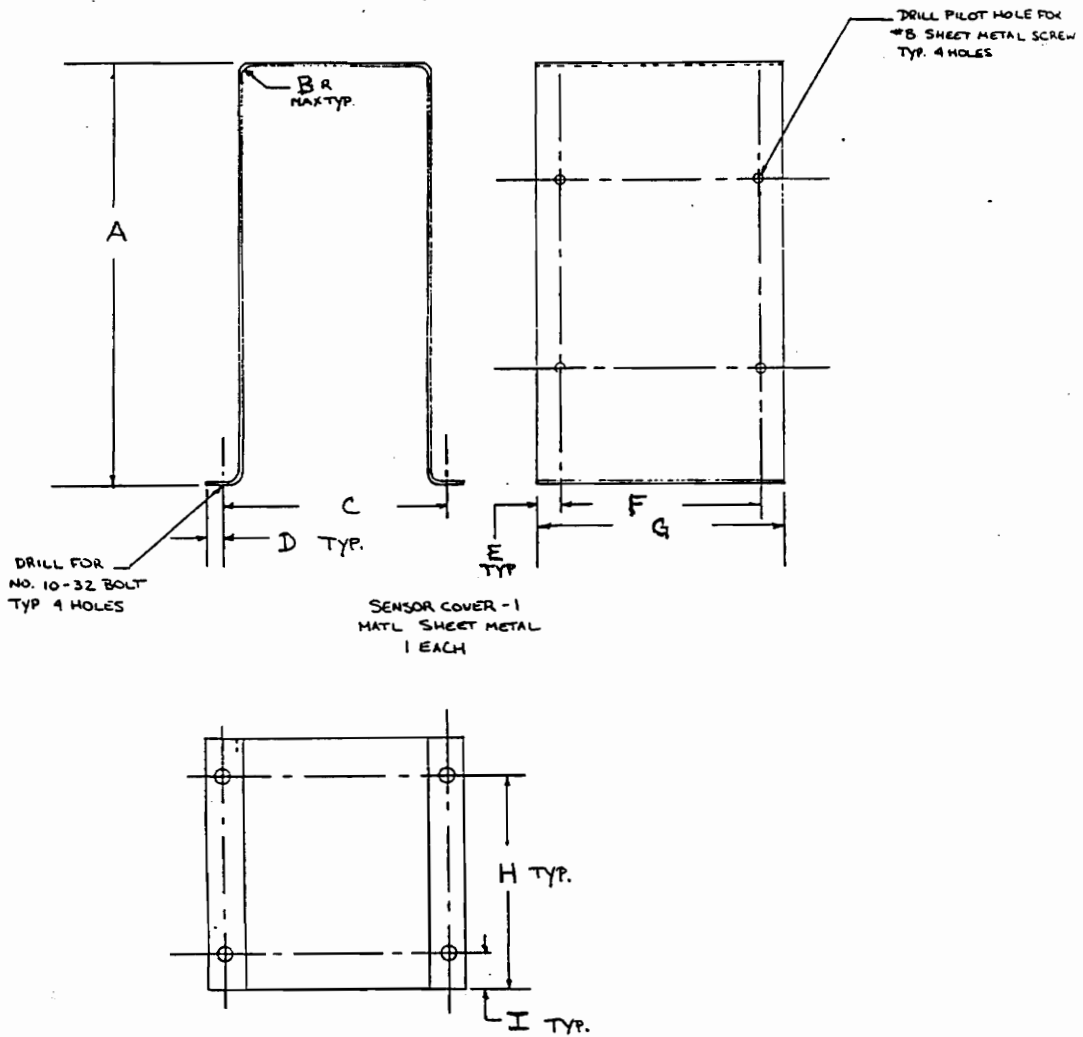
DIMENSIONS GIVEN IN TABLE 6 OF APPENDIX E

Figure 10. Detailed Drawing of Sensor Box
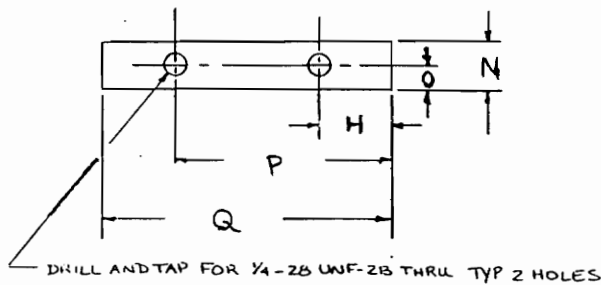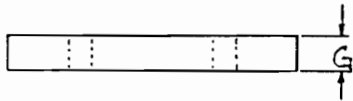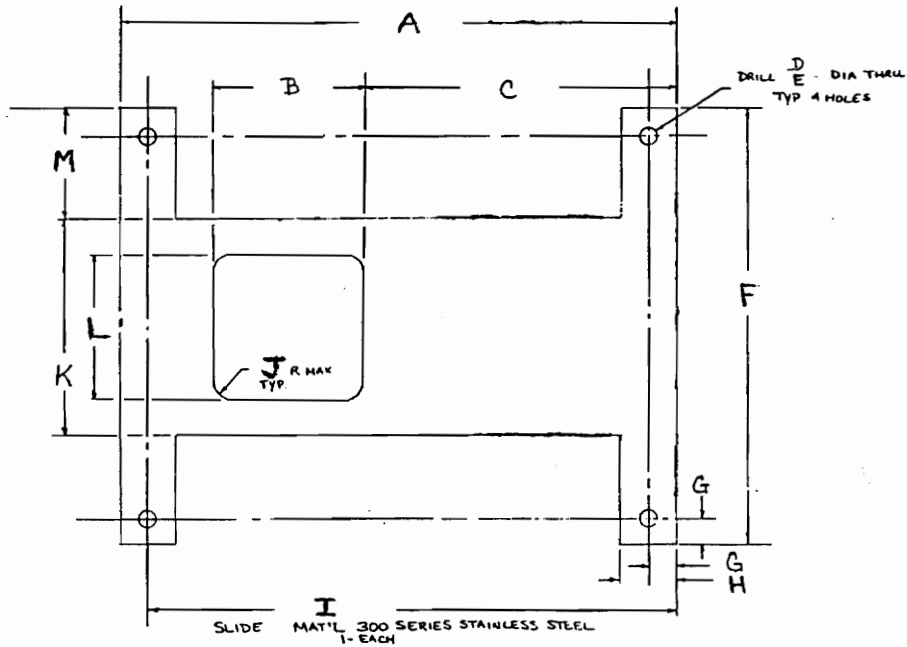
DIMENSIONS GIVEN IN TABLE 7 OF APPENDIX E

Figure 11. Detailed Drawing of Shutter and Slide Supports

36

The entire apparatus was mounted onto a rolling cart to facilitate in relocation. The overall view of the apparatus is shown in Fig. 12. In the next section, the experimental set-up of the apparatus is discussed.

4.2   Experimental Apparatus

The Heat Flux Microsensor was placed in an aluminum block and mounted a fixed distance of 11.59 cm (4.56 in.) from a propane torch as illustrated in Fig. 13. The Heat Flux Microsensor was painted using Krylon ultra-flat black spray to increase the gage's radiation absorptivity. This paint has a reported absorptivity of 0.97 [35].

A Trigger Start 2000 Bernz-O-Matic propane torch was used to produce a turbulent combustion flame. The torch has a release valve that rotates to emit the propane gas. Once the valve is fully opened, there is a trigger button that is pressed to ignite the propane gas. The advantage of this torch is that the fuel/oxygen ratio is already pre-set, requiring no additional adjustments.

Between the torch tip and the sensor surface, a shutter mechanism was placed to step on and off the exposure of the combustion flame to the sensor. This shutter mechanism was detailed in Fig. 11. The shutter was originally designed to operate either manually or by using two springs with an equal spring constant. However, when using the springs there is a tremendous jarring reaction on the device when the shutter is
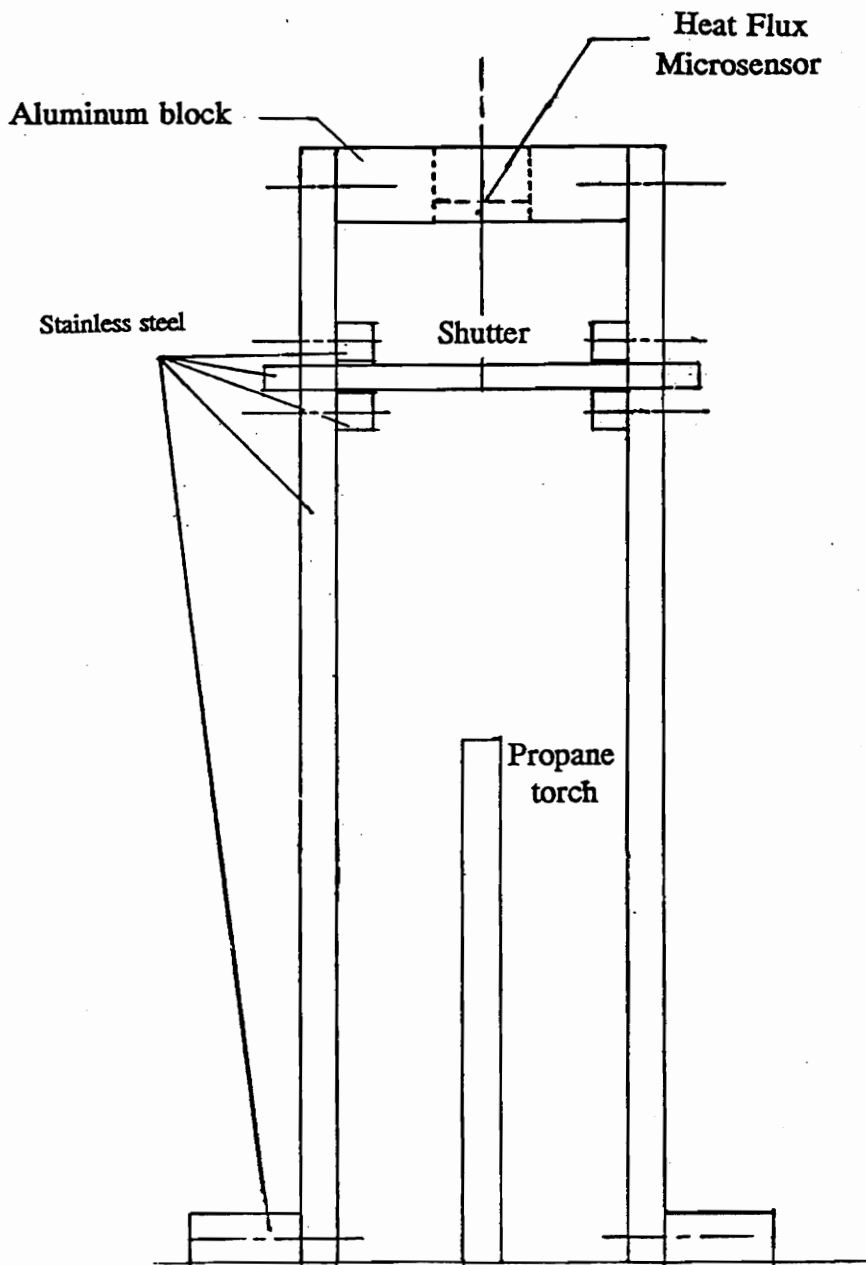
Figure 12. Overall View of Apparatus

38
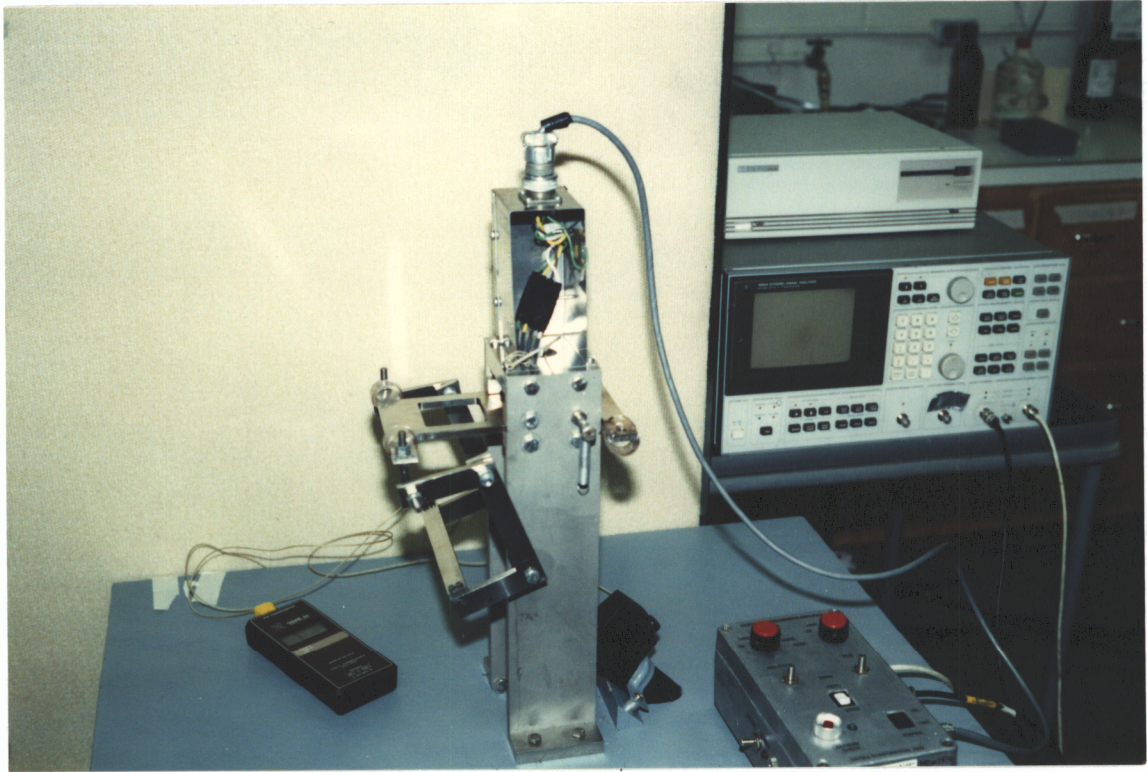
Figure 13. Photograph of Combustion Flame Experimental Set-Up

closed. This type of jarring vibration was not wanted in the apparatus. Thus, the shutter was operated manually, even though this created a lower shutter speed.

The output from the heat flux sensor was amplified 1000 times and the output from the RTS was amplified 200 times using an amplifier built by Vatell Corporation. The heat flux signal was used as the input to Channel 1 and the RTS signal was used as the input to Channel 2 of a Hewlett Packard 3562A dynamic signal analyzer. To reduce the effect of 60 Hz noise, one pin on the panel mount was used as a ground and the lead on that pin was grounded to the sensor box. A ground cable was also attached from the sensor box to the dynamic signal analyzer for the same purpose. Time-resolved heat flux measurements have previously been made with this system by [36,37].

A Type K thermocouple was positioned just below the shutter and in alignment with the sensor and the propane torch tip to monitor flame temperature. The thermocouple was read using a Tegam, Inc. Model 878 Type K thermocouple digital readout meter.

4.3   Experimental Procedure

After the Heat Flux Microsensor was positioned inside the aluminum housing block and all the leads and cables were connected, the amplifier built by Vatell Corporation was turned on and the switch denoting a test or calibration was pressed to

the calibration side. Using the dynamic signal analyzer and the amplifier, the output from both the Heat Flux Microsensor and the RTS was zeroed. Then, the switch was pressed to the test side in order to enable the amplifier for measurement.

With the shutter closed, the torch was ignited and adjusted to the desired flame height. This flame height corresponded to a flame temperature of approximately 1120 °C, which through trial and error was determined to be the flame temperature for maximum flame stability. The shutter was then manually opened to allow flame impingement onto the surface of the sensor for a predetermined time length. When the sensor had been exposed the desired length of time, the shutter was manually closed and the propane torch was turned off.

Tests were run for total times of 20 sec and 0.800 sec. The latter time length was run using the trigger mechanism on the Hewlett Packard dynamic signal analyzer. The trigger was set for a voltage output from the heat flux signal of -50 mV and a delay of 0.10 sec in order to capture a portion of the signal prior to the shutter opening. From the 0.800 sec heat flux traces it was determined that the shutter was fully opened in approximately 20 msec.

A convection calibration was performed to determine the sensitivity of the Heat Flux Microsensor. The sensitivity was used to calculate heat flux from the voltage output of the sensor. Details of the calibration procedure are given in Appendix A. The sensitivity defined by

$$S_q = \frac{E_q}{q} \qquad (27)$$

was $S_q = 23.2 \, \mu V/(W/cm^2)$. The 95% confidence interval for the sensitivity calculation

had an error of ± 8 percent compared with an estimated error of ± 10 percent.

Calibration of the temperature response was also performed. The procedure for

the RTS calibration is discussed in Appendix B. A linear regression was used to obtain

$$T = 330.83 \left[\frac{°C}{V} \right] E_T - 291.06 \, °C \qquad (28)$$

This curve was used to calculate temperature from the RTS voltage output.

Chapter 5.0

Results

Time-resolved heat flux and RTS measurements were taken for two different time duration tests. Samples of the time-resolved heat flux and RTS measurements for the longer time duration test, 20 sec, and the shorter time duration tests, 0.800 sec are shown in Figs. 14, 15, and 16. An example of the time-resolved heat flux and surface temperature measurements for the 20 sec test is shown in Fig. 14. For the shorter time duration, two separate tests were run. The first short duration test was conducted with the flame adjusted for a medium flame height and maximum flame stability. The flame temperature for this test was approximately 1120 °C. Time-resolved signals from the Heat Flux Microsensor and RTS were measured and recorded. These are shown in Fig. 15. The second short time duration test was also conducted with the flame adjusted for a medium flame height. However, it was purposely operated in an unstable mode. There was considerable audible noise associated with the combustion instabilities that were not present for the other tests. The time-resolved measurements of heat flux and RTS signals were recorded for this test and are illustrated in Fig. 16.

In order to compare the actual heat flux signal recorded from the Heat Flux Microsensor with the signal analytically calculated using the method detailed in Chapter
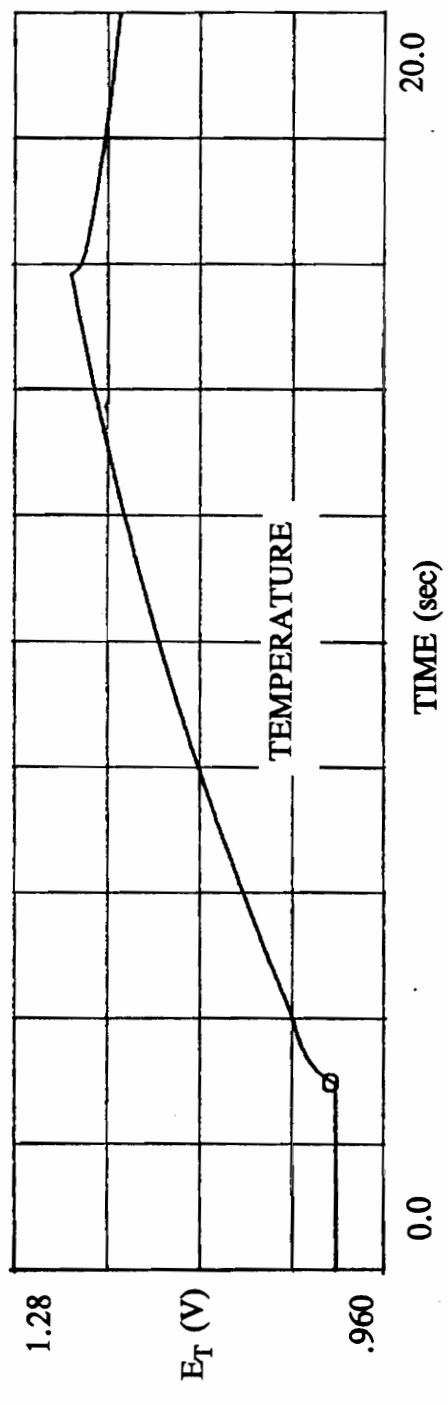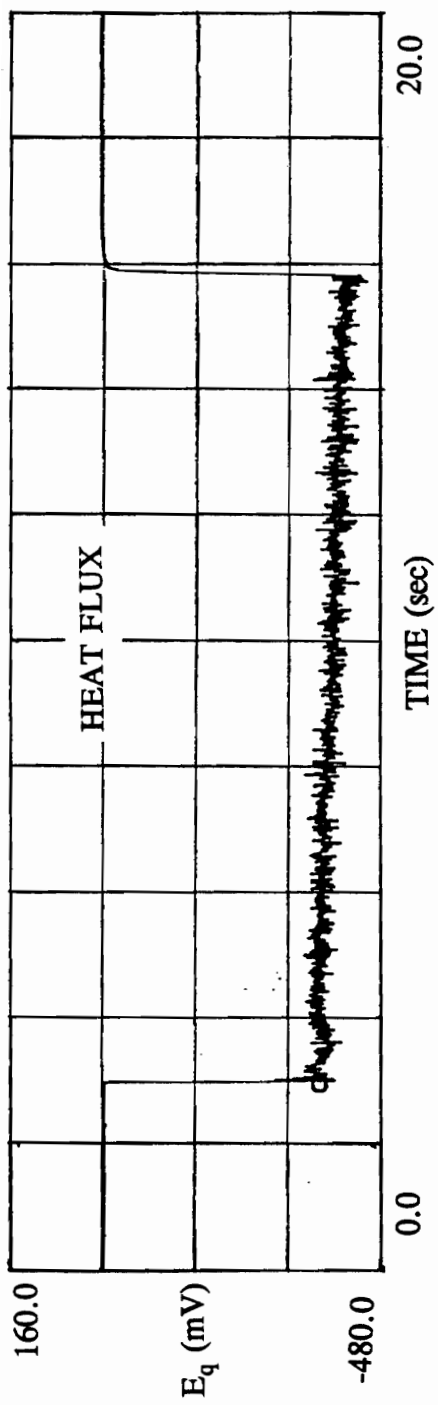
Figure 14. Time-Resolved Heat Flux and RTS Measurements for 20 Sec Test

44
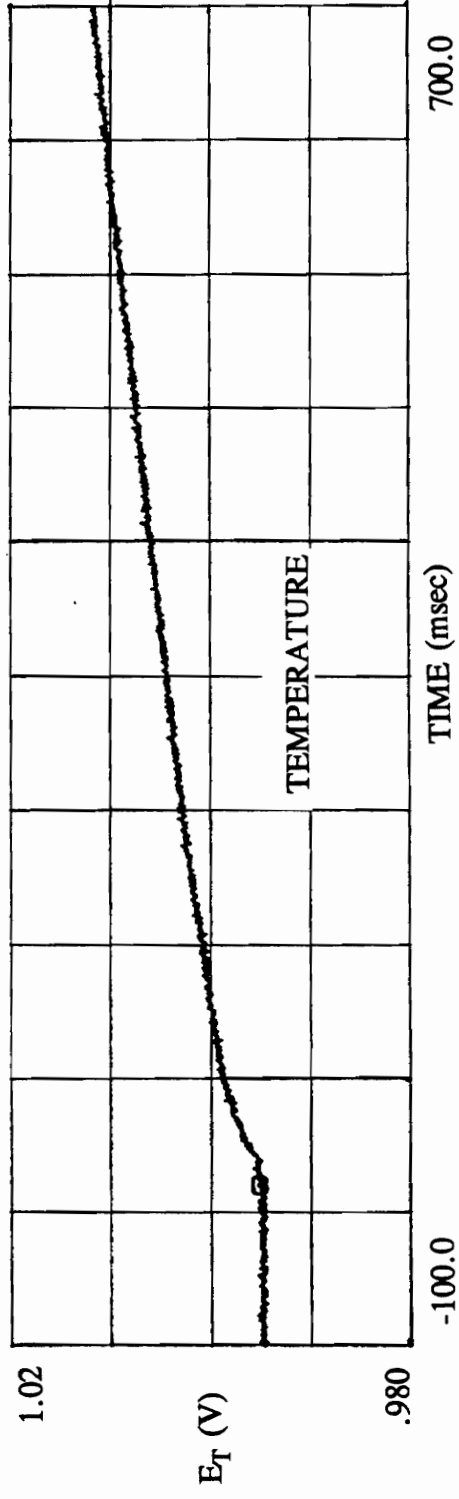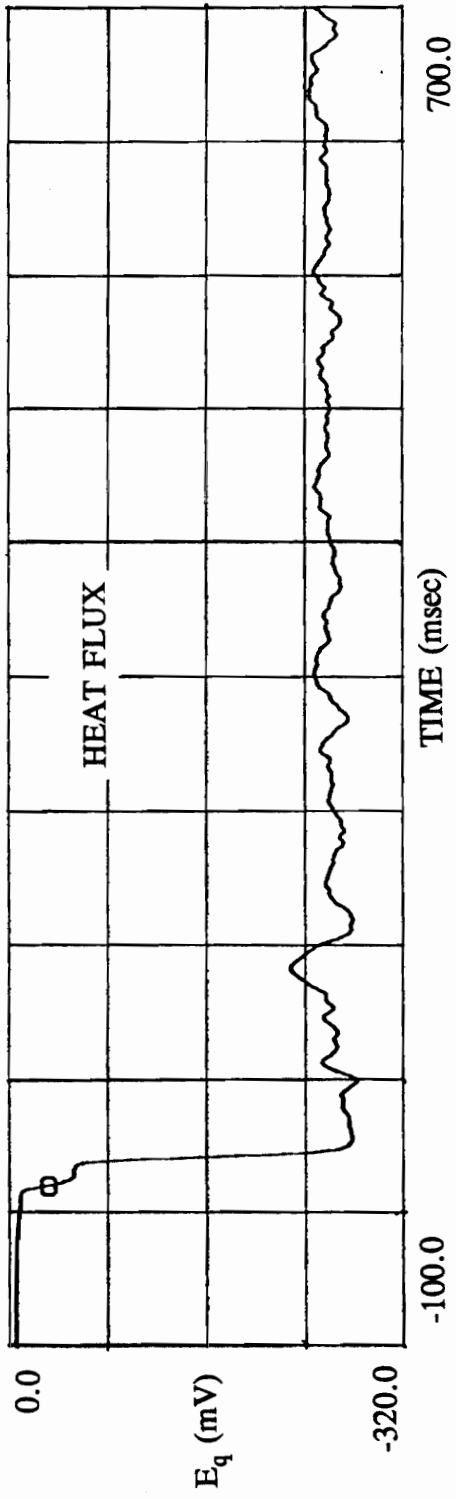
Figure 15. Time-Resolved Heat Flux and RTS Measurements for First 0.800 Sec Test

45
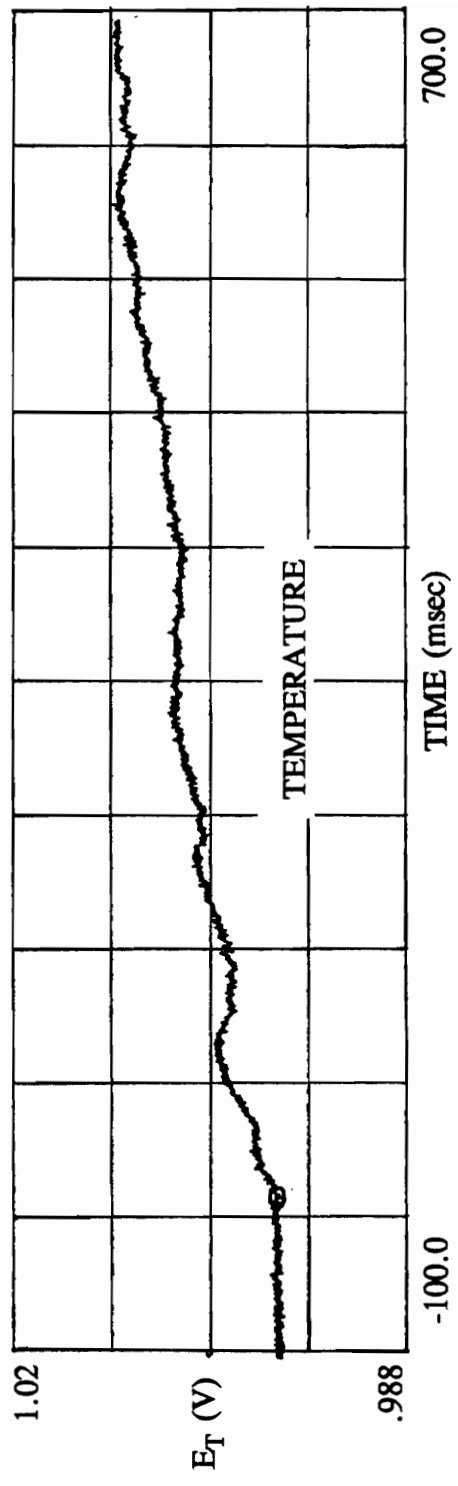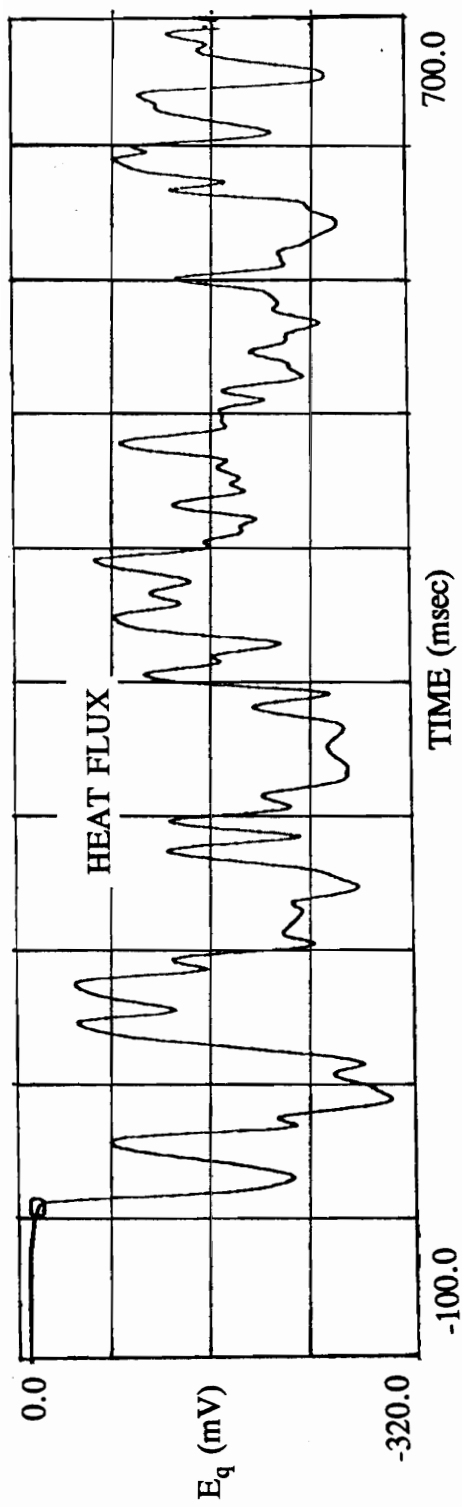
Figure 16. Time-Resolved Heat Flux and RTS Measurements for Second 0.800 Sec Test

2.0 and to compare the actual surface temperature signal recorded by the RTS with the signal analytically determined using the methods detailed in Chapter 3.0, the properties of the sensor substrate were needed. Based on information given by the manufacturer, the following properties of aluminum nitride were used:

$$k = 170 \text{ W/m} \cdot \text{K}$$

$$C = 670 \text{ J/kg} \cdot \text{K}$$

$$\rho = 3260 \text{ kg/m}^3$$

$$\alpha = 7.78 \times 10^{-5} \text{ m}^2/\text{s}$$

For each test, the surface temperature signal measured by the RTS was digitized into 2048 singular data points by the HP dynamic signal analyzer. A Hewlett Packard program, LIF, converts Hewlett Packard files into ASCII files so that the data can be used in numerical programs and in spreadsheets. Similarly, the heat flux signal measured by the Heat Flux Microsensor was converted into an ASCII file.

For the 20 sec duration test, the HP dynamic signal analyzer filtered out frequencies greater than 40 Hz using an internal low-pass filter. The center of the frequency span was 20 Hz and the band width was 75 mHz. Figure 17 graphically represents the results of using the digitized surface temperature signal to calculate heat flux by the analytical methods detailed in Chapter 2.0. The FORTRAN program written

47
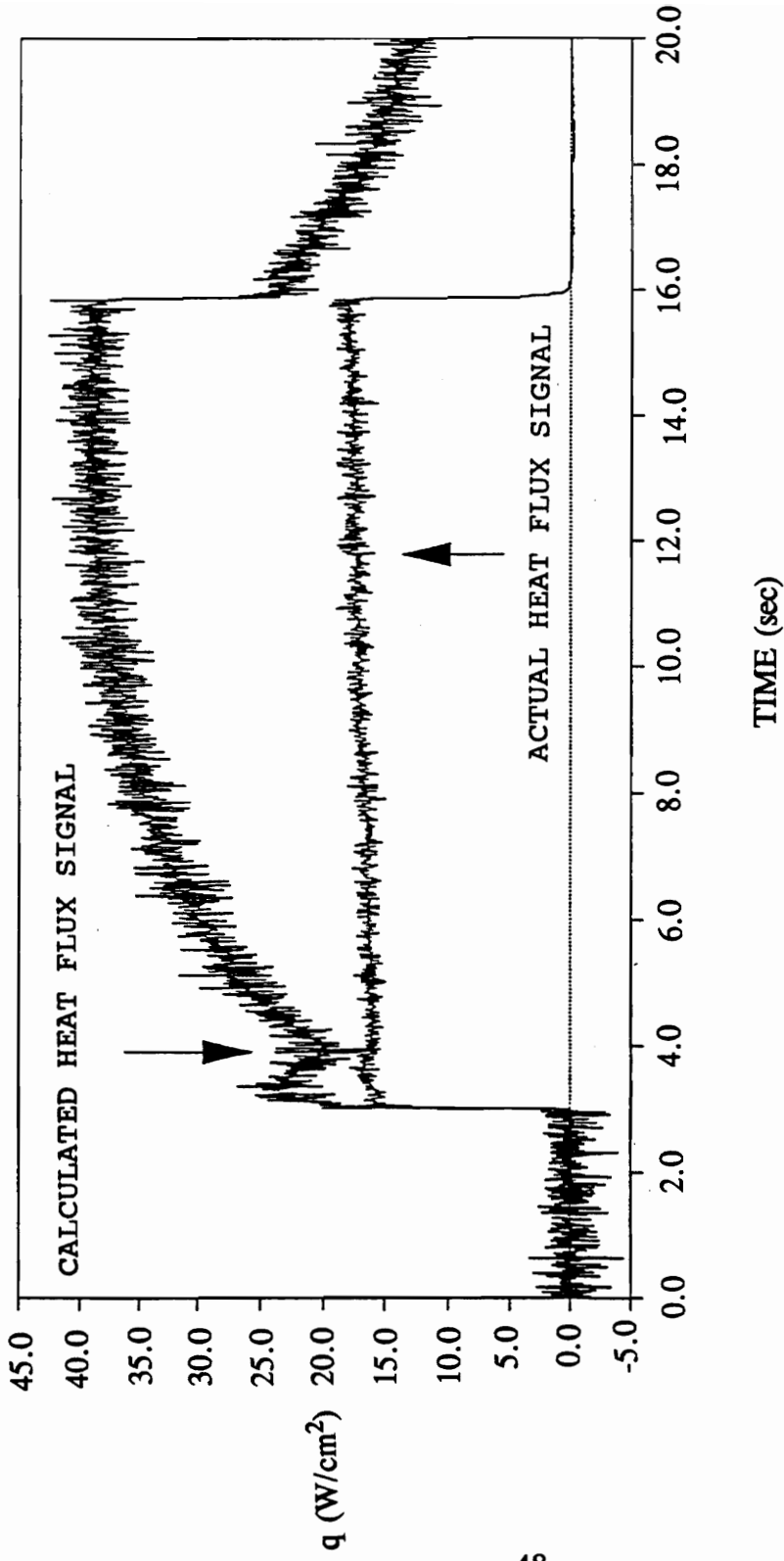
Figure 17. Heat Flux Traces for 20 Sec Test

48

to perform this method is listed in Appendix D. Conversely, Fig. 18 graphically illustrates the results of using the digitized heat flux signal to calculate surface temperature by the methods described in Chapter 3.0 for the same test. The FORTRAN programs written to perform both methods are also listed in Appendix D. It should be noted that since both integration methods yield the same result, they appear as a single line in the graph.

The same procedure was used for the two short duration time tests. For the 0.800 sec tests, the low-pass filter on the HP dynamic signal analyzer filtered out frequencies higher than 1 kHz. The center of the frequency span was 500 Hz and the band width was 1.87 Hz. The results using of converting surface temperature measurements to heat flux values for the two short duration time tests are shown in Figs. 19 and 21. The results of the converse process of converting heat flux measurements to surface temperature values are illustrated in Figs. 20 and 22.

The frequency spectra was also investigated for each of the tests. However, there were no sharp spikes discernable. Only broad band noise was present in the frequency spectra of each test.
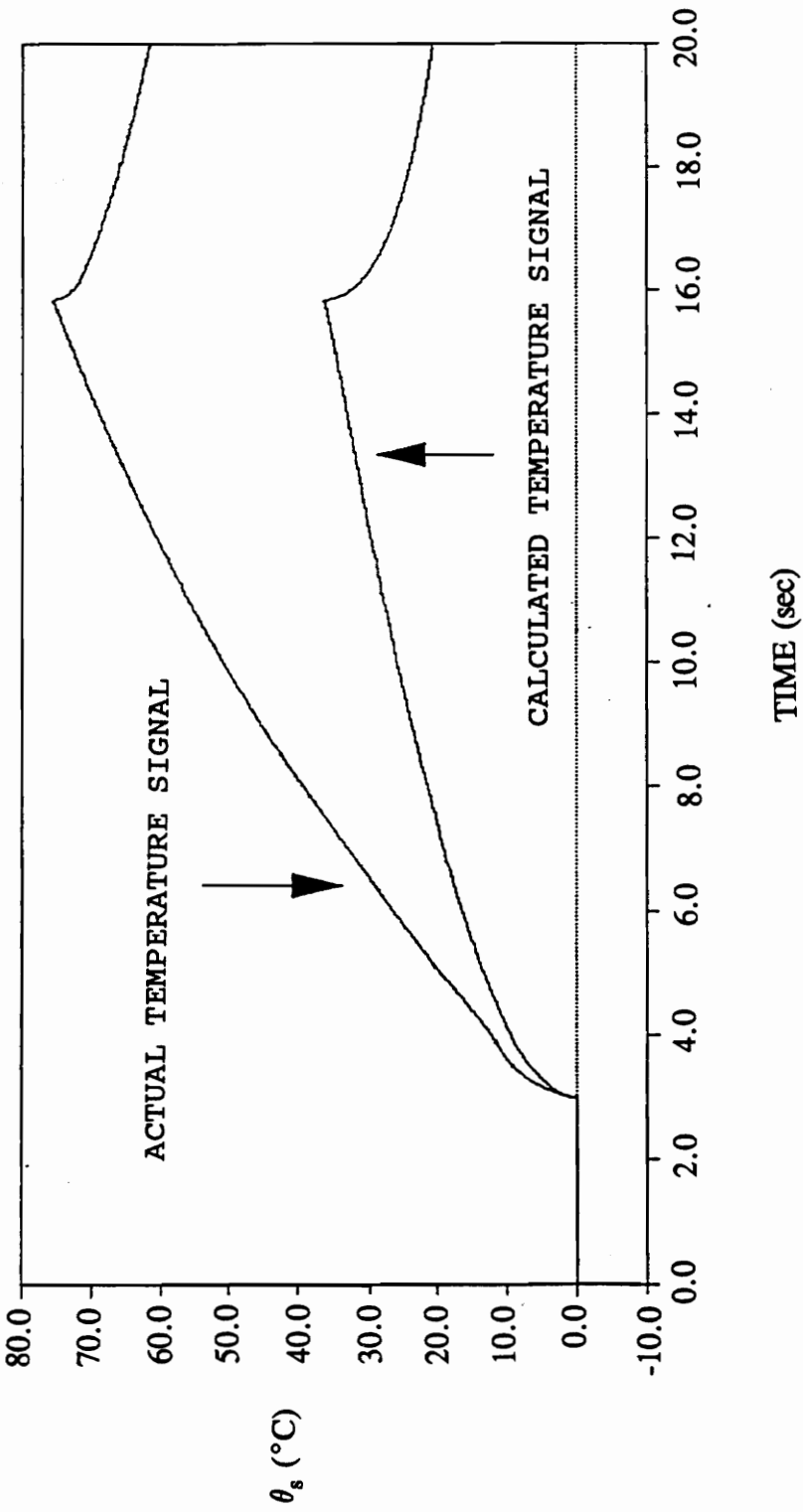
Figure 18. Temperature Traces for 20 Sec Test

50
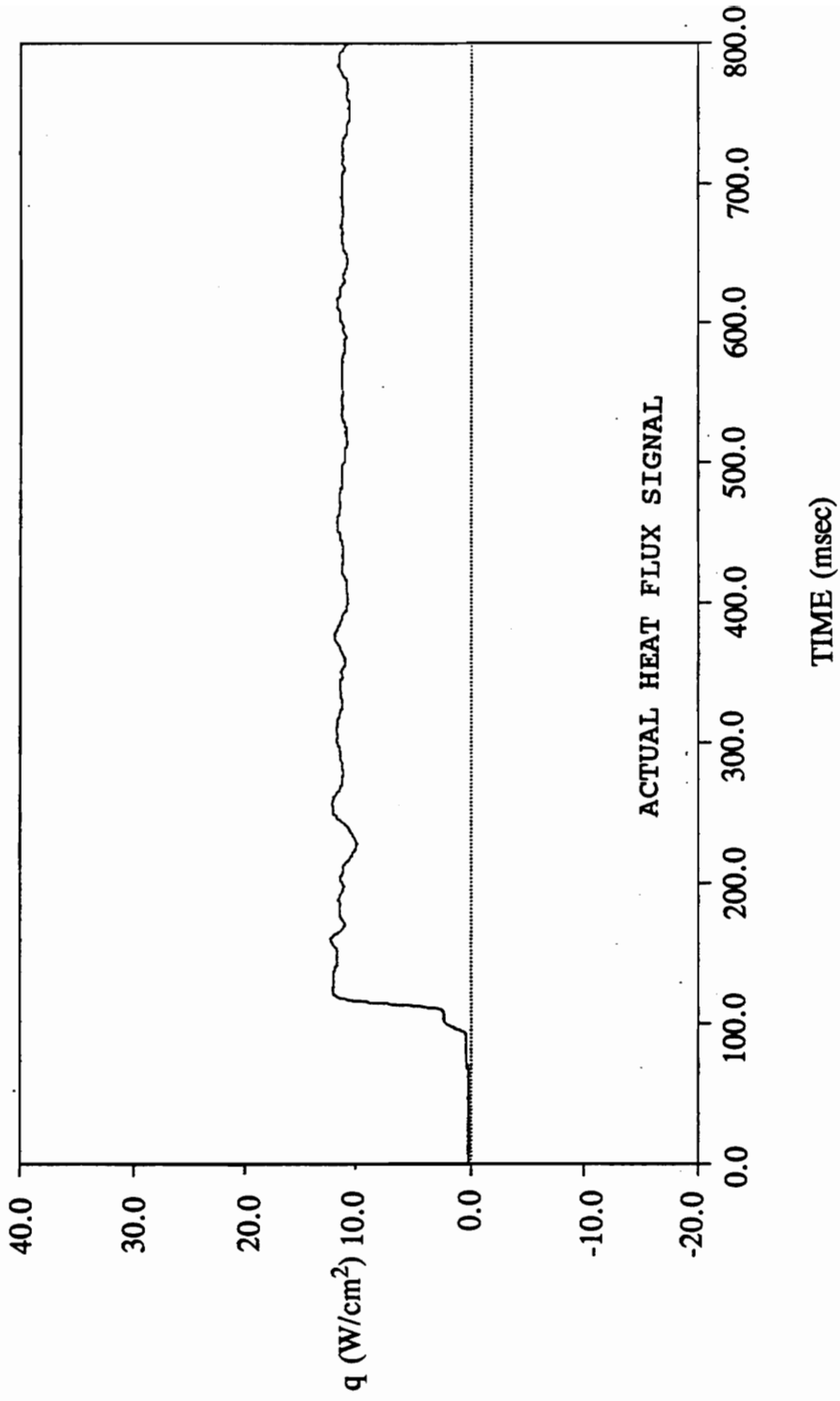
Figure 19. Heat Flux Traces for First 0.800 Sec Test

a) Heat Flux Microsensor Trace
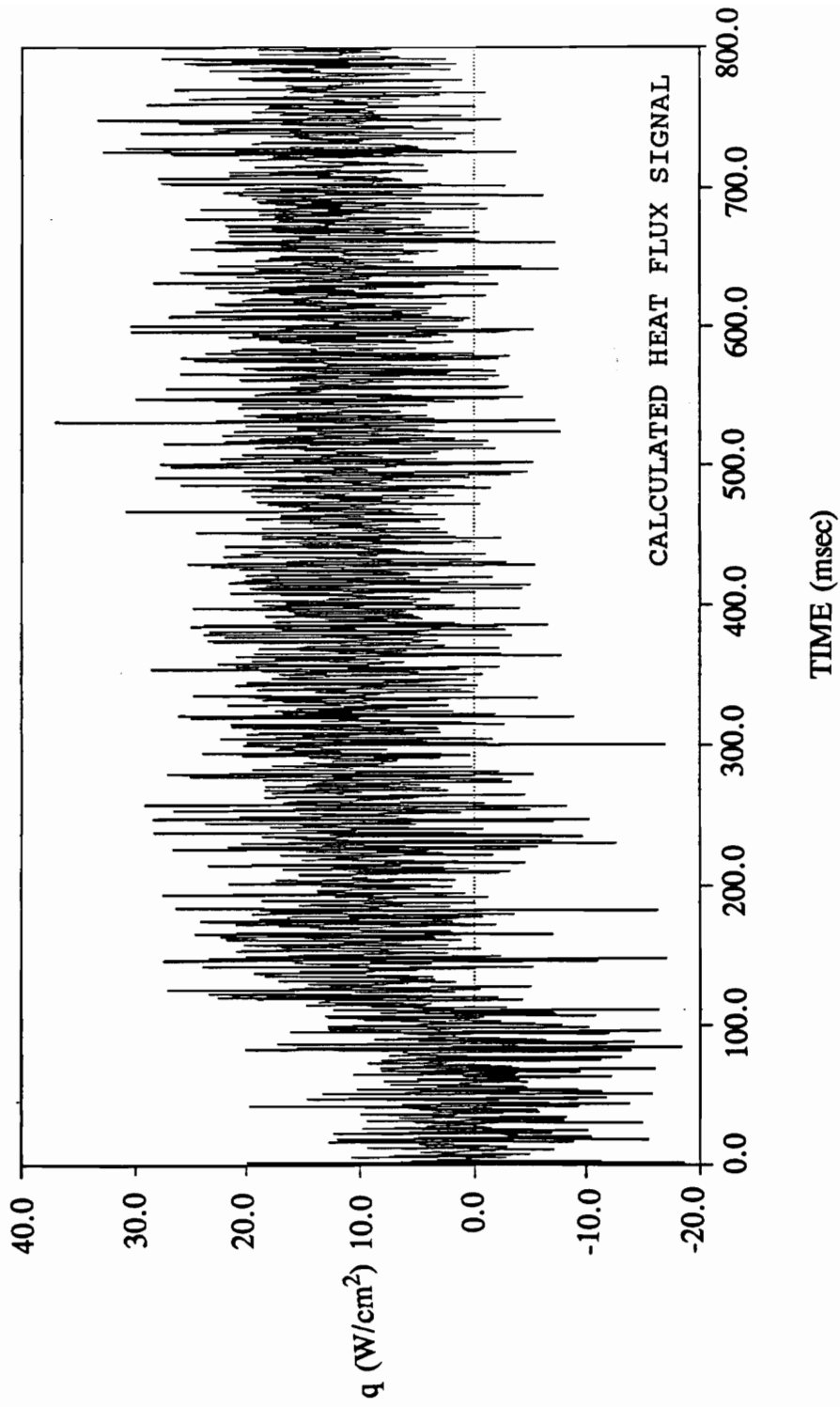
Figure 19. Heat Flux Traces for First 0.800 Sec Test

b) Heat Flux Trace from Temperature Output
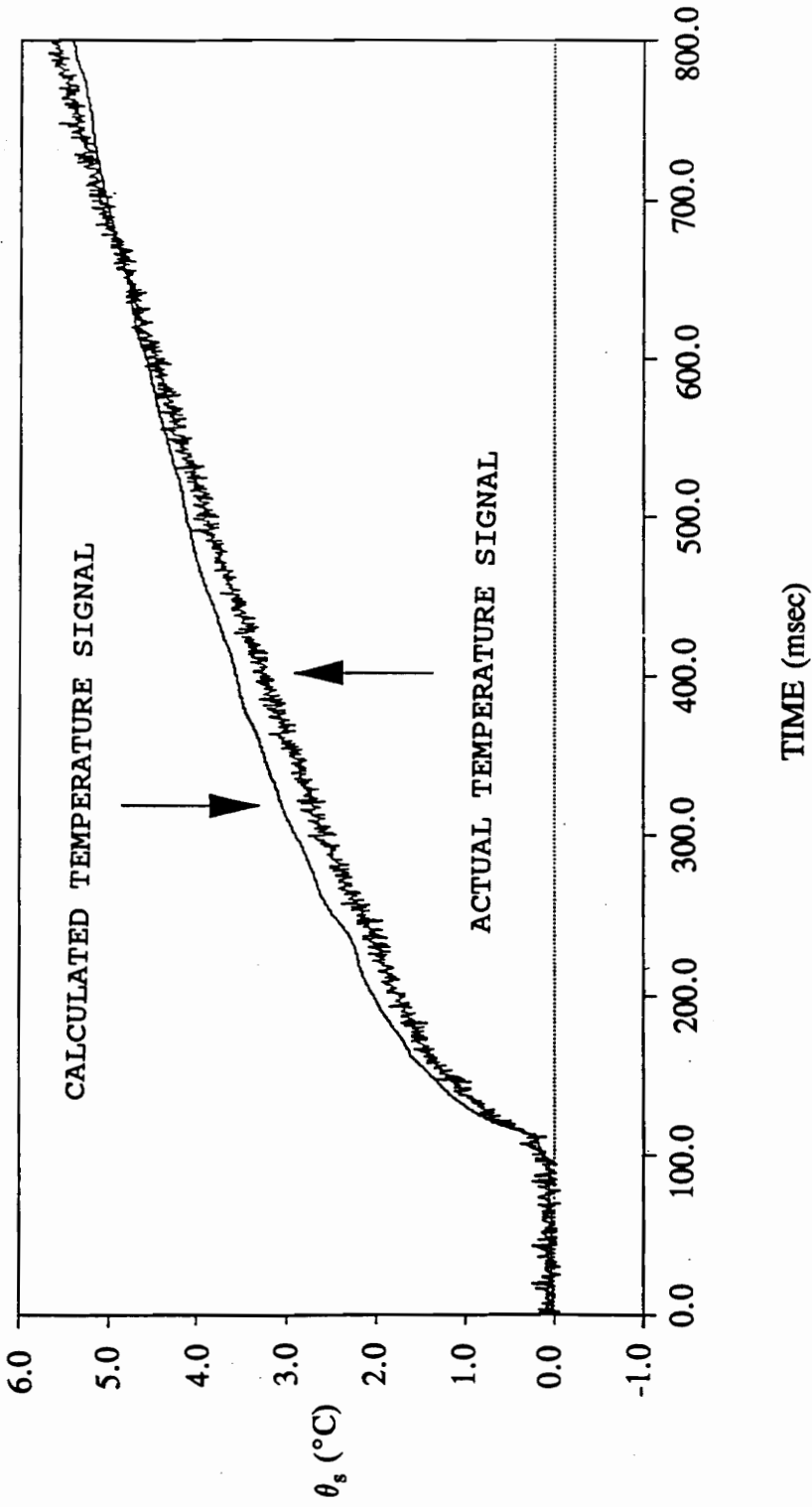
Figure 20. Temperature Traces for First 0.800 Sec Test

53
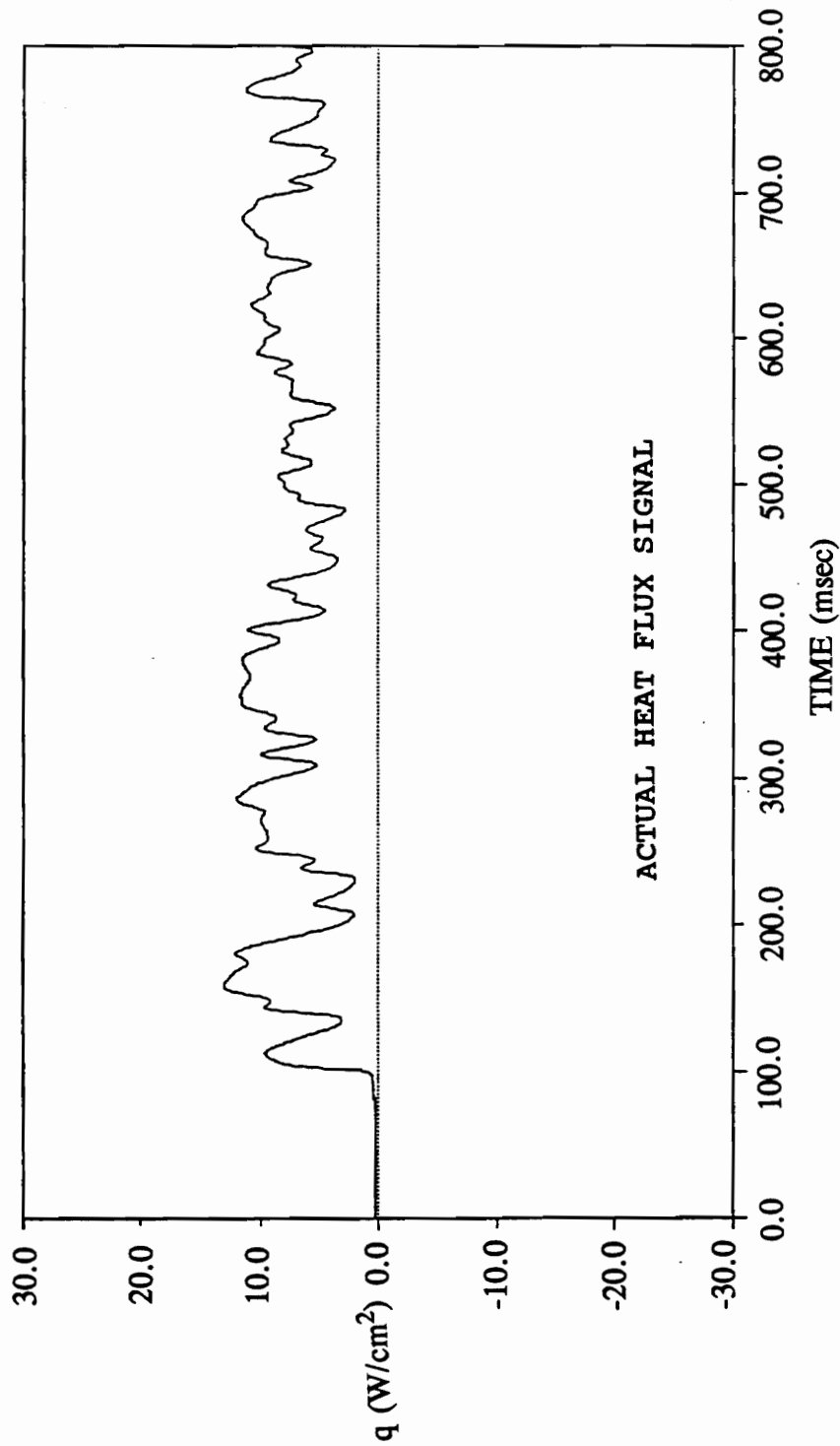
Figure 21. Heat Flux Traces for Second 0.800 Sec Test

a) Heat Flux Microsensor Trace

54
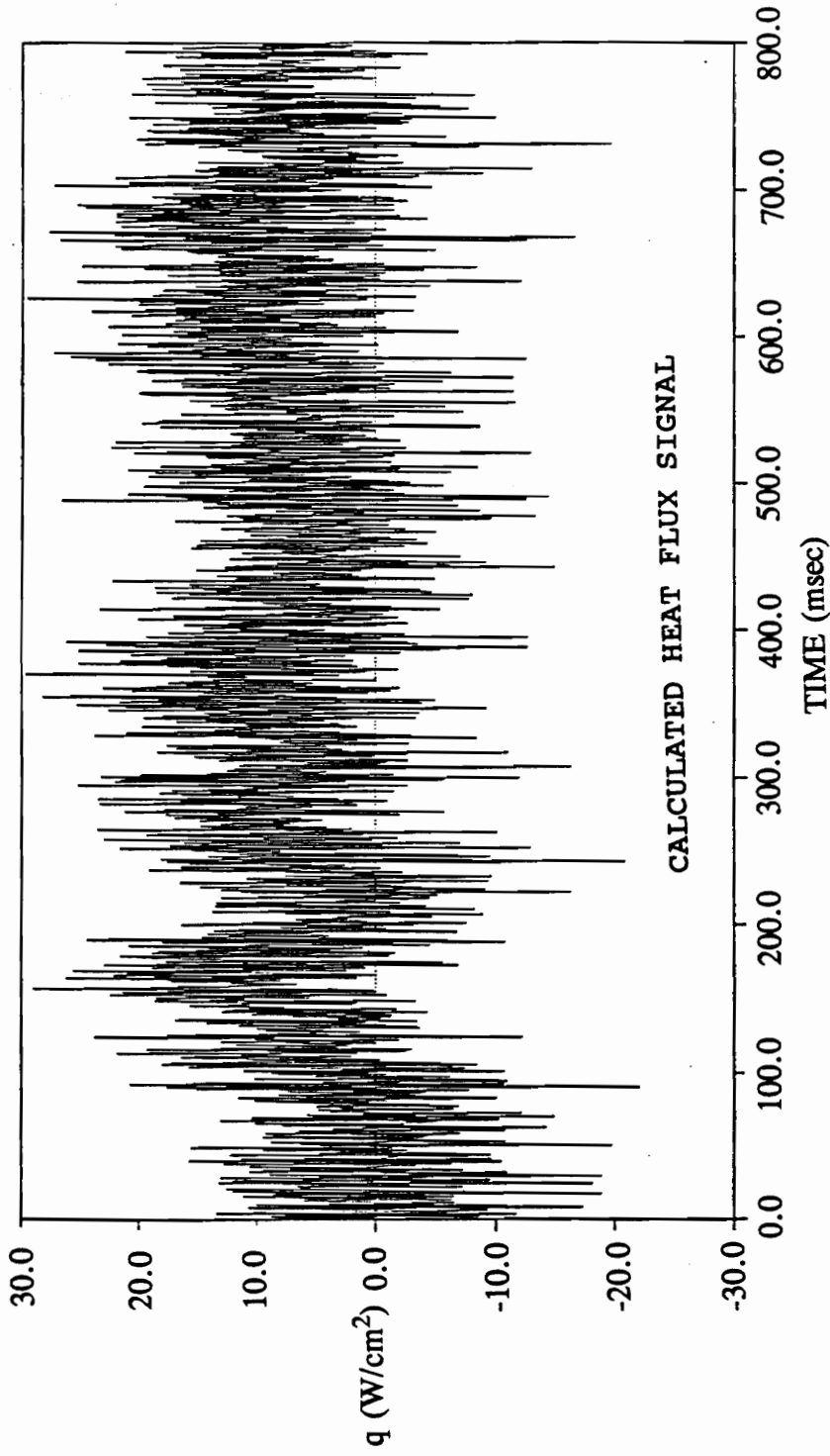
Figure 21. Heat Flux Traces for Second 0.800 Sec Test

b) Heat Flux Trace from Temperature Output

55
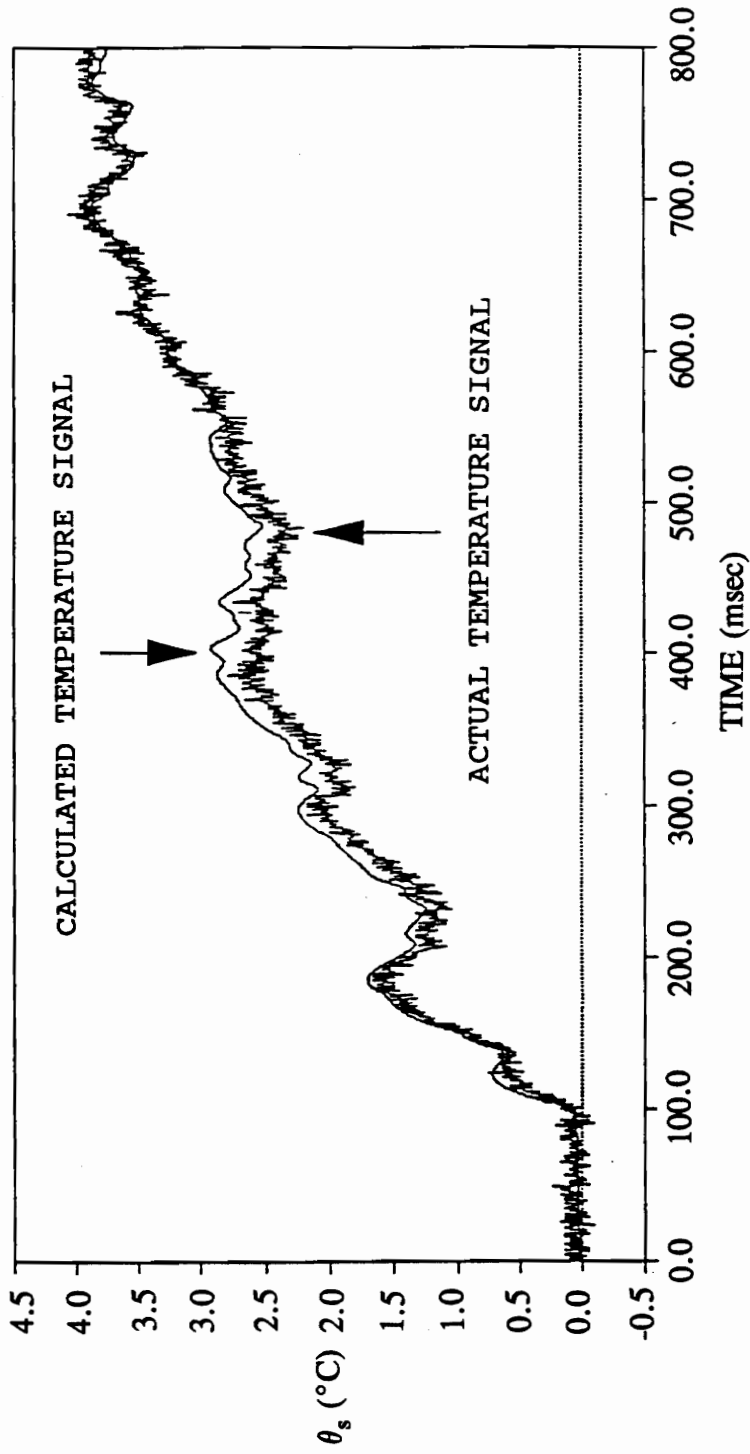
Figure 22. Temperature Traces for Second 0.800 Sec Test

56

Chapter 6.0

Discussion of Results

Measurements were conducted in a turbulent combustion flame to simulate a useful industrial application. Both heat flux and surface temperature measurements were made so a comparison between the actual unsteady heat flux signal and the heat flux trace obtained from the RTS temperature signal using the numerical expression of Eq. 15 could be made. In addition, the actual unsteady surface temperature signal and the surface temperature trace obtained from the Heat Flux Microsensor were compared using the numerical expressions of Eq. 19 and Eq. 26. The tests were conducted for different time intervals in order to evaluate how the length of test time affected the results.

6.1   Time-Resolved Measurements

The time-resolved signals are shown in Figs. 14, 15, and 16. The top graph in each figure is the unsteady heat flux signal as recorded by the Heat Flux Microsensor. As illustrated, each time-resolved heat flux trace demonstrates that the heat flux caused from impingement of the propane flame onto the sensor is relatively constant with the

exception of Fig. 16. In this case, the measured heat flux signal is not constant due to the presence of combustion instabilities in the flame. The bottom graph in each figure is the transient surface temperature signal as recorded by the RTS. These graphs illustrate that surface temperature increases proportional to the square root of time.

In the 20 sec duration time test shown in Fig. 14, the transient temperature curve is smooth. Since the time length is longer, the 60 Hz noise is filtered by the signal analyzer. However, for the 0.800 sec duration time test, this noise is no longer filtered out. Thus, the transient temperature signals shown in Figs. 15 and 16 are much noisier. Also, the unsteady heat flux signal for the 20 sec test in Fig. 14 has more noise than the shorter duration tests. However, there is a noticeable unsteadiness in the 0.800 sec duration tests of Figs. 15 and 16.

6.2   Results for Cook and Felderman's Method

Cook and Felderman's method described in Chapter 2.0 takes the actual transient temperature signal and differentiates it with respect to time using the numerical expression of Eq. 15 to yield heat flux. The results of this method are compared with the actual heat flux signal for all three tests.

The correlation between the actual unsteady heat flux signal and the heat flux trace obtained from the temperature signal for the 20 sec duration test is illustrated in

Fig. 17. Two important observations can be made. First, it is obvious that the signal calculated through the use of the transient temperature measurements is noisier than the actual recorded heat flux trace. Second, the calculated curve does not accurately predict the actual unsteady heat flux. The calculated heat flux trace over-predicts the actual signal by approximately 20 W/cm^2 by the end of the test. Since the sensor is modeled as a semi-infinite material, the conduction solution for this type of material is only valid for the time interval

$$t \cong \frac{L^2}{16\alpha} \qquad (29)$$

This is the amount of time prior to the thermally affected zone (1% temperature change) reaching the back surface of the substrate [26]. The corresponding time for the 6.3 mm thick aluminum nitride substrate is only 32 msec. As a result, the high heat flux predicted from the temperature signal is explainable because of the finite thickness of the substrate. This illustrates one of the main limitations of using these methods to calculate heat flux.

Figures 19 and 21 illustrate the correlation between the actual unsteady heat flux signal and that calculated using the temperature trace in the differentiation method expressed in Eq. 15 for the 0.800 sec tests. Both figures are broken into two plots because of the noise generated from the temperature signal masks the actual heat flux measurement. As discussed earlier in this chapter, the 60 Hz noise is no longer filtered by the signal analyzer. The small amount of electrical noise evident in the temperature

signals of Figs. 15 and 16 is amplified by the signal processing of Eq. 15. Many points of negative heat flux are even indicated. For the first 0.800 sec test when the flame was adjusted for medium flame height and maximum flame stability, the heat flux from the flame was nearly constant throughout the duration of the test. This is illustrated in Fig. 19. However, for the second 0.800 sec test when the flame was adjusted to operate in an unstable mode, the heat flux shown in Fig. 21 is clearly unsteady.

6.3   Results for Integration Methods

The integration methods, Duhamel's method and Green's function, take the unsteady heat flux signal measured by the Heat Flux Microsensor and integrate it with respect to time to yield a transient temperature trace. The FORTRAN programs of Appendix D are used to perform the required summation for Duhamel's method and Green's function shown in Eqs. 19 and 26, respectively.

Figure 18 shows these methods of integrating the unsteady heat flux measurements to obtain a transient temperature signal for the 20 sec duration test. The actual transient temperature signal and the one obtained using the unsteady heat flux trace are both clean signals. In addition, the calculated transient temperature trace under-predicts the actual signal over most of the test. This is attributed to the limitations of approximating the sensor's substrate as a semi-infinite material when it actually has a finite thickness.

60

Much more heat flux is assumed to enter the semi-infinite substrate than is possible with the finite thickness. For the first fraction of a second, however, the two signals appear to correlate well. This observation led to performing tests that were less than one second in duration to illustrate the effect of test time length on the results. As mentioned on page 49 of Chapter 5.0, Duhamel's method and Green's function yield the same result. Thus, the two methods appear as a single line and the resulting values of the 2048 time steps for each method only differ from roundoff error from the computer processing. For the 20 sec test, the roundoff error for the two methods was within $\pm$ 0.00015 °C.

The first 0.800 sec test results for the integration methods are shown in Fig. 20. This figure demonstrates the correlation between the actual temperature signal and the one calculated through integration of the unsteady heat flux trace. As shown, the calculated trace predicts quite accurately the actual transient temperature distribution. Using Duhamel's method and Green's function, the resulting values for the 2048 time steps for this test had a roundoff error within $\pm$ 0.00002 °C. Toward the end of the trace the integration from the heat flux measurement is beginning to under-predict the temperature measurement because of the aforementioned substrate finite thickness effect. Even though the semi-infinite conduction model is not valid after a time of 32 msec, the heat flux is accurate to within 1% for times to 0.3 L^2/α, which corresponds to 155 msec. Thus, for this time duration, the models using Duhamel's method and Green's function are accurate in predicting transient temperature responses.

Another 0.800 sec test was run with the combustion flame adjusted to operate in

an unstable mode to observe results with greater unsteadiness in the signals. The results using the integration methods are shown in Fig. 22. It is interesting to note how well the temperature prediction from the unsteady heat flux signal follows the actual changes in the temperature curve. Using the integration methods, the resulting values for each time step agreed to within ± 0.00001 °C for this test. Also, the temperature signal even experiences temporary decreases in temperature corresponding to the times of very low heat flux associated with the combustion instabilities. As in Fig. 20, the heat flux signal gives a temperature signal with even less noise than the original signal from the temperature sensor.

Chapter 7.0

Conclusions and Recommendations

7.1   Conclusions

The Heat Flux Microsensor has the capability of measuring surface temperature and heat flux simultaneously. This ability allowed for comparisons of experimental surface temperature and heat flux. Using the Heat Flux Microsensor in a turbulent combustion flame, the temperature signal was used to calculate heat flux and the heat flux signal was used to calculate temperature, assuming a one-dimensional semi-infinite model of the gage's substrate.

Two numerical procedures were developed for using unsteady heat flux measurements to predict the corresponding surface temperature as a function of time for a semi-infinite substrate. In addition, a standard method was used for converting transient temperature measurements to the corresponding unsteady heat flux for a semi-infinite substrate. These methods were successfully used on simultaneous measurements of heat flux and surface temperature during transient exposure to a propane flame.

Although the signals were shown to match well going from either temperature to heat flux or from heat flux to temperature, the electrical noise inherent in the signals was

63

reduced when converting from heat flux to temperature, but was amplified when the conversion was from temperature to heat flux. The difference in integration of the signals versus differentiation was clear, even when the actual signal processing did not directly involve these operations.

These results are useful for understanding the relationships between heat flux and temperature measurements. It was shown that the time-resolved heat flux is a good signal for predicting temperature. Therefore, it may be useful in temperature control systems, such as a feed-forward temperature controller.

7.2   Recommendations

The following recommendations are suggested for future work in the study of the Heat Flux Microsensor for use as a temperature regulator:

1.   Determine a more consistent method of convection calibration for calculating the sensitivity of the Heat Flux Microsensor. By developing a better procedure for calibrating the sensor, the reliability of the sensitivity used in experimentation would be enhanced.

2.   Develop numerical procedures using the same methods presented for a a one-dimensional finite thickness substrate. This would help improve the capability of the Heat Flux Microsensor in predicting surface temperature from the heat flux signal over a longer time span.

3.   Develop a simple but accurate method for measuring substrate thermal properties.

List of References

1. Jones, T.V., and Schultz, D.L., "Heat Transfer Measurements in Short Duration Hypersonic Facilities," AGARDograph 165, 1973.

2. O'Brien, J.E., "A Technique for Measurement of Instantaneous Heat Transfer in Steady-Flow Ambient-Temperature Facilities," Experimental Thermal and Fluid Science, Vol. 3, 1990a, pp. 416-430.

3. O'Brien, J.E., "Effects of Wake Passing on Stagnation Region Heat Transfer," ASME Journal of Turbomachinery, Vol. 112, 1990b, pp.522-530.

4. Ching, C.Y., and O'Brien, J.E., "Unsteady Heat Flux in a Cylinder Stagnation Region with High Freestream Turbulence," in Fundamental Experimental Measurements in Heat Transfer, Eds. D.E. Beasley and J.L.S. Chen, ASME, New York, 1991, pp. 57-66.

5. Dunn, M.G., "Phase and Time-Resolved Measurements of Unsteady Heat Transfer and Pressure in a Full-Stage Rotating Turbine," ASME Journal of Turbomachinery, Vol. 112, 1990, pp. 531-538.

6. Jones, T.V., "Heat Transfer, Skin Friction, Total Temperature, and Concentration Measurements," in Measurements of Unsteady Fluid Dynamic Phenomena, Ed. B.E. Richards, Hemisphere Publishing Corporation, Washington DC, 1977, pp. 63-102.

7. Nicholson, J.H., Forest, A.E., Oldfield, M.L.G., and Schultz, D.L., "Heat Transfer Optimized Turbine Rotor Blades - An Experimental Study Using Transient Techniques," ASME Journal of Engineering for Gas Turbines and Power, Vol. 106, 1987, pp. 173-182.

8. Johnson, A.B., Rigby, M.J., Oldfield, M.L.G., Ainsworth, R.W., and Oliver, M.J., "Surface Heat Transfer Fluctuations on a Turbine Rotor Blade Due to Upstream Shock Wave Passing," ASME Journal of Turbomachinery, Vol. 111, 1989, pp. 105-115.

9. Diller, T.E., "Heat and Mass Transfer Measurements in Unsteady Flow," in Forum on Unsteady Flows in Biological Systems, Eds. M.H. Friedman and D.C. Wiggert, ASME, 1985, pp. 71-74.

10. Diller, T.E., "Time-Resolved Heat Transfer Measurements in Unsteady Flow," AIAA Paper Number 88-3599-CP, 1988, pp. 1471-1478.

11. Swisher, S.E., "Time-Resolved Heat Flux Measurements of the Turbulent Junction Vortex System," M.S. Thesis, Virginia Polytechnic Institute and State University, 1991.

12. Campbell, D.S., Gundappa, M., and Diller, T.E., "Design and Calibration of a Local Heat Flux Measurement System for Unsteady Flows," Fundamentals of Forced and Mixed Convection, Eds. F.A. Kulacki and R.D. Boyd, ASME, 1985, pp. 73-80.

13. Doorly, D.J., and Oldfield, M.L.G., "Simulation of the Effects of Shock Wave Passing on a Turbine Rotor Blade," ASME Journal of Engineering for Gas Turbines and Power, Vol. 107, 1985, pp. 998-1006.

14. Guenette, G.R., Epstein, A.H., Giles, M.B., Haimes, R., and Norton, R.J.G., "Fully Scaled Transonic Turbine Rotor Heat Transfer Measurements," ASME Journal of Turbomachinery, Vol. 111, 1989, pp. 1-7.

15. Miller, C.G., "Refinement of an 'Alternate' Method for Measuring Heating Rates in Hypersonic Wind Tunnels," AIAA Journal, Vol. 23, 1985, pp. 810-812.

16. Dunn, M.G., "Time-Resolved Heat-Flux Measurements for the Rotor Blade of a TFE-731-2 HP Turbine," in Convective Heat Transfer and Film Cooling in Turbomachinery, von Karman Institute for Fluid Dynamics, Rhode Saint Genese, 1986.

17. George, W.K., Rae, W.J., and Woodward, Scott H., "An Evaluation of Analog and Numerical Techniques for Unsteady Heat Transfer Measurement With Thin Film Gauges in Transient Facilities," Experimental Thermal and Fluid Science, Vol. 4, 1991, pp. 333-342.

18. Hager, J.M., Onishi, S., Langley, L.W., and Diller, T.E., "Heat Flux Microsensors," in Heat Transfer Measurements, Analysis and Flow Visualization, Ed. R.K. Shah, ASME, 1989, pp. 1-8.

19. Hager, J.M., Onishi, S., Langley, L.W., and Diller, T.E., "High Temperature Heat Flux Measurements," AIAA Paper Number 91-0165, 1991.

20. Hager, J.M., Terrell, J.P., Langley, L.W., Onishi, S., and Diller, T.E., "Measurements with the Heat Flux Microsensor," accepted for the 37th International Instrumentation Symposium of the Instrument Society of America, San Diego, May 1991.

21. Hager, J.M., Simmons, S., Smith, D., Onishi, S., Langley, L.W., and Diller, T.E., "Experimental Performance of a Heat Flux Microsensor," ASME Journal of Engineering for Gas Turbines and Power, Vol. 113, 1991a, pp. 246-250.

22. Mancuso, T., and Diller, T.E., "Time-Resolved Heat Flux Measurements in Unsteady Flow," in Fundamental Experimental Measurements in Heat Transfer, Eds. D.E. Beasley and J.L.S. Chen, ASME, New York, 1991, pp. 67-74.

23. Michener, M., Hager, J.M., Terrell, J.P., Veit, H., and Diller, T.E., "Noninvasive Blood Perfusion Measurement with a Heat Flux Microsensor," accepted for the 1991 Winter Annual Meeting of ASME, Atlanta, Dec. 1-6, 1991.

24. Incropera, F.P. and DeWitt, D.P., Introduction to Heat Transfer, Second Edition, John Wiley & Sons, New York, 1990, pp. 225-310.

25. Beck, J.V., Blackwell, B., and St. Clair, C.R., Jr., Inverse Heat Conduction, Ill Posed Problems, Wiley-Interscience, New York, 1985.

26. Diller, T.E., "Advances in Heat Transfer Measurement," accepted for Advances in Heat Transfer, Vol. 23, 1993.

27. Cook, W.J., and Felderman, E.M., "Reduction of Data From Thin-Film Heat-Transfer Gages: A Concise Numerical Technique," AIAA Journal, Vol. 4, 1966, pp. 561-562.

28. Cook, W.J., "Determination of Heat Transfer Rates from Transient Surface Temperature Measurements," AIAA Journal, Vol. 8, 1970, pp. 1366-1368.

29. Vidal, R.J., "Model Instrumentation Techniques for Heat Transfer and Force Measurements in a Hypersonic Shock Tunnel," Cornell Aeronautical Laboratory Report M. AD-917-A-1, 1956.

30. Eckert, E.R.G., and Drake, R.M. Jr., <u>Analysis of Heat and Mass Transfer</u>, McGraw Hill, New York, 1972, pp. 281-352.

31. Myers, G.E., <u>Analytical Methods in Conduction Heat Transfer</u>, McGraw-Hill, Inc., 1971, pp. 151-166.

32. Beck, J.V., "Green's Function Solution for Transient Heat Conduction Problems," <u>International Journal of Heat and Mass Transfer</u>, Vol. 27, 1984, pp. 1235-1244.

33. Beck, J.V., and Keltner, N.R., "Green's Function Partitioning Procedure Applied to Foil Heat Flux Gages," <u>ASME Journal of Heat Transfer</u>, Vol. 109, 1987, pp. 274-280.

34. Ozisik, M.N., <u>Heat Conduction</u>, John Wiley & Sons, New York, 1980, pp. 209-245.

35. Kidd, C.T., "Determination of the Uncertainty of Experimental Heat-Flux Calibrations," AEDC report TR-83-13, August 1983.

36. Simmons, S.G., Hager, J.M., and Diller, T.E., "Simultaneous Measurements of Time-Resolved Surface Heat Flux and Freestream Turbulence at a Stagnation Point," in <u>Heat Transfer 1990</u>, Vol. 2, Ed. G. Hetsroni, Hemisphere Publishing Corporation, New York, 1990, pp. 375-380.

37. Swisher, S.E., Diller, T.E., and Pierce, F.J., "Time-Resolved Heat Flux Measurements in a Turbulent Junction Vortex," in <u>Topics in Heat Transfer</u>, Vol. 1, Eds. M. Keyhani et al., ASME, New York, 1992, pp. 55-63.

38. Borell, G.J., and Diller, T.E., "A Convection Calibration Method for Local Heat Flux Gages," <u>Journal of Heat Transfer</u>, Vol. 109, 1987, pp. 83-89.

39. Diller, T.E., "Heat Transfer in Unsteady Flow," in <u>Proceedings of the International Conference on Fluid Mechanics</u>, Ed. S. Yuan, Peking University Press, Beijing, 1987, pp. 1217-1222.

40. Gundappa, M., and Diller, T.E., "Unsteady Heat Transfer Measurements Around a Cylinder in Pulsating Crossflow," in <u>1987 ASME/JSME Thermal Engineering Joint Conference</u>, Eds. P.J. Marto and I. Tanasawa, ASME, New York, 1987, pp. 629-634.

Appendix A

Heat Flux Microsensor Calibration

To determine the sensitivity of the Heat Flux Microsensor, convection calibration tests were performed. Tests were run in a boundary layer tunnel and in an unheated free jet. Three gages were used: the Gardon gage, the Schmidt-Boelter gage, and the Heat Flux Microsensor. Two different Heat Flux Microsensors were tested. One Heat Flux Microsensor was calibrated in both the boundary layer tunnel and the free jet. The Heat Flux Microsensor used in the current study was only calibrated in the free jet. The free jet configuration had a higher heat transfer coefficient than the boundary layer tunnel and its procedure was similar to the actual test situation.

A.1   Boundary Layer Tunnel Calibration

Each gage was mounted in a 3.49 cm (1.38 in.) diameter aluminum cylinder and placed inside a 13.18 cm x 11.59 cm (5.19 in. x 4.75 in.) wooden block. The wooden block was used to support the cylinder in a thin-walled aluminum block with a 15.24 cm x 15.875 cm (6.00 in. x 6.25 in.) face and an open back. The aluminum block was

mounted onto a 5.08 cm x 60.96 cm (2.00 in. x 24.00 in.) stainless steel strip. The strip was used to position the block in the center of the boundary layer tunnel at the leading edge of a plate in the tunnel floor where an slot opening was created to suction out the boundary layer. At this position, the gage was subjected to a uniform air flow.

Silicon wire resistance heaters were wrapped around the cylinder holding the gage and secured with electrical ties. A grounding cable was placed on top of the heaters and aluminum foil was wrapped around the gage. The aluminum foil was used to reduce the amount of electrical noise present in the signal. Electrical tape was wrapped over the aluminum foil to hold it firmly in place.

The cylinder was positioned in the wooden block using wood shims so that the surface of the gage was flush with the outer front surface of the aluminum block. The spacing between the sensor and the face of the aluminum block was filled with putty. With the gage in place, the entire apparatus was carefully positioned inside the tunnel and secured using four C-clamps located at equal distances from the center of the block.

The leads from the gage were connected to an amplifier box built by Vatell Corporation. The output from the amplifier was monitored with the HP signal analyzer. The heater wires were hooked up to a Variac power supply. The thermocouples in the probe holder were connected to a Doric Trendicator Model 410A thermocouple readout meter. A pitot static probe was inserted upstream to measure the tunnel air speed. The estimated air velocity was 31.9 m/s.

After the temperature and heat flux signals were zeroed, the gage was heated to

approximately 45 °C prior to turning on the tunnel. With the tunnel providing a uniform air flow field, the gage temperature was allowed to reach thermal equilibrium. At steady state data was taken for a particular power setting on the Variac. The gage and air temperatures were recorded for the specified Variac setting. Then, the Variac setting was increased. When thermal equilibrium occurred for this Variac setting, another measurement was taken. This procedure was repeated for several Variac settings between 40 W and 100 W.

Using the Gardon gage as a standard, the heat transfer coefficient was calculated for the air blowing through the boundary layer tunnel. From [38], the sensitivity of the Gardon gage was $S = 2.41 \times 10^{-5}$ mV/(W/cm^2). The indicated heat transfer coefficient is given by

$$h_i = \frac{\dfrac{E_q}{S} - \varepsilon_g \sigma(T_p^4 - T_\infty^4)}{T_p - T_a} \tag{30}$$

where $\epsilon_g = 0.97$ and σ, the Stefan-Boltzmann Constant, is 5.67×10^{-8} W/(m^{2}K^4). The corrected value for the heat transfer coefficient is given by

$$h_c = \left[\frac{1}{1 - \dfrac{.75\,S\,h_i}{K_2}} \right] h_i \tag{31}$$

where $K_2 = 0.042$ mV/°C. Figure 23 illustrates the values of the heat transfer coefficient, h_c, versus the change in temperature, $(T_g - T_a)$ for the Gardon gage. The average heat transfer coefficient was $h = 52.8 \pm 2.5$ W/(m^2°C) for a 95% confidence
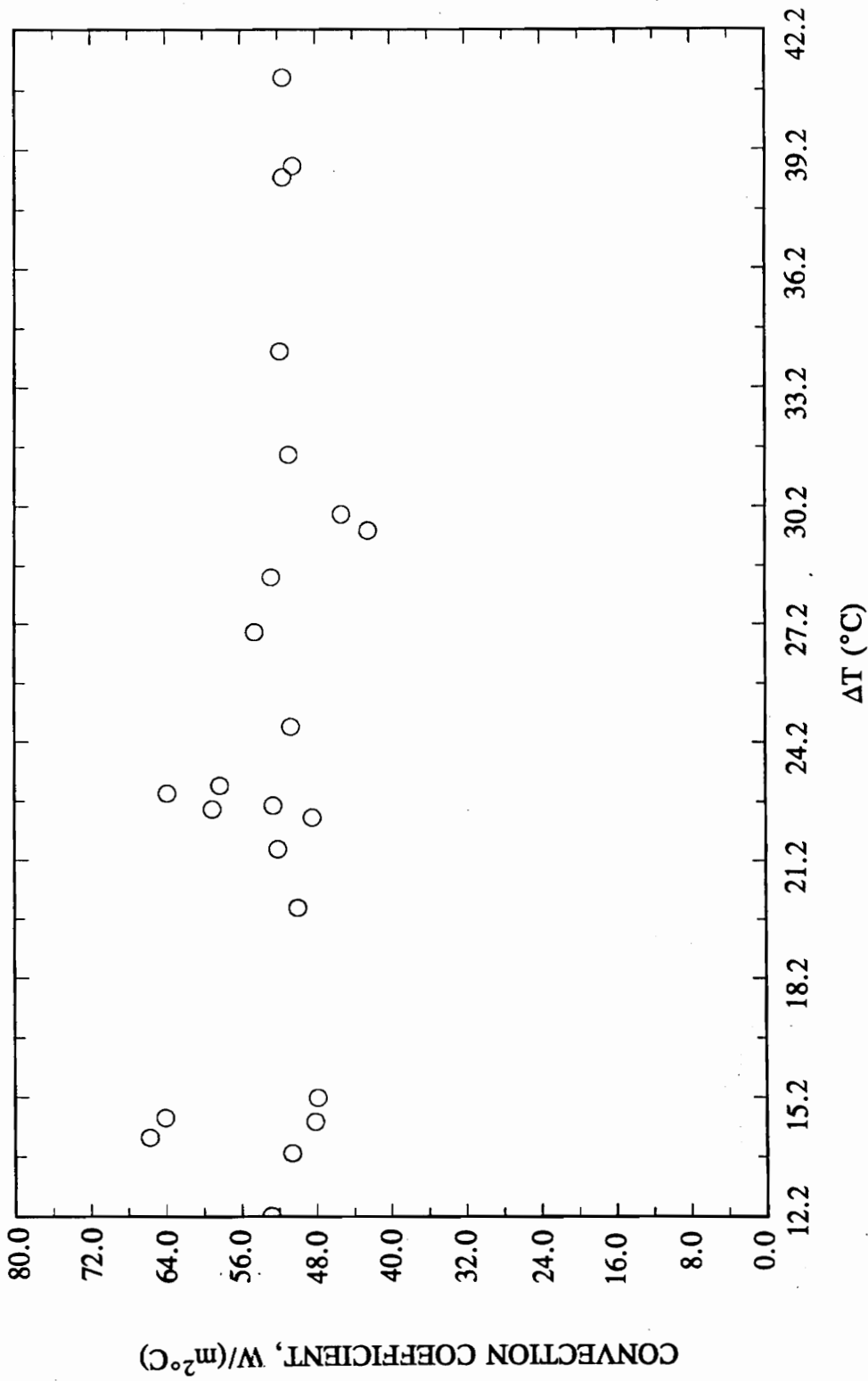
Figure 23. Convection Calibration for Gardon Gage in Boundary Layer Tunnel

interval. The standard deviation was 5.89 W/(m²°C).

After the heat transfer coefficient for the air flowing through the boundary layer tunnel was determined, the other two gages were calibrated to determine the sensitivity of each gage. Figure 24 shows the output for the Schmidt-Boelter (SB) gage versus heat flux. The heat flux, q, was calculated using the measured surface and air temperatures and the heat transfer coefficient determined by the Gardon gage

$$q = h(T_s - T_a) + q_{rad} \tag{32}$$

where q_{rad} is given by

$$q_{rad} = \varepsilon_g \sigma (T_s^4 - T_a^4) \tag{33}$$

The sensitivity, defined by

$$S = \frac{E_q}{q} \tag{34}$$

is the slope of the calibration curve in Fig. 24. The sensitivity for each data point was calculated and graphed versus gage temperature. Figure 25 illustrates the results. From Fig. 25, the sensitivity of the Schmidt-Boelter gage was estimated as $S = 3.66$ mV/(W/cm²).

The same procedure was performed for the Heat Flux Microsensor. The calibration curve illustrated in Fig. 26 shows the output from the Heat Flux Microsensor versus heat flux, q, as defined in Eq. 32. For the Heat Flux Microsensor, the heat flux was calculated with and without radiation. When radiation was considered, the
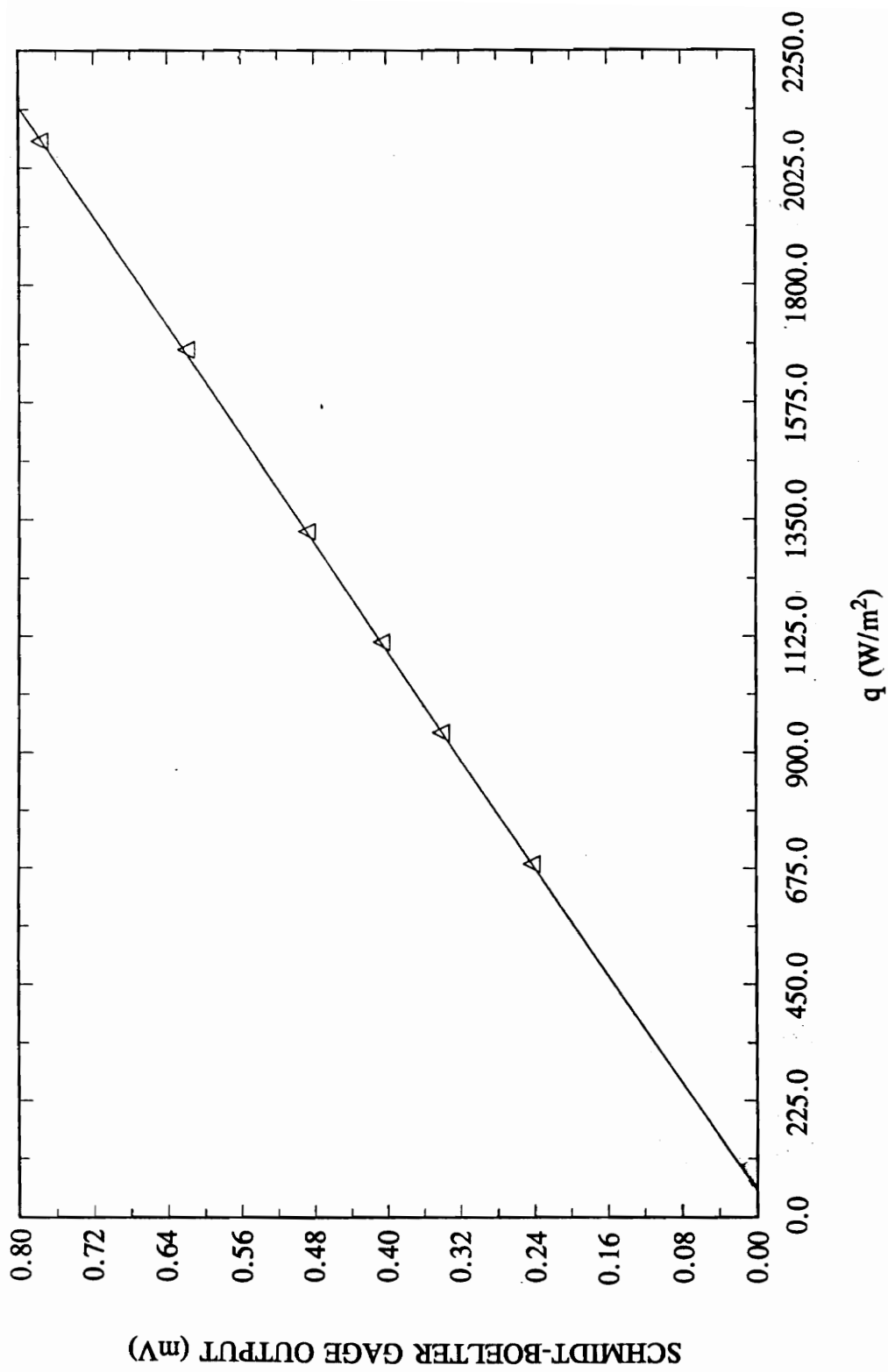
Figure 24. Boundary Layer Tunnel: Schmidt-Boelter Gage Output Versus Heat Flux

75
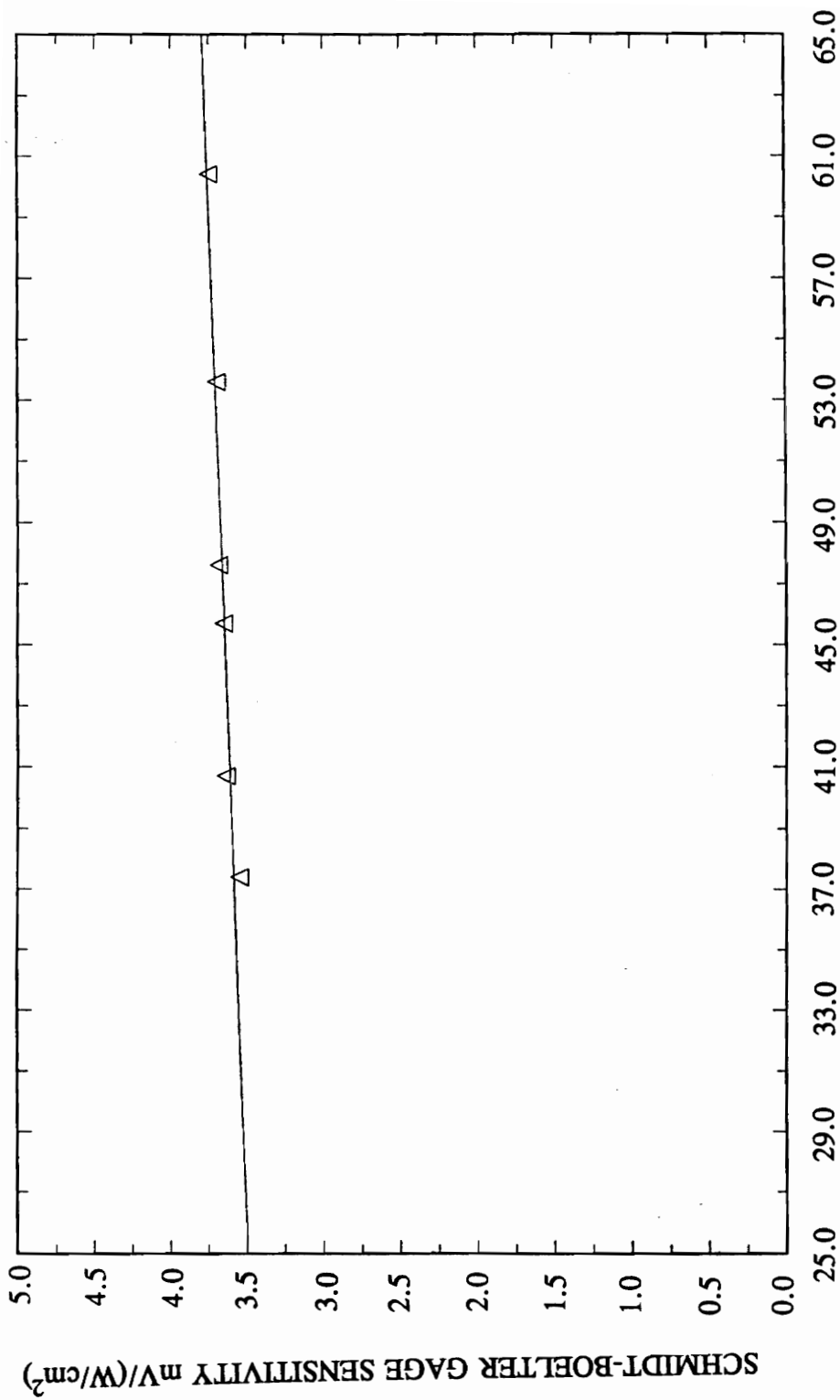
SCHMIDT-BOELTER GAGE TEMPERATURE (°C)

Figure 25. Boundary Layer Tunnel: Schmidt-Boelter Gage Sensitivity Versus Gage Temperature
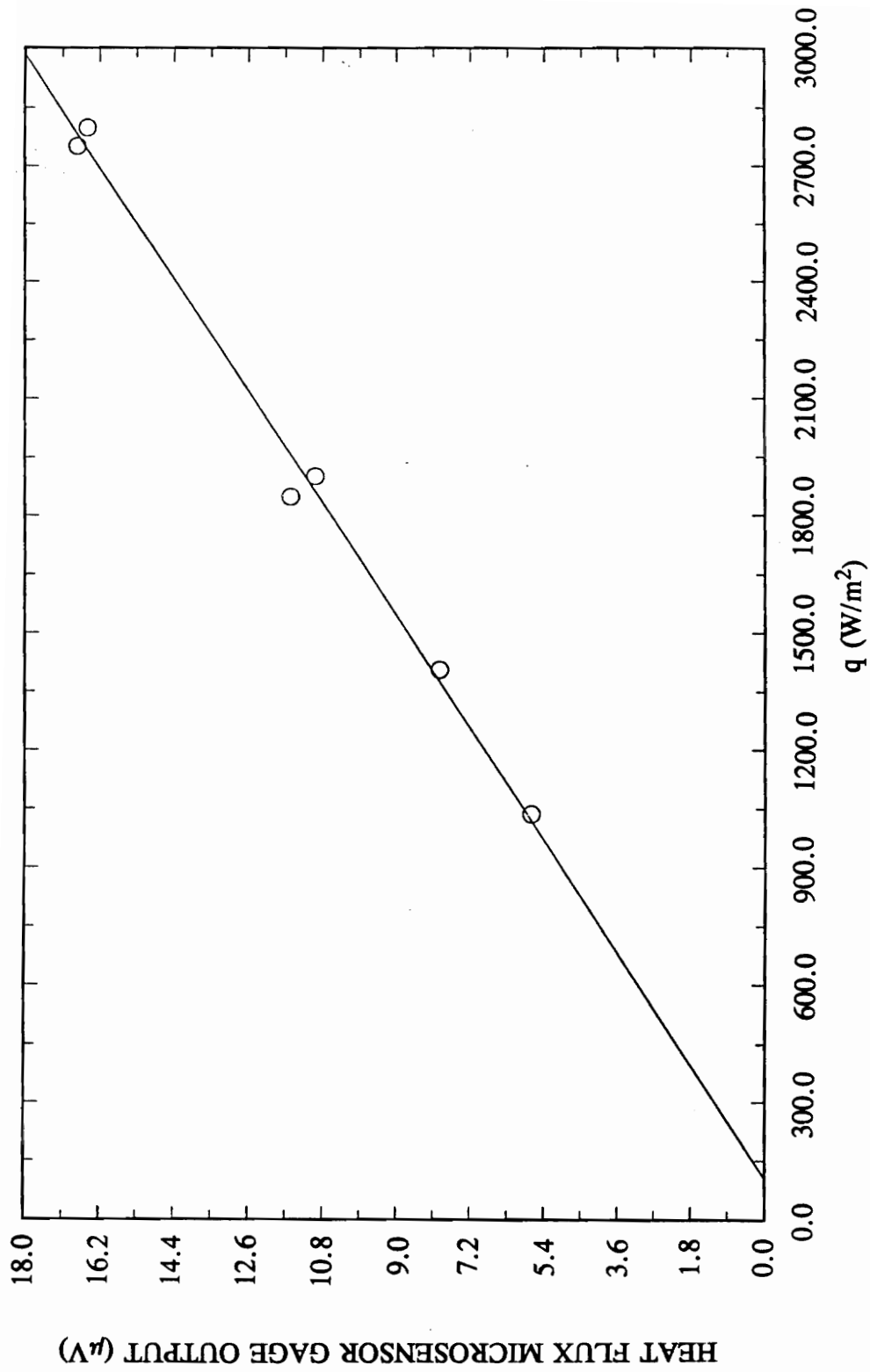
Figure 26. Boundary Layer Tunnel: Heat Flux Microsensor Output Versus Heat Flux

HEAT FLUX MICROSENSOR GAGE OUTPUT (μV)

q (W/m^2)

emissivity was taken as $\epsilon_g = 0.69$. A sensitivity versus gage temperature plot for the sensor is shown in Fig. 27. The sensitivity of the Heat Flux Microsensor was estimated as $S = 58.65 \, \mu V/(W/cm^2)$ considering the radiation effects and $S = 64.17 \, \mu V/(W/cm^2)$ neglecting radiation.

A.2   Jet Calibration

The above three gages were then tested in an unheated free jet. Each gage was prepared as detailed above and placed in the aluminum block. The stainless steel strip was not used since the block did not need to be clamped onto a plate. The configuration for the jet is shown in Fig. 28. The jet was created by a 3.81 cm (1.50 in.) diameter orifice. The block was positioned three jet diameters, 11.43 cm (4.50 in.), away from the jet.

The leads were connected to a Dynamics Differential DC Model 7526A amplifier which was then connected to the HP dynamic signal analyzer. The heaters were connected to a Variac and each gage's internal thermocouple was connected to a Doric Trendicator Model 410A thermocouple readout meter. A thermocouple was positioned upstream to monitor the temperature of the free stream air. A U-tube manometer was used to measure the static pressure.

After the gage was heated to approximately 45 °C, the jet was turned on. When the surface temperature reached thermal equilibrium for a particular Variac setting, a data

78
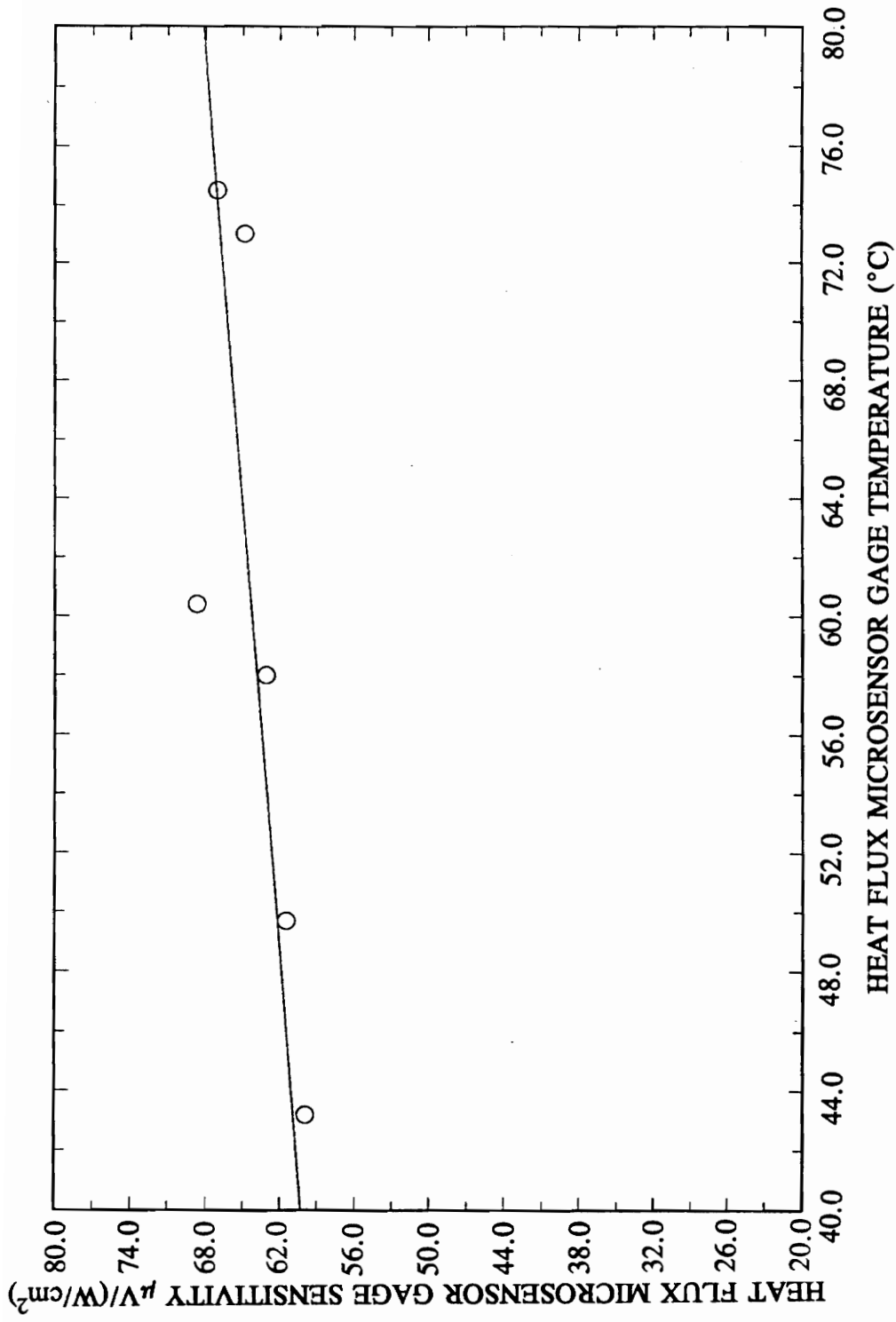
Figure 27. Boundary Layer Tunnel: Heat Flux Microsensor Gage Sensitivity Versus Gage Temperature

Air Jet

Heat Flux Gage
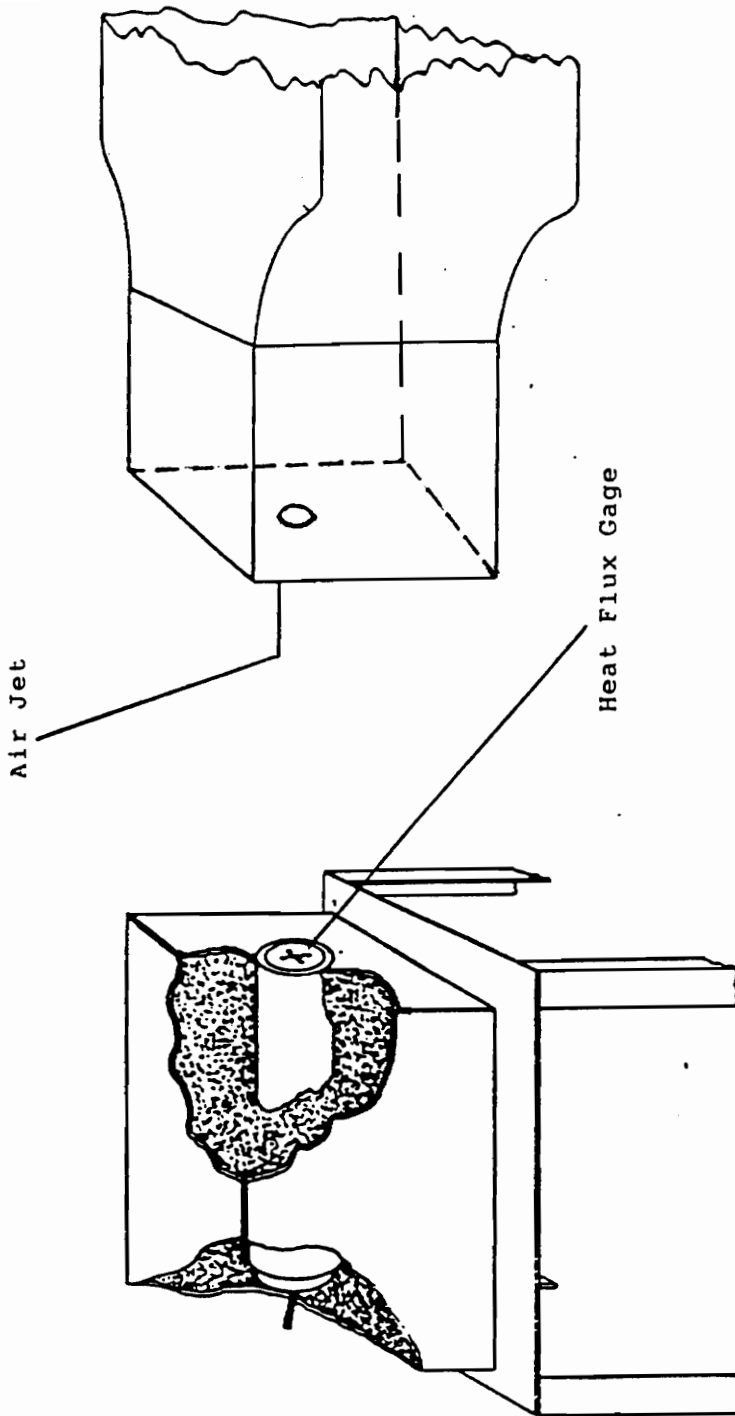
Figure 28. Schematic of Jet Calibration Tunnel

measurement was taken. Several measurements were taken over a range of Variac settings. When each gage had been tested, it was removed from the aluminum block. After all the gages had been tested, each was placed back into the aluminum block and retested. This was done to determine repeatability of the calibration experiments.

Using a Gardon gage mounted at the stagnation point, the heat transfer coefficient was calculated for the air blowing out of the unheated free jet for several gage temperatures. Figure 29 graphically illustrates the results. The Δp measured for this type of calibration was 13 in. H_2O. The heat transfer coefficient was h = 205 $\pm$ 2.3 W/m^2K at 95% confidence with a standard deviation of 4.4 W/m^2K.

The Schmidt-Boelter gage was mounted in the same position as the Gardon gage. Again, tests were run over a range of gage temperatures. The gage's output versus heat flux is shown in Fig. 30. The two curves represent the first and second tests of the gage. There is a discrepancy in the curves because the gage was not positioned in exactly the same place for both tests. The sensitivity for each data point was calculated and plotted versus gage temperature in Fig. 31. The average sensitivity was S = 3.90 $\pm$ 0.2 mV/(W/cm^2). In determining the sensitivity, the data acquired from both tests were combined.

As with the first two gages, the Heat Flux Microsensor was mounted at the stagnation point. The gage was tested twice in the unheated free jet. Because the results for each test matched well, the data was combined. The output of the Heat Flux Microsensor versus heat flux is shown in Fig. 32. As illustrated, most of the data points
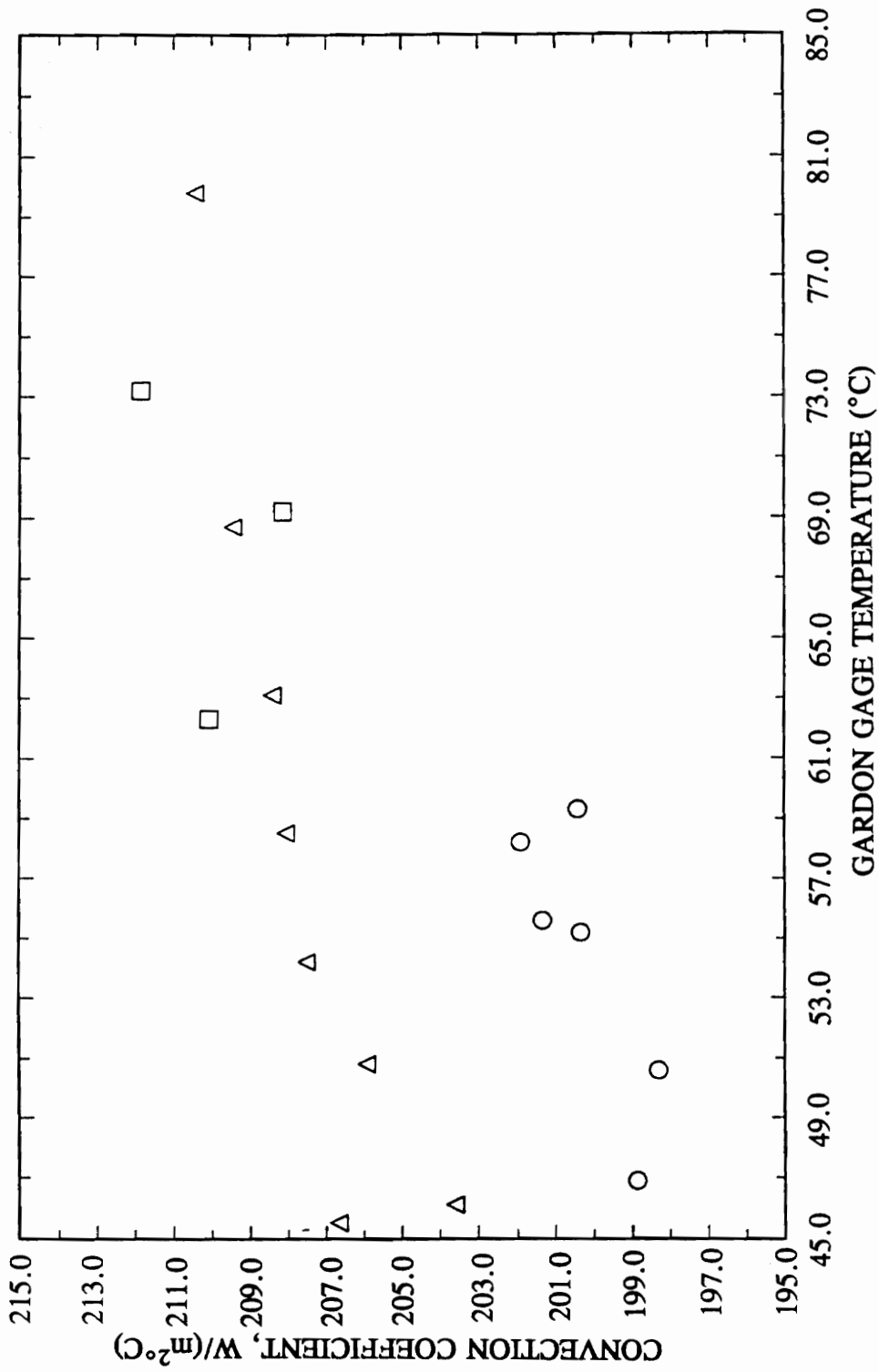
Figure 29. Convection Calibration for Gardon Gage in Free Jet
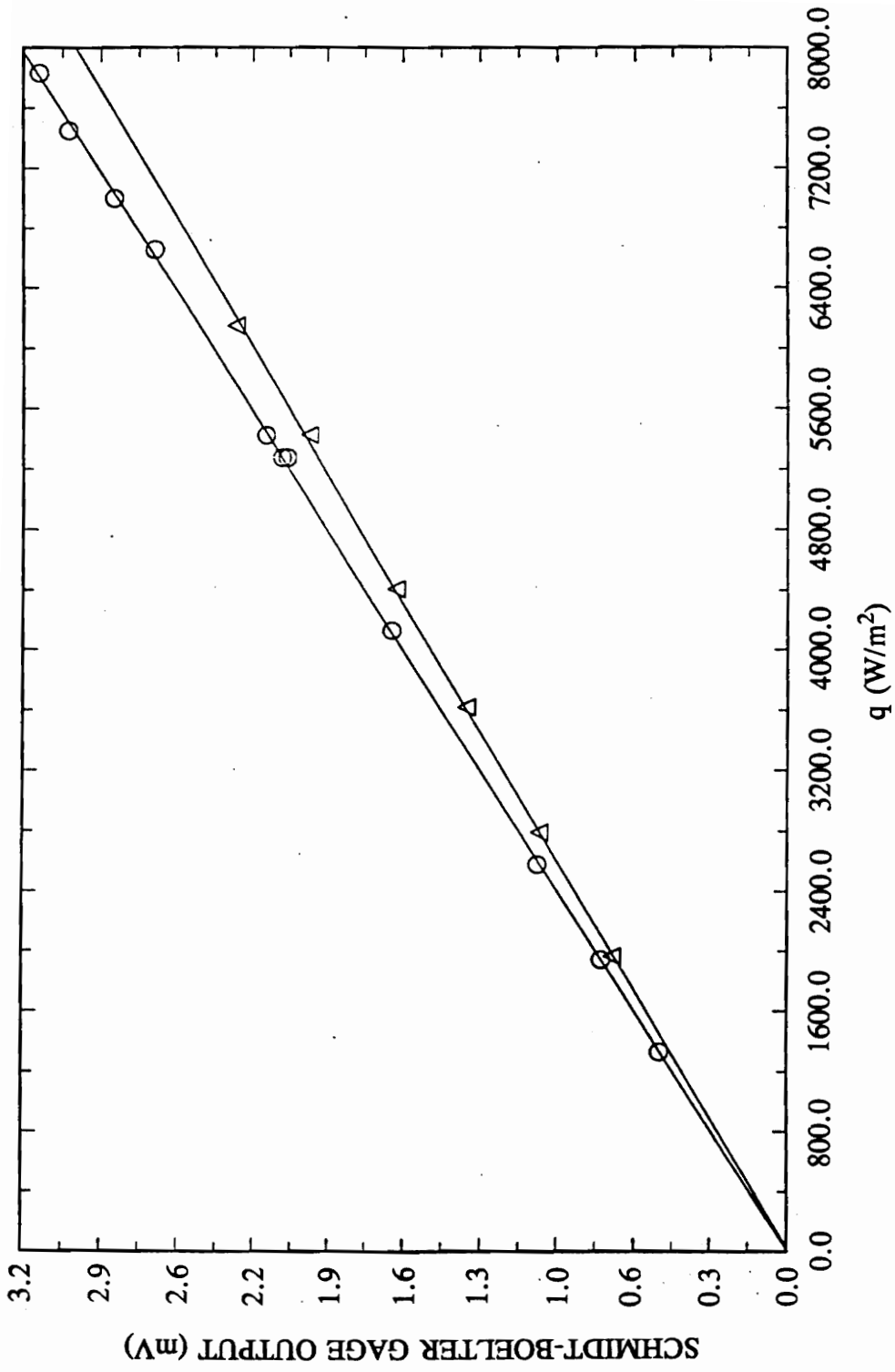
Figure 30. Free Jet: Schmidt-Boelter Gage Output Versus Heat Flux

83
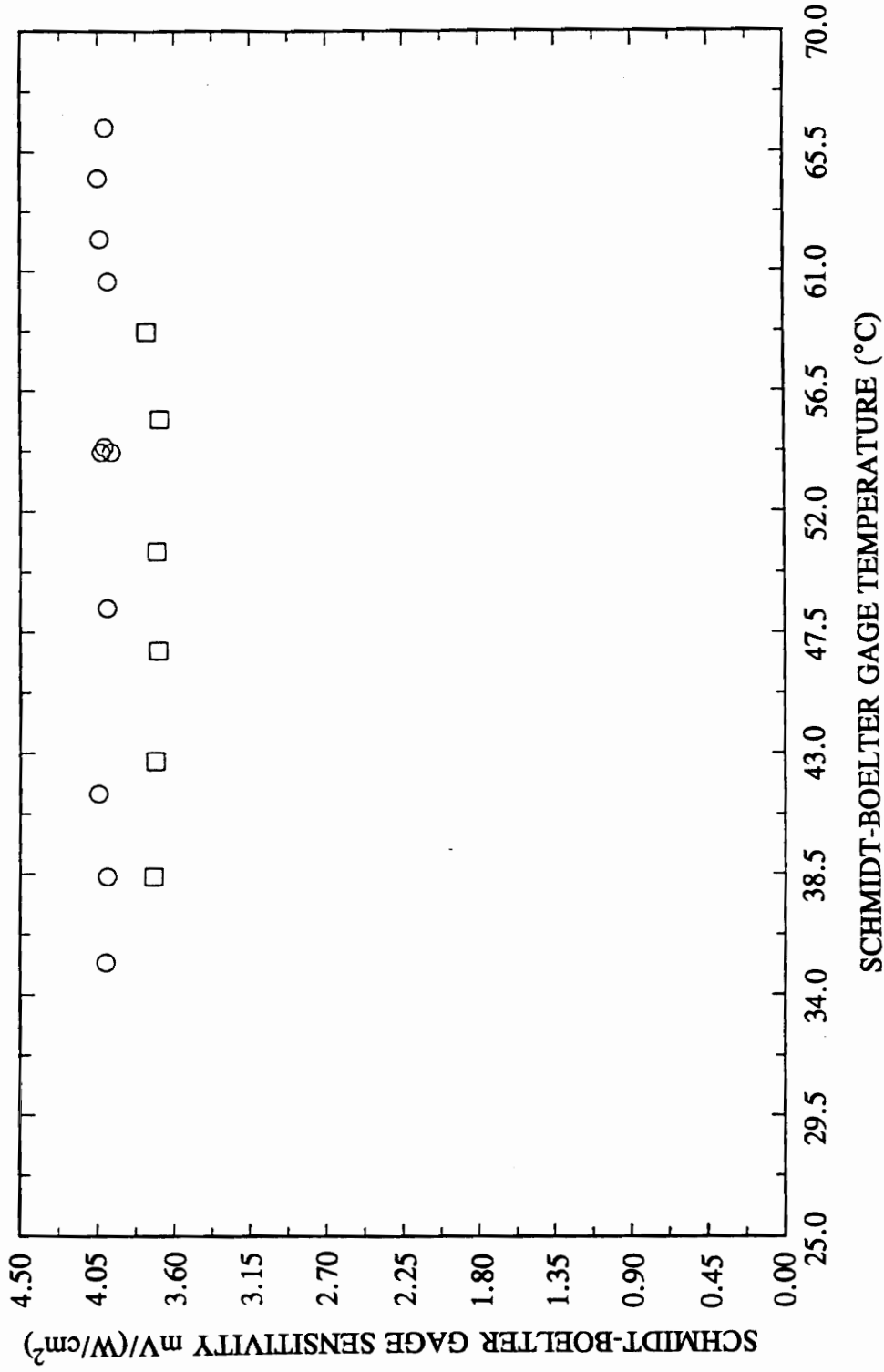
Figure 31. Free Jet: Schmidt-Boelter Gage Sensitivity Versus Gage Temperature

84
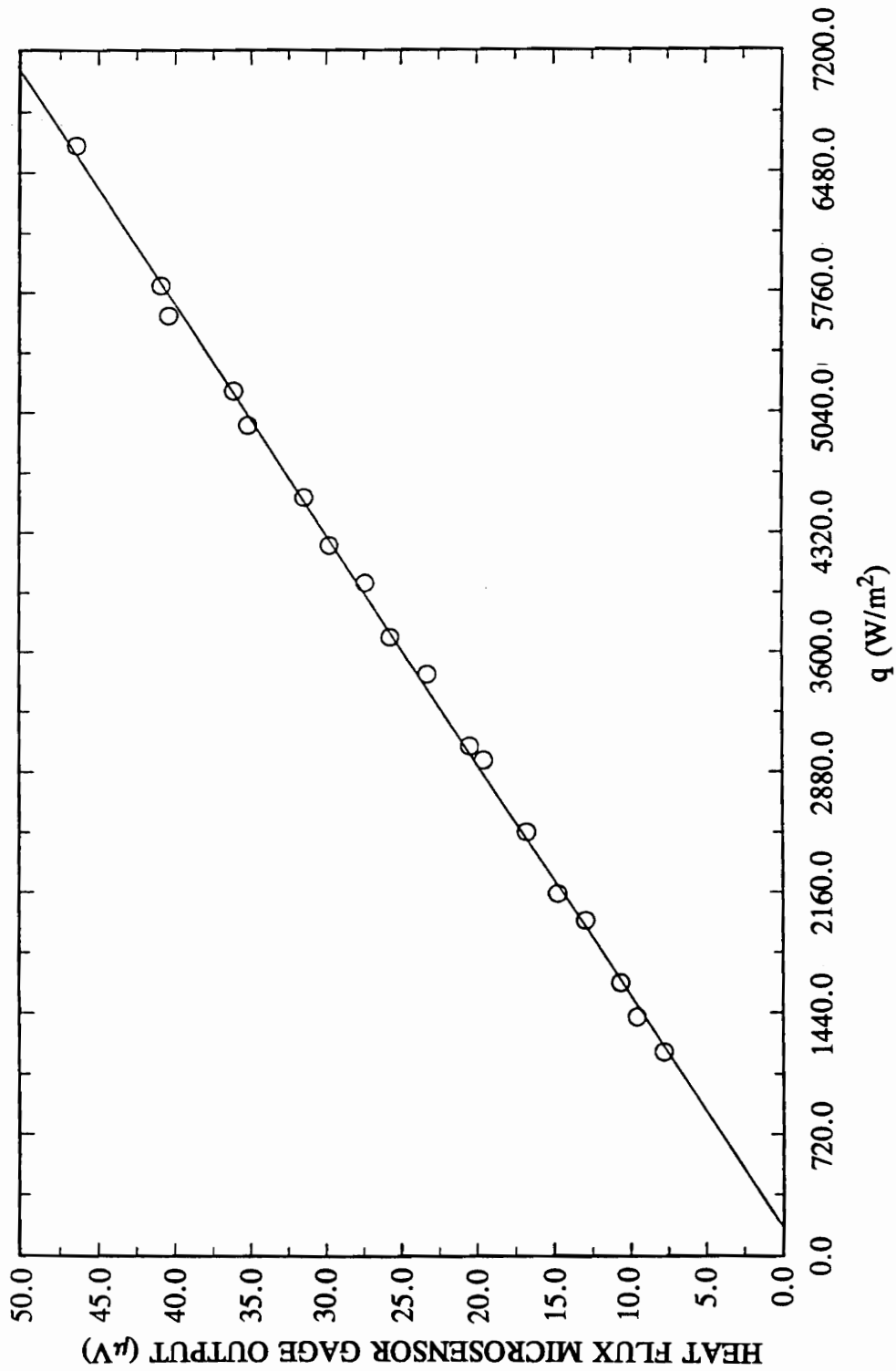
Figure 32. Free Jet: Heat Flux Microsensor Gage Output Versus Heat Flux

fall on or near the calibration curve. When plotting the sensitivity calculated at each data point versus gage temperature, Fig. 33 illustrates that the sensitivity increases slightly with increasing gage temperature. Otherwise the scatter is small. As in the boundary layer calibration procedure, the radiative effects were both considered and neglected. An emissivity of $\epsilon_g = 0.69$ was used when radiation was considered. The sensitivity of the Heat Flux Microsensor was $S = 66.69 \pm 1.1 \ \mu V/(W/cm^2)$ with radiation effects and $S = 68.23 \pm 1.0 \ \mu V/(W/cm^2)$ without radiation effects.

The Heat Flux Microsensor used in this study was calibrated in the unheated free jet configuration shown in Fig. 28. Calibration tests were performed with the sensor unpainted and with the sensor's surface painted with Krylon ultra-flat black spray. This paint has a reported absorptivity of 0.97 [35]. The experimental set-up was the same as above but the procedure was changed. For the current research, there was no steady state requirement. Thus, the calibration did not have to depend on whether thermal equilibrium was reached.

The amplifier for the current research was used instead of the Dynamics Differential DC Model 7526A amplifier. The gain on the Heat Flux Microsensor was set at 1000 and the gain for the RTS was set at 200. The heat flux signal was used as the input to Channel 1 and the RTS was used as the input to Channel 2 of the HP signal analyzer. The range on Channel 1 of the HP signal analyzer was set to 100 mV and the range for Channel 2 was set to 2V, peak-to-peak. The time length for each measurement was set for 25 sec.
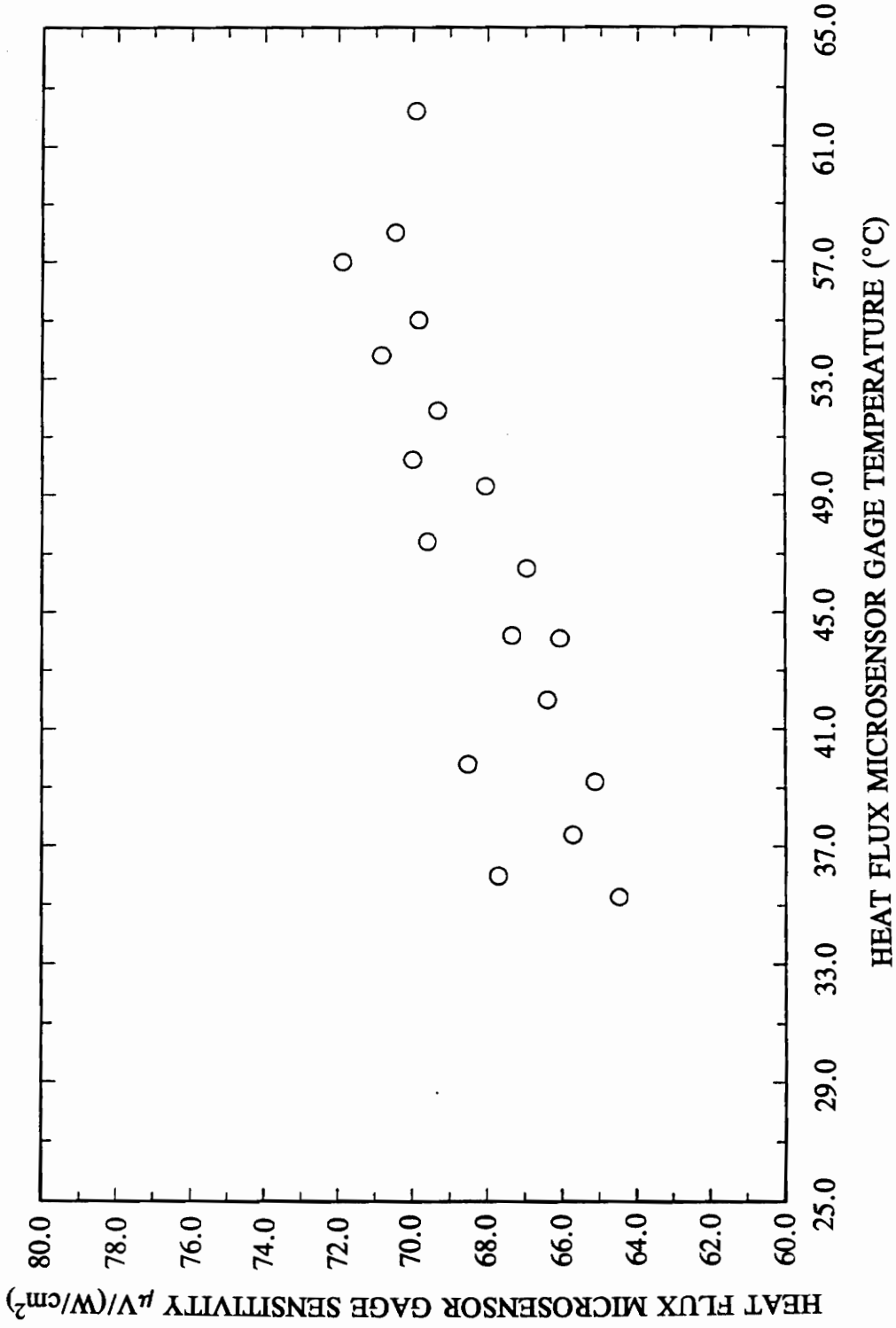
Figure 33. Free Jet: Heat Flux Microsensor Gage Sensitivity Versus Gage Temperature

Using the Variac at a setting of 70 W, the heaters were allowed to thoroughly heat the gage prior to running the calibration tests. The Variac setting was not changed during the calibration experiments. When the gage was heated, a 22.86 cm x 30.48 cm (9.00 in. x 12.00 in.) stainless steel plate was inserted between the jet and the sensor before turning on the jet. The heaters were turned off during the test to reduce the noise distortion during the data collection. After the jet was turned on, the plate was quickly removed to "trip" impingement of the air blowing out of the jet onto the sensor.

The temperature calibration curve discussed in Appendix B was used to determine the surface temperature. The ambient air temperature was 25 °C. The heat flux from the surface of the sensor was calculated using Eq. 32. Then, as in Eq. 34, the output voltage from the Heat Flux Microsensor was divided by the calculated heat flux to determine the sensitivity.

Samples of the time-resolved heat flux and surface temperature measurements for the unpainted sensor are shown in Fig. 34. The results are tabulated in Table 1. The average sensitivity for the Heat Flux Microsensor neglecting radiation was $S_q = 28.3$ $\mu V/(W/cm^2)$. With radiation taken into account, the sensitivity was $S_q = 27.6$ $\mu V/(W/cm^2)$. The sensitivity decreased because the denominator of Eq. 34 contained the added q_{rad} term from Eq. 32. Therefore, the denominator was larger since heat convected and radiated from the surface of the sensor flows in the same direction.

The calibration was also performed after the sensor was painted black. Samples of the time-resolved heat flux and surface temperature measurements for this case are
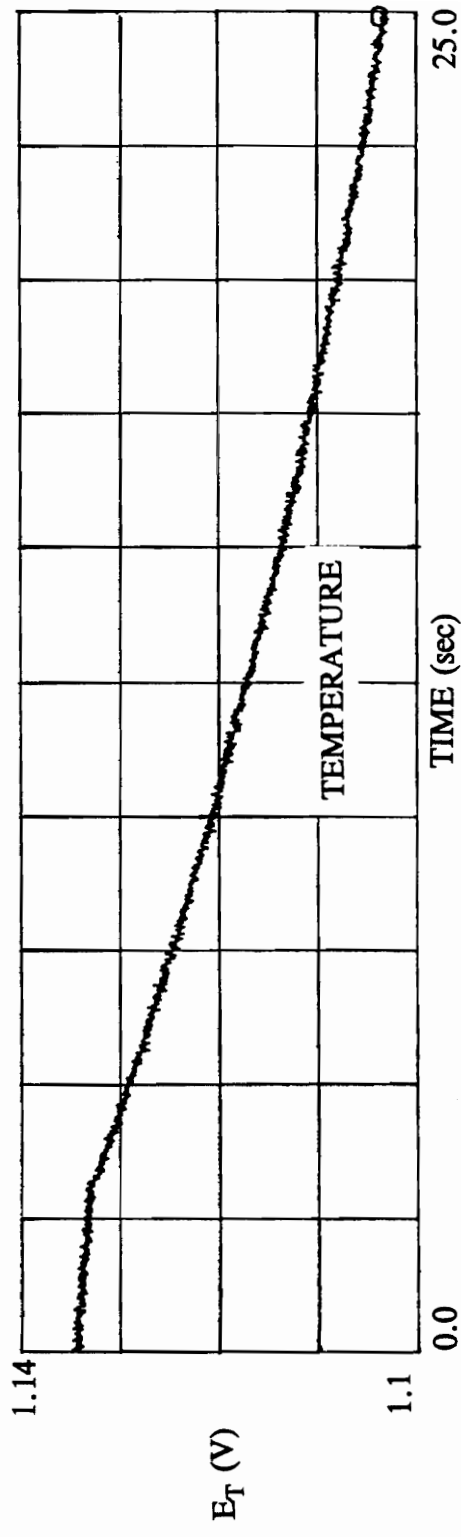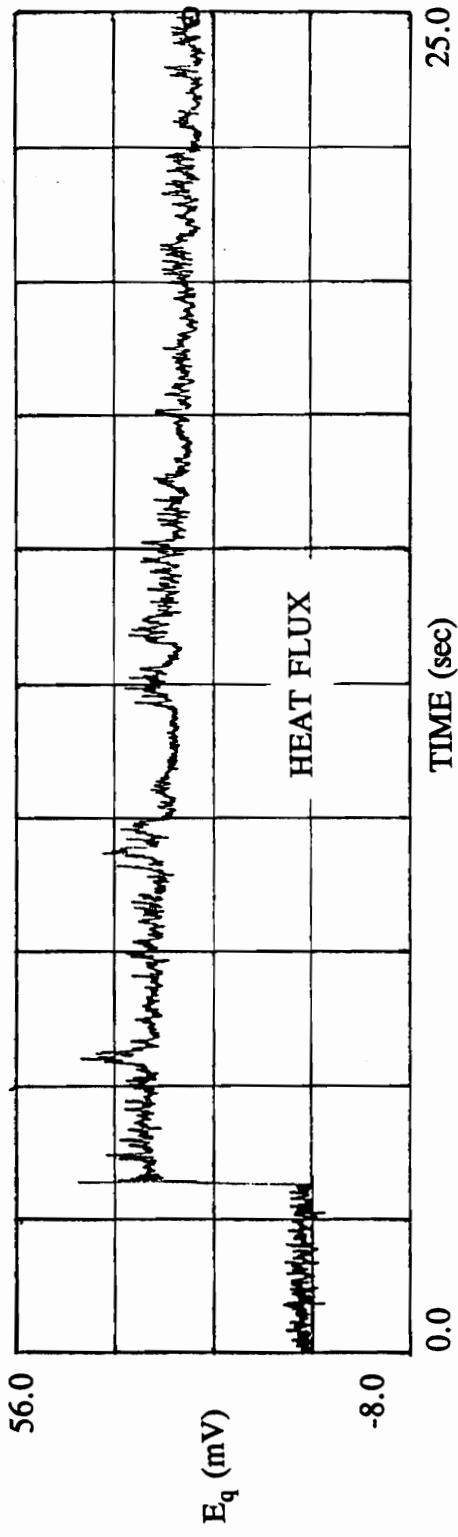
Figure 34. Time-Resolved Heat Flux and RTS Measurements for Unpainted Sensor

89

illustrated in Fig. 35. The results of the calibration tests are tabulated in Table 2. The sensitivity was again determined with and without radiation. The sensitivity was $S_q = 24.1\ \mu V/(W/cm^2)$ without radiation and $S_q = 23.2\ \mu V/(W/cm^2)$ with radiation. Because there was a reasonable difference when considering radiation, the radiation effects were considered. In addition, the sensitivities of the painted sensor were noticeably lower than those of the clear sensor. For the current study, the sensor was painted black. Therefore, the sensitivity of the painted sensor taking into account radiation effects was used.
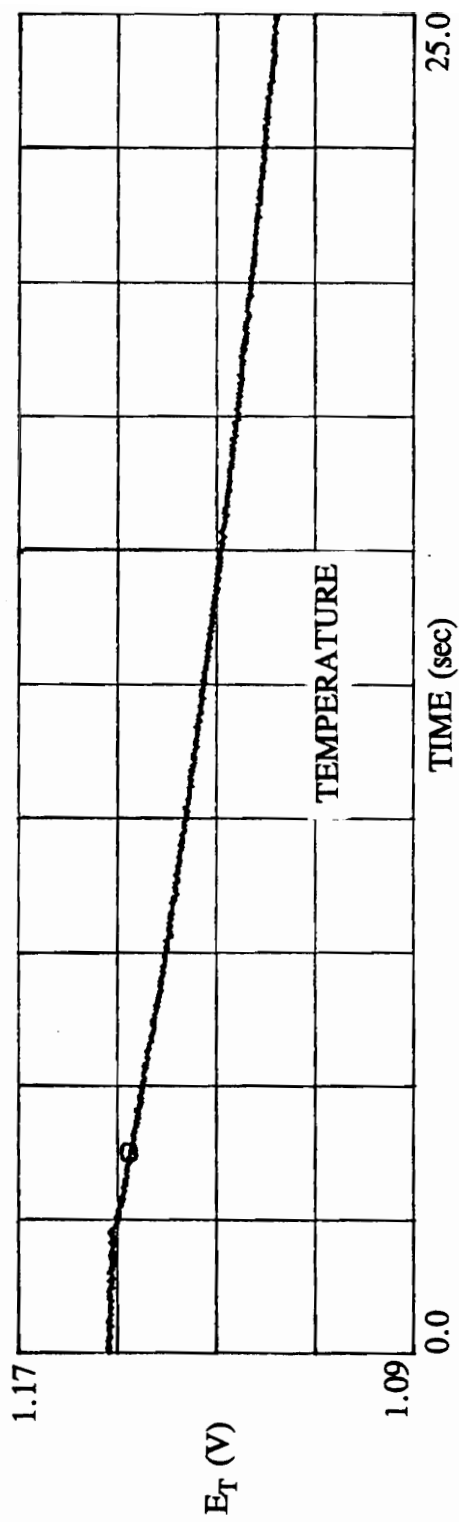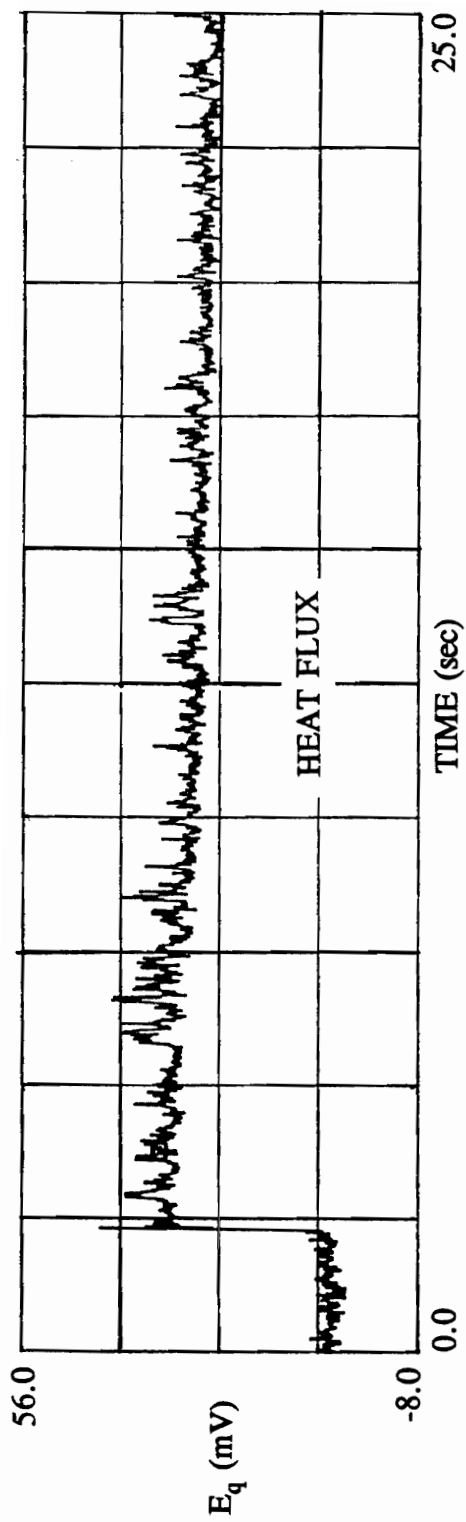
Figure 35. Time-Resolved Heat Flux and RTS Measurements for Painted Sensor

91

Table 1. Sensitivities for Unpainted Sensor

Run	Average S_q Without Radiation $\mu V/(W/cm^2)$	Average S_q With Radiation $\mu V/(W/cm^2)$
1	29.37	28.61
2	28.49	27.76
3	26.66	25.87
4	27.53	26.84
5	29.11	28.34
6	28.87	28.10
Overall Average S_q $\mu V/(W/cm^2)$	28.34	27.59

Table 2. Sensitivities for Painted Sensor

Run	Average S_q Without Radiation $\mu V/(W/cm^2)$	Average S_q With Radiation $\mu V/(W/cm^2)$
1	23.18	22.33
2	24.63	23.71
3	24.32	23.43
4	24.30	23.42
5	24.48	23.58
6	23.41	22.59
Overall Average S_q $\mu V/(W/cm^2)$	24.05	23.18

Appendix B

RTS Calibration

The RTS temperature sensor on the Heat Flux Microsensor was calibrated using a T-type thermocouple. The sensor and the thermocouple were placed in an isolated environment in direct thermal contact with each other. After the RTS sensor was zeroed at room temperature, a Variac was used to heat several silicone wire resistance heaters placed in the same isolated environment. At thermal equilibrium, the output of the RTS was recorded along with the thermocouple output over the temperature range of the current research using a multimeter and a Doric Trendicator, respectively. The measurements for the RTS were taken at a gain of 200 to be consistent with the current work's setting. The results are shown in Fig. 36 and indicate a linear relationship between RTS output voltage and temperature.

A linear regression was performed to obtain a calibration curve for the RTS sensor. The curve is

$$T = 330.83 \left[\frac{^\circ C}{V} \right] E_T - 291.06\,^\circ C \tag{35}$$

This calibration curve was used in the current work to calculate temperature from the voltage output of the sensor.
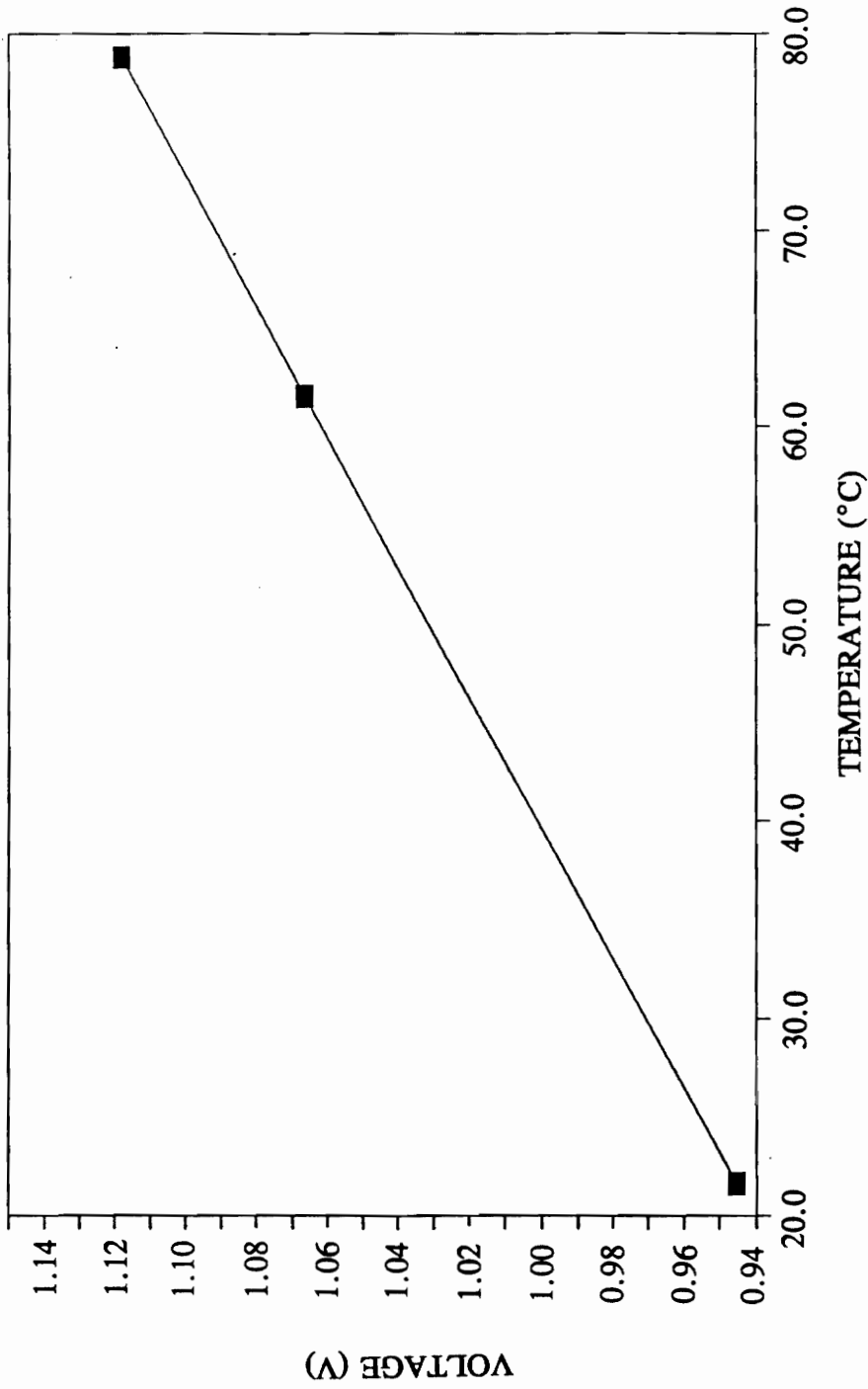
Figure 36. Calibration Curve for RTS Temperature Sensor

Appendix C

Heat Transfer in Steady and Pulsating Flow

Average and time-resolved measurements of heat flux were obtained over a flat plate in steady and pulsating flow. The unsteadiness effects on the surface heat flux were explored for pulsating free streams. The mean heat transfer over the stagnation and wake regions of the model were measured and compared with simultaneous time-resolved measurements of both the flow and heat flux.

C.1   Introduction

A constraint in the design of modern gas turbines is the limitation placed on the operating temperature of the blades. Several groups have explored how flow unsteadiness affects the amount of heat transferred to the blades [3,5,13,14]. From these experiments, it was determined that the unsteadiness of the flow further increases the amount of heat transferred to the blades beyond steady-state values. Because heat transfer in a stagnation region increases with the speed of the oncoming free stream, it was believed that the periodic increases of the stream between upstream blades would

explain the overall 10% to 15% increase over steady-state conditions. However, Doorly and Oldfield [13] determined that the heat transfer is higher in wake regions, where the free stream is interrupted by one blade prior to coming into contact with a second blade. In this instance, the velocity of the oncoming stream is much lower and the higher rate of heat transfer was considered a result of the locally turbulent character of the flow. To examine how the character of the flow affects heat transfer, a method of measuring instantaneous values of wall heat flux was required. Simultaneous measurements on the dynamics of the oncoming flow field were also needed to fully comprehend the effects. The Heat Flux Microsensor was used to measure the instantaneous values of wall heat flux and a hot-wire anemometer was used to monitor the flow of the free stream.

In order to understand the underlying mechanisms that influence temporal variation of heat transfer, simplified problems have been developed for various types of unsteadiness in the flow field as well as different configurations. Two specific configurations are flow over a circular cylinder and flow over a flat plate. First, time-resolved heat transfer was measured over a circular cylinder in steady flow [39]. This experiment determined that the heat transfer signal reacts to the unsteadiness of the wake region. This response drives the attached boundary layer into a periodic motion. This model was then extended to pulsating flows [40]. In pulsating flow, it was concluded that the reduced velocity and surface heat flux varied proportionally to each other. [36] investigated the effects of turbulence on stagnation heat transfer. A jet was aimed through a turbulence grid and then was impinged on a flat instrumented plate. It was

found that there were significant increases of heat transfer with increasing turbulence levels.

C.2   Experimental Procedure

Tests were conducted in a blow-down type of a wind tunnel with a test section having a length of 248 cm (97.64 in.) and a cross section of 74 cm x 53 cm (29.13 in. x 20.87 in.).   A set of rotating vanes is located in the settling chamber which can generate a pulsating stream in the test section. This chamber contains a honeycomb and six screens and leads to a 6:1 converge section. The turbulence level in the test section was approximately 0.4% to 0.5%. These values were not exceeded when the turning vanes were activated to produce pulsating flow. The waveforms of the pulsating velocity were nearly sinusoidal, with at least 95% of the wave energy in the fundamental frequency. In terms of the mean stream velocity U_∞ and the amplitude A, the velocity in the test section is given by

$$U = U_\infty (1 + A\sin(2\pi ft)) \qquad\qquad (36)$$

where f is the pulsation frequency and t is time. The amplitude A achieved in this manner was a function of the frequencies at which the tests were run.

The Heat Flux Microsensor was mounted in the center of a 23.18 cm x 7.62 cm

(9.13 in. x 3.00 in.) flat plate. Tests were run at pulsation frequencies of 2 Hz, 7 Hz, and 13 Hz in both stagnation and wake regions of the flow. A hot-wire anemometer was placed 0.3 widths upstream of the stagnation region of the flat plate to measure waveforms of the velocity signal. The sensor was heated to approximately 100 °C and the wind tunnel was turned on. The flow was adjusted to the desired frequency and data was taken.

The Heat Flux Microsensor was calibrated in convection heat transfer. The sensor was heated to 100 °C and an air jet was shuttered onto the face. Simultaneous measurements of the sensor voltage output, E_q, and surface temperature, T_s, were recorded and used to determine the heat flux sensitivity, $S_q = E_q/q$. The gage sensitivity was constant over the measurement range and was determined to be S = 7.36 $\mu V/(W/cm^2)$ with a standard deviation of 0.68 $\mu V/(W/cm^2)$.

C.3   Results and Discussion

At a free stream pulsation frequency of 13 Hz, heat flux and velocity measurements were recorded. Figure 37 illustrates the waveforms of these signals. The heat flux signal indicates evidence of the first harmonic which is due to the upstream influence of the wake oscillation. The same behavior has also been reported using skin friction gages. The expected shedding frequency at this mean free stream velocity was

99
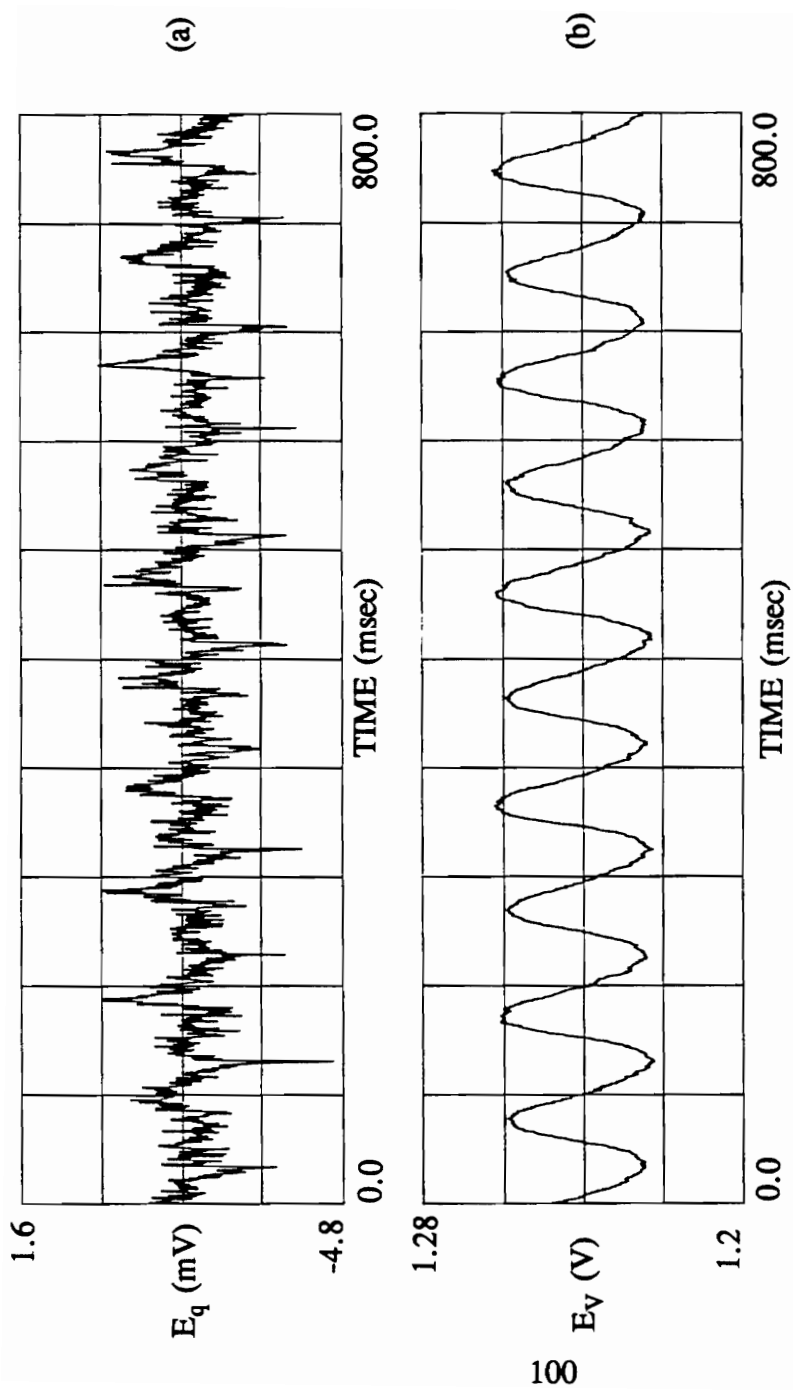
Figure 37. Waveforms of a) Heat Flux and b) Velocity for Stagnation Flow

at a Free Stream Pulsation Frequency of 13 Hz

100

14 Hz. Thus, the skin friction oscillation detected at the stagnation point is 28 Hz, almost twice the free stream pulsation. In Fig. 38, the coherence of the two signals in the frequency domain is displayed. From Fig. 38, it was determined that the velocity also contained a disturbance in the harmonic of the driving frequency. In the case of the 2 Hz free stream pulsation, the disturbance due to shedding was not obvious because the shedding frequency and the pulsation frequency were very different. In Fig. 39, the waveforms for the heat flux and velocity signals are displayed for the 2 Hz free stream pulsation.

Waveforms in the wake did not display any periodic character. However, spectral analysis of such signals indicated there was some organized activity at the driving frequency. Heat flux signals were processed by a program designed to eliminate noise and provide a reasonable estimate of the amplitude of fluctuation. In addition, an overall time average was calculated. The results are given in Table 3.

From these tests, it was determined that the average heat transfer is higher in the stagnation region than in the wake region. On the other hand, pulsation enhances the activity in the wake region immersed in the turbulent flow. As a result, the amplitude of reduced flux is higher in the wake region than in the stagnation region.

It is well known that heat transfer is greater in stagnation regions or in regions immersed in highly turbulent flow. The tests performed in this section determined that if a periodic disturbance is superimposed on the mean flow, the heat flux also fluctuates over both the stagnation and wake regions. The mean heat flux is not affected by the
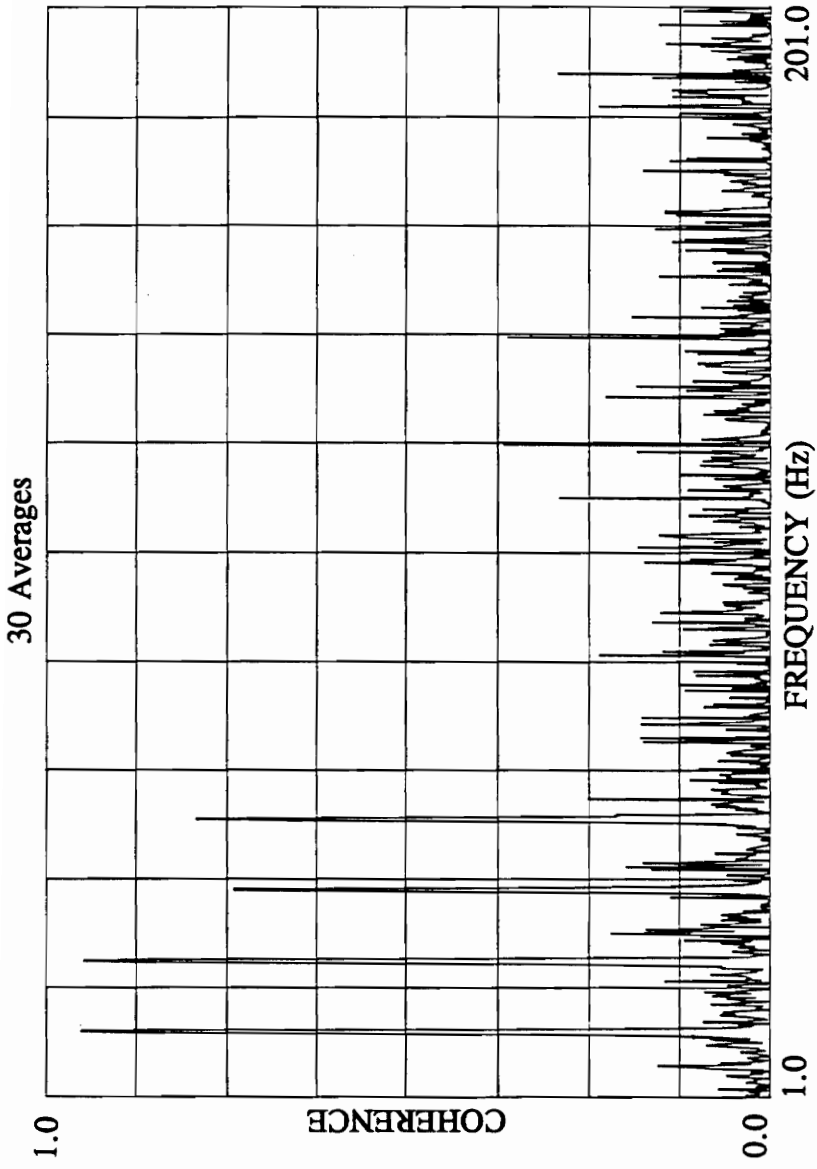
Figure 38. Coherence of Velocity and Vorticity Measurements
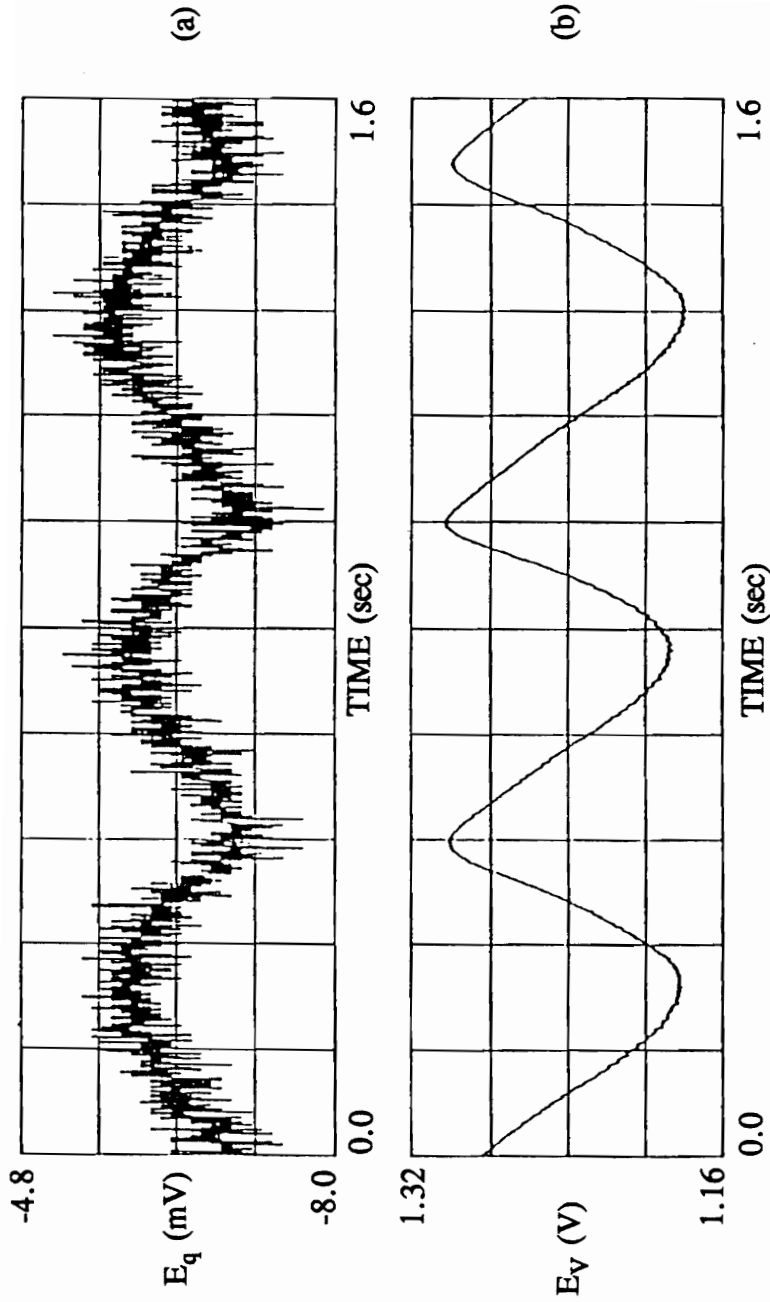
Figure 39. Waveforms of a) Heat Flux and b) Velocity for Stagnation Flow
at a Free Stream Pulsation Frequency of 2 Hz

103

pulsation. In the fully turbulent flow region, the pulsed flow leads to considerable increases in the heat transfer.

In conclusion, a mere oscillation in the oncoming free stream is not going to affect the time-averaged local heat transfer. However, the periodic disturbances in regions of fully turbulent flow, including the case of a turbine blade immersed in the spatially periodic wake of the preceding cascade, does cause an increase in the local heat transfer.

Table 3. Mean and Average Nusselt Numbers for Re = 40,000

Amplitudes	Frequency	Forward/ Reverse	Average Nu	Nu Amplitude
29.5	2	F	105	14.5
17.4	7	F	130	14.5
14.5	13	F	28	17.0
29.5	2	R	69	72.1
17.4	7	R	53	72.6
14.5	13	R	49	50.9

Appendix D

Data Processing Codes

The following FORTRAN programs were used to process data taken from the HP dynamic signal analyzer after the data had been converted into ASCII files. The first program uses the differentiation method developed by Cook and Felderman to obtain unsteady heat flux values from surface temperature measurements. The second and third programs are two different integration methods. The second program uses the method of superposition, or Duhamel's method, to obtain transient surface temperature values from unsteady heat flux measurements. The last program utilizes Green's function for the same purpose.

After the data was processed in these programs, the output from the program was imported into a Quattro Pro spreadsheet and compared with the corresponding output from the sensor. Results of these programs are illustrated in Figs. 17, 18, 19, 20, 21, and 22 of Chapter 5.

D.1 Differentiation Method

```
*****************************************************************
*                                                               *
*     This program takes the temperature response from the Heat Flux *
*     Microsensor and differentiates it with respect to time to *
*     yield heat flux at each data point.  This uses the algorithm *
*     developed by Cook and Felderman.                          *
*                                                               *
*****************************************************************
*
      REAL K,RHO,CP,Q(2049),TEMP(2049),DATA(2049)
      INTEGER TIMEF
      PARAMETER (PI = 3.141592654)
*****************************************************************
*     The ASCII data file is opened and an output file is created. *
*****************************************************************
      OPEN (9,FILE = 'TT15.ASC')
      OPEN (6,FILE = 'TT15.OUT')
*****************************************************************
*     The thermal properties of the substrate are listed as K, RHO, *
*     and CP.  The total number of data points in the ASCII file is *
*     given as TIMEF.  Units for the thermal properties are W/(cmK), *
*     kg/cm^3, and J/(kgK), respectively, so the units will work with *
*     the sensitivity's units.                                  *
*****************************************************************
      K = 1.7
      RHO = 3.26E-3
      CP = 670.
      TIMEF = 2048
*****************************************************************
*     The following do loop reads in each data point from the opened *
*     ASCII file and converts the data into surface temperature *
*     using the RTS temperature calibration curve.              *
*****************************************************************
      DO 1 I = 1,TIMEF
        READ (9,*) DATA(I)
        TEMP(I) = 330.83*DATA(I)-291.06
   1  CONTINUE
*****************************************************************
*     The next do loop performs the numerical expression developed *
*     by Cook and Felderman to calculate heat flux from surface *
*     temperature and writes the resultant heat flux for each data *
*     point to the output file created above.  The internal value of *
*     0.000391 in the method is the delta t time step.  It is   *
*     calculated by dividing the total time of the test by TIMEF, *
*     the number of data points.                                *
*****************************************************************
      DO 3 M = 1,TIMEF
        Q(M) = 0.
        DO 4 L = 2, M
        Q(M)=Q(M)+(TEMP(L)-TEMP(L-1))/(SQRT((M-L)*.000391)
     *  +SQRT((M-L+1)*.000391))
   4    CONTINUE
        Q(M) = 2.*SQRT(K*RHO*CP)/SQRT(PI)*Q(M)
  20    FORMAT (1X,I4,2X,F16.5)
        WRITE (6,20) M,Q(M)
   3  CONTINUE
      STOP
      END
```

D.2 Duhamel's Method

```
******************************************************************
*                                                                *
*     This program uses Duhamel's method to integrate the heat flux  *
*     with respect to time to yield temperature.                 *
*                                                                *
******************************************************************
*
*
      REAL K,RHO,CP,QDPRME(2049),TEMP(2049),DATA(2049)
      INTEGER TIMEF
      PARAMETER (PI = 3.141592654)
******************************************************************
*     The ASCII data file is opened and an output file is created.  *
******************************************************************
      OPEN(9,FILE = 'TF15.ASC')
      OPEN(6,FILE = 'TF15.OUT')
******************************************************************
*     The thermal properties of the substrate are listed as K, RHO,  *
*     and CP. The total number of data points in the ASCII file is   *
*     given as TIMEF.  Units for the thermal properties are W/(cmK),  *
*     kg/cm^3, and J/(kgK), respectively, so the units will work with*
*     the sensitivity's units.                                   *
******************************************************************
      K = 1.7
      RHO = 3.26E-3
      CP = 670.
      TIMEF = 2048
******************************************************************
*     The following do loop reads in each data point from the opened *
*     ASCII file and converts the data into heat flux using the     *
*     sensitivity of the sensor.  The data is multiplied by a factor *
*     of 1000 because the ASCII data file gives the output of the    *
*     sensor in volts.                                           *
******************************************************************
      DO 1 I = 1,TIMEF
        READ (9,*) DATA(I)
        QDPRME(I) = -1.*DATA(I)*1000/23.17625
   1  CONTINUE
******************************************************************
*     The next do loop performs the method of superposition, or     *
*     Duhamel's method, on the data and writes the resultant        *
*     temperature for each data point to the output file created    *
*     above.  The internal value of 0.000391 in the method is the    *
*     delta t time step.  It is calculated by dividing the total     *
*     time of the test by TIMEF, the number of data points.         *
******************************************************************
      DO 3 M = 1,TIMEF
        TEMP(M) = QDPRME(1)*SQRT((M-.5)*.000391)
        DO 4 L = 2,M
        TEMP(M) = TEMP(M)+(QDPRME(L)-QDPRME(L-1))*SQRT((M-L+1)*.000391)
   4  CONTINUE
        TEMP(M) = 2./SQRT(PI)/SQRT(K*RHO*CP)*TEMP(M)
  20    FORMAT (1x,I4,2x,F12.8)
        WRITE (6,20) M,TEMP(M)
   3  CONTINUE
      STOP
      END
```

108

D.3 Green's Function

```
*********************************************************************
*                                                                   *
*      This program uses Green's Function to integrate the heat flux *
*      with respect to time to yield temperature.                   *
*                                                                   *
*********************************************************************
*
*
       REAL K,RHO,CP,QDPRME(2049),THETA(2049),DATA(2049),ALPHA
       INTEGER TIMEF
       PARAMETER (PI = 3.141592654)
*********************************************************************
*      The ASCII data file is opened and an output file is created.  *
*********************************************************************
       OPEN(9,FILE = 'TF15.ASC')
       OPEN(6,FILE = 'TF15G.OUT')
*********************************************************************
*      The thermal properties of the substrate are listed as K, RHO, *
*      and CP.  The thermal diffusivity, a combination of the thermal *
*      properties, is given as ALPHA.  The total number of data points*
*      in the ASCII file is given as TIMEF.  Units for the thermal    *
*      properties are W/(cmK), kg/cm^3, and J/(kgK), respectively, so *
*      the units will work with the sensitivity's units.             *
*********************************************************************
       K = 1.7
       RHO = 3.26E-3
       CP = 670.
       ALPHA = K/RHO/CP
       TIMEF = 2048
*********************************************************************
*      The following do loop reads in each data point from the opened *
*      ASCII file and converts the data into heat flux using the      *
*      sensitivity of the sensor.  The data is multiplied by a factor *
*      of 1000 because the ASCII data file gives the output of the   *
*      sensor in volts.                                              *
*********************************************************************
       DO 1 I = 1,TIMEF
         READ (9,*) DATA(I)
         QDPRME(I) = -1.*DATA(I)*1000/23.17625
   1   CONTINUE
*********************************************************************
*      The next do loop performs the method of Green's function on   *
*      the data and writes the resultant temperature for each data   *
*      point to the output file created above.  The internal value of *
*      0.000391 in the method is the delta t time step.  It is       *
*      calculated by dividing the total time of the test by TIMEF,   *
*      the number of data points.                                    *
*********************************************************************
       DO 3 M = 1,TIMEF
         THETA(M)= 0.
       DO 4 J = M,1,-1
         IF (J.EQ.1) THEN
           THETA(M)=THETA(M)-2.*SQRT(ALPHA)/K/SQRT(PI)*QDPRME(J)
     *     *(SQRT(((M-.5)-(J-.5))*.000391)-SQRT((M-.5)*.000391))
         ELSE
           THETA(M)=THETA(M)-2.*SQRT(ALPHA)/K/SQRT(PI)*QDPRME(J)
     *   *(SQRT(((M-.5)-(J-.5))*.000391)-SQRT(((M-.5)-(J-1.5))*.000391))
         ENDIF
   4   CONTINUE
  20   FORMAT (1x,I4,2x,F12.8)
         WRITE (6,20) M,THETA(M)
   3   CONTINUE
       STOP
       END
```

109

Appendix E

Dimension Tables for Detailed Drawings

The following tables provide the dimensions for the detailed drawings shown in Figs. 8 - 11. All dimensions are given in millimeters and inches. Table 4 lists the dimensions for the sensor housing block diagram illustrated in Fig. 8. Next, Table 5 lists the dimensions for the wall and base supports shown in Fig. 9. The following table, Table 6, lists the dimensions for the sensor box detailed in Fig. 10. The last table, Table 7, lists the dimensions for the shutter and slide supports illustrated in Fig. 11.

Table 4. Dimensions for Detailed Drawing of Sensor Housing Block

LETTER	DIMENSIONS (mm)	DIMENSIONS (in.)
A	19.050 ± 0.254	0.750 ± 0.010
B	9.525 ± 0.254	0.375 ± 0.010
C	12.70	0.500
D	57.150 ± 0.254	2.250 ± 0.010
E	66.675 ± 0.254	2.625 ± 0.010
F	4.763 ± 0.254	0.1875 ± 0.010
G	9.525	0.375
H	0.794	0.03125
I	12.70 ± 0.254	0.500 ± 0.010
J	38.10 ± 0.254	1.500 ± 0.010
K	50.8	2.000
L	9.91 ± 0.254	0.390 ± 0.010
M	38.1	1.500
N	15.88 ± 0.254	0.625 ± 0.010
O	19.050	0.750
P	76.2 ± 0.254	3.000 ± 0.010
Q	11.11 ± 0.254	0.4375 ± 0.010
R	65.09 ± 0.254	2.5625 ± 0.010

Table 5. Dimensions for Detailed Drawings of Wall and Base Supports

LETTER	DIMENSIONS (mm)	DIMENSIONS (in.)
A	38.10 ± 0.254	1.500 ± 0.010
B	19.050 ± 0.254	0.750 ± 0.010
C	9.525 ± 0.254	0.375 ± 0.010
D	19.689 ± 0.254	0.775 ± 0.010
E	57.150 ± 0.254	2.250 ± 0.010
F	6.60	0.260
G	6.86	0.270
H	342.90 ± 0.254	13.500 ± 0.010
I	6.35 ± 0.254	0.250 ± 0.010
J	66.675 ± 0.254	2.625 ± 0.010
K	76.2 ± 0.254	3.000 ± 0.010
L	12.70 ± 0.254	0.500 ± 0.010
M	6.35	0.250
N	28.58 ± 0.254	1.125 ± 0.010
O	15.88 ± 0.254	0.625 ± 0.010
P	12.70	0.500

Table 6. Dimensions for Detailed Drawing of Sensor Box

LETTER	DIMENSIONS (mm)	DIMENSIONS (in.)
A	127.00 ± 0.254	5.000 ± 0.010
B	6.35	0.250
C	66.675 ± 0.254	2.625 ± 0.010
D	4.763 ± 0.254	0.1875 ± 0.010
E	7.144 ± 0.254	0.28125 ± 0.010
F	61.91 ± 0.254	2.4375 ± 0.010
G	76.2 ± 0.254	3.000 ± 0.010
H	65.09 ± 0.254	2.5625 ± 0.010
I	11.11 ± 0.254	0.4375 ± 0.010

Table 7. Dimensions for Detailed Drawing of Shutter and Slide Supports

LETTER	DIMENSION (mm)	DIMENSION (in.)
A	190.50 ± 0.381	7.50 ± 0.015
B	50.8 ± 0.254	2.000 ± 0.010
C	107.95 ± 0.254	4.25 ± 0.010
D	6.60	0.260
E	6.86	0.270
F	151.89 ± 0.254	5.980 ± 0.010
G	9.525 ± 0.254	0.375 ± 0.010
H	19.050 ± 0.254	0.750 ± 0.010
I	180.98 ± 0.381	7.125 ± 0.015
J	6.35	0.250
K	75.69 ± 0.127	2.980 ± 0.005
L	50.8 ± 0.254	2.000 ± 0.010
M	38.10 ± 0.254	1.500 ± 0.010
N	12.70 ± 0.254	0.500 ± 0.010
O	6.35 ± 0.254	0.250 ± 0.010
P	57.150 ± 0.254	2.25 ± 0.010
Q	76.2 ± 0.254	3.000 ± 0.010

Vita

Karen Irene Baker was born in Titusville, Florida on December 7, 1969 to Patrick and Faye Baker. When she was eight years old, she moved to Gastonia, North Carolina where her father began a new job with Southern Bell. After graduating from Ashbrook High School as salutatorian in June 1987, she began her undergraduate studies at the University of North Carolina at Charlotte. In May 1991, she received her Bachelor of Science in Mechanical Engineering with cum laude honors. In August of that same year, she began graduate studies at Virginia Polytechnic Institute and State University. Upon completion of the Master of Science in Mechanical Engineering degree, she will begin a career at Bechtel Corporation in Gaithersburg, Maryland as a Mechanical Engineer.

Karen Irene Baker